Heavy Meson Spectroscopy from Lattice QCD

Peter Boyle

Doctor of Philosophy

The University of Edinburgh

1997

Abstract

This thesis introduces lattice simulation techniques and the physics of heavy quark systems, and then presents results for the masses and mass splittings of mesons containing a heavy quark obtained from simulations of quenched QCD.

Chapter 3 presents the results obtained from a calculation of the pseudoscalar, vector and orbitally excited heavy meson spectrum using a $16^3 \times 48$ lattice, while Chapter 4 presents and compares a similar calculation using a $24^3 \times 48$ lattice with a smaller lattice spacing. The first simulation includes a calculation of the fine structure of the quarkonium triplet χ-states, and of a fine splitting in heavy-light systems. The results obtained for the hyperfine splittings scale well between the two lattices, showing that the continuum limit of the quenched theory is inconsistent with experiment. The results are:

Splitting	Calculation (MeV)	Experiment (MeV)
$D^* - D$	110 (6)	142
$D_s^* - D_s$	99 (4)	144
$B^* - B$	41 (8)	46
$B_s^* - B_s$	40 (5)	47
$J/\psi - \eta_c$	69 (2)	117
$\Upsilon - \eta_b$	22 (1)	-

The final chapter contains a study of a novel gauge-invariant smearing technique that gives improved signals for ground state mesons, and, for the first time, yields plateaux for radially excited mesons. The feasibility study demonstrates a dramatic improvement in both the stability and precision of fits to the spectrum.

Declaration

This thesis has been wholly composed by me and presents research carried out by me as part of the UKQCD collaboration. My calculations used gauge configurations generated by the UKQCD collaboration. The data generation for the calculation in Chapter 3 was shared between Paul Rowland, Sinead Ryan, David Richards and myself. The data generation for the results in Chapters 4 and 5 was performed by me, using existing UKQCD local light quark propagators. The parallel code to construct hadron correlators was written largely by me, with several routines written by Stephen Pickles and Paul Rowland. All results were analysed by myself alone.

The results of these calculations have been published in

- Comprehensive Spectroscopy of D, D_s and Charmonium Systems from Relativistic Lattice QCD, P. Boyle, Nucl. Phys. B53 (Proc Suppl) 398-400, 1997

- Heavy Meson Spectroscopy at $\beta = 6.0$, Peter Boyle, Poster Presented at Lattice '97

Other work to which I have contributed includes:

- Hybrid and Orbitally Excited Mesons in Quenched QCD, P. Lacock et al. Contributed to Lattice 97

- Hybrid Mesons from Quenched QCD P. Lacock et al,Phys.Lett.B401:308-312,1997

- Orbitally Excited and Hybrid Mesons from the Lattice P. Lacock et al, Phys.Rev.D54:6997-7009,1996

Acknowledgements

I would like to thank my supervisors, Richard Kenway and Brian Pendleton, Christine Davies for her interest in my work in Chapters 3 and 4, and the UKQCD collaboration whose resources were used extensively for this project. My PhD course was funded by the Carnegie Trust for the Universities of Scotland, whose charitable support I gratefully acknowledge.

I want to thank my flatmates and colleagues, past and present, Douglas, Jane, Stephen, Alice, Dave, Carol, Iain, Harry, Sinead, Steve, Zbysek et al who have made my stay here enjoyable. I almost forgive Harry for introducing me to the Royal Oak.

Finally I would like to thank my family, Julie, Kate, Stuart, Mum and Dad for their love and support throughout, and dedicate this thesis to them.

Contents

Chapter 1

Introduction to Lattice QCD

1.1 The Need for Non-Perturbative Physics

The Standard Model of the strong and electroweak interactions of quarks and leptons has provided a spectacularly successful explanation of the electroweak force and the strong force at high energies. The coupling of the strong force displays asymptotic freedom, rendering a perturbative approximation to the theory convergent at sufficiently high energy, while low energy physics, where the coupling $\alpha_s \sim 1$, is not predictable by traditional techniques.

In the absence of solutions of QCD, the quark model qualitatively explains the states in the hadron spectrum, and various models and symmetry arguments can use experimental input to form predictions of one system from another. This level of understanding of the particles around us is unsatisfactory, and hadron phenomenology should in principle be derived from the parameters of the Standard Model, without a priori assumption. Additionally, our inability to solve soft QCD systems leaves poorly understood hadronisation factors for a number of interesting experimental processes. Because of confinement, these factors are a theoretical uncertainty in experimental determinations of CKM matrix elements, such as V_{td} from neutral B meson mixing, and V_{ub} from the semi-leptonic decays of B mesons.

Lattice QCD is a framework that allows the Monte Carlo simulation of QCD and provides a means to demonstrate that QCD correctly reproduces hadron phenomenology. Furthermore the evaluation of the QCD matrix elements of the electroweak currents allows the disentanglement of the CKM matrix elements from hitherto unknown QCD prefactors.

Lattice QCD is applied in this thesis in an *ab initio* study of the phenomenology of mesons containing charm quarks.

1.2 The Strong Sector of the Standard Model

The pure QCD sector of the Standard Model [1, 2, 3] consists of an SU(3) gluon field $A_\mu(x) = A^a_\mu(x)T_a$, coupled to six quark fields $\psi_f(x)$ where $f \in \{u, d, s, c, b, t\}$. Here T_a are the basis matrices of the Lie algebra of SU(3) with normalisation $\mathrm{Tr}(T_aT_b) = \frac{1}{2}\delta_{ab}$, and can be taken as $T^a = \frac{\lambda^a}{2}$ where λ^a are the Gell-Mann matrices.

The local gauge invariance of the theory is made manifest by constructing the action out of covariant derivatives,

$$D_\mu = \partial_\mu + igA_\mu, \tag{1.1}$$

substituted for regular derivatives in the free theory. Under a gauge transformation $\Lambda(x) = e^{ig\lambda_a(x)T_a}$, the fields transform as

$$\psi_i(x) \to [e^{-ig\lambda_a(x)T_a}]_{ij}\psi_j = \Lambda(x)^{-1}_{ij}\psi_j, \tag{1.2}$$

$$A_\mu(x) \to \Lambda^{-1}(A_\mu - \frac{i}{g}\partial_\mu)\Lambda, \tag{1.3}$$

so that,

$$\begin{aligned} D'_\mu &= (\partial_\mu + ig\{\Lambda^{-1}(A_\mu - \frac{i}{g}\partial_\mu)\Lambda\}) && (1.4)\\ &= \Lambda^{-1}(\partial_\mu + igA_\mu)\Lambda && (1.5)\\ D'_\mu\psi' &= \Lambda^{-1}D_\mu\psi. && (1.6) \end{aligned}$$

We construct the field strength tensor

$$F_{\mu\nu} = \frac{1}{ig}[D_\mu, D_\nu] \tag{1.7}$$

$$= \partial_\mu A_\nu - \partial_\nu A_\mu + ig[A_\mu, A_\nu]. \tag{1.8}$$

We can now define the QCD Lagrangian as

$$\mathcal{L}_{\mathrm{QCD}} = \mathcal{L}_{\mathrm{YM}} + \sum_{f=u,d,s,c,t,b} \bar{\psi}_f (i\not{D} - m_f)\psi_f \tag{1.9}$$

where the Yang-Mills Lagrangian is

$$\mathcal{L}_{\mathrm{YM}} = -\frac{1}{2}\mathrm{Tr} F_{\mu\nu}F^{\mu\nu} = -\frac{1}{4}F_a^{\mu\nu}F^a_{\mu\nu}. \tag{1.10}$$

The QCD action is then

$$S_{\mathrm{QCD}}[A, \psi_f] = \int d^4x \mathcal{L}_{\mathrm{QCD}}(x). \tag{1.11}$$

The Minkowski partition function for QCD is then, ignoring Fadeev-Popov gauge fixing terms,

$$Z = \int \mathcal{D}\psi\mathcal{D}\bar{\psi}\mathcal{D}A e^{iS_{\mathrm{QCD}}}. \tag{1.12}$$

In practice this partition function is the integral of a wildly oscillating integrand, and is not amenable to either numerical simulation, or indeed proof of convergence. The integrals are much better treated in Euclidean space, where the integrand is a decaying exponential, and the Green functions of the Minkowski theory inferred by analytic continuation.

1.2.1 QCD in Euclidean space-time

The topic of Wick rotation and analytic continuation is worthy of a brief aside here. Wick rotation changes the Minkowski metric into a Euclidean metric, and consists of the following set of transformations on the coordinates and Dirac matrices:

$$\begin{array}{rclcrcl} x^0 & = & -ix_E^4 & , & \gamma_i^E & = & i\gamma_i, \\ \gamma_4^E & = & \gamma_0 & , & A_4^E & = & iA_0. \end{array} \tag{1.13}$$

This gives the Euclidean metric, $2\delta_{\mu\nu} = \{\gamma^E_\mu, \gamma^E_\nu\}$. The substitutions performed on the action lead to:

$$\begin{aligned} d^4x &\longrightarrow -id^4x^E, && (1.14)\\ \not{D} &\longrightarrow i\not{D}^{\,E}, && (1.15)\\ \bar{\psi}_f(i\not{D} - m_f)\psi_f &\longrightarrow -\bar{\psi}_f(\not{D}^{\,E} + m_f)\psi_f, && (1.16) \end{aligned}$$

$$\begin{aligned} S_{\text{QCD}} &\longrightarrow i\int d^4x^E\{\frac{1}{4}\text{Tr}F^E_{\mu\nu}F^E_{\mu\nu} + \sum_f \bar{\psi}_f(\not{D}^{\,E} + m_f)\psi_f\} && (1.17)\\ &= iS^E_{\text{QCD}}, && (1.18) \end{aligned}$$

$$Z_E = \int \mathcal{D}\psi\mathcal{D}\bar{\psi}\mathcal{D}Ae^{-S^E_{\text{QCD}}}. \qquad (1.19)$$

It is clear that the substitution $x_0 \to ix^E_4$ is not a valid change of variables in the path integral since the limits of integration remain real. When dealt with rigorously, [4] it can be shown that the Green functions of the Euclidean action are the analytic continuation in the time variable of the Minkowski Green functions to the imaginary axis. In order to explain the connection between the Euclidean and Minkowski theories I quote some complex analysis in order to precisely define what is meant by *analytic continuation* [5].

If two complex differentiable (analytic) functions F and G are equal on a set of points that has a limit point in $\mathbb{C}$ then the two functions are identically equal. This means that if $F : \mathbb{R} \to \mathbb{C}$ is defined on either the real or imaginary line as a function of t then there is a *unique* differentiable function $G : \mathbb{C} \to \mathbb{C}$ s.t. $G(x) = F(x)\ \forall x \in \mathbb{R}$. G is then called the analytic continuation of F to $\mathbb{C}$. Hence a Green function $G(x,t)$ uniquely defines $G(x,it)$ and *vice versa*.

The essential point is that the two path integrals are not directly related, but rather the connection comes only through the Wick rotated time dependence of their Green functions. The lattice calculation can therefore be used to infer the properties of the Minkowski Green functions by the appropriate transformation of their t dependence.

For the Minkowski theory associated in this way with a Euclidean theory to make sense, it must have a positive semidefinite Hermitian Hamiltonian. In order that this be the case, the transfer matrix of the Euclidean theory must be reflection positive. Reflection positivity of the widely used Wilson action is shown by e.g. Montvay and Munster [4]. It is worth noting here that the path integral on a Euclidean space-time lattice is often used in constructive field theory as the definition of the Minkowski theory, since it is difficult to define a convergent limiting process for the path integral in Minkowski space.

1.3 Lattice QCD

Lattice QCD is a framework for studying the Euclidean path integral on a discretised space-time.

For simplicity, consider a hypercubic lattice of size N^4 with lattice spacing a, and length $L = Na$. On each site we define a Grassmann spinor of flavour f, $\psi^f_{\alpha a}$, that transforms in the fundamental representation of the gauge group $SU(3)$.

Analogous to the covariant derivative, we construct a non-local covariant difference on the lattice, to enable the construction of manifestly gauge covariant operators. Suppose we have a field ψ_0, transforming as the fundamental representation of the gauge group, whose covariant derivative is identically zero. We can therefore write the spatial derivative of the field in terms of the gauge field and establish the parallel transport of this field between two sites:

$$\partial_\mu \psi_0(x) = -igA_\mu \psi_0(x). \tag{1.20}$$

Hence for an infinitesimal difference, $\epsilon = \frac{a}{N}$

$$\psi_0(x + \epsilon\mu) = e^{\epsilon\partial_\mu}\psi_0(x) \simeq (1 + \epsilon\partial_\mu)\psi_0(x) \equiv (1 - i\epsilon g A_\mu)\psi_0(x). \tag{1.21}$$

Iterating, we obtain

$$\psi_0(x + a\mu) = \lim_{N\to\infty} \prod_{i=1}^{N} [1 - i\frac{ag}{N} A_\mu(x + \frac{ia}{N}\mu)]\psi_0(x). \tag{1.22}$$

We therefore define the link variable $U_\mu \in SU(3)$, where the path ordered exponential is defined by the above, as

$$U_\mu(x) = \mathcal{P}e^{iag\int_0^1 A_\mu(x+ta\mu)dt} \simeq e^{igA_\mu(x+\frac{a}{2}\mu)}, \tag{1.23}$$

such that link $U_\mu(x)\psi(x+\mu)$ covariantly transports a colour vector from $x+\mu$ to x. The path integral in lattice QCD is performed over these gauge group elements U_μ (as opposed to the Lie algebra) using the Haar measure.

There are two ways to form gauge invariant (non-local) objects from links and spinors:

- Traced closed loops of links, such as the plaquette, $\mathrm{Tr}U^{\square}_{\mu\nu} = \mathrm{Tr}U_\mu(x)U_\nu(x+\mu)U^\dagger_\mu(x+\nu)U^\dagger_\nu(x)$.
- Non-local quark bilinears, such as $\bar\psi(x)U_\mu(x)\psi(x+\mu)$.

We are now in a position to define the Wilson [6] lattice action for one quark flavour, composed of such gauge invariant objects:

$$S_{\mathrm{latt}} = S_G + S_F + O(a) \tag{1.24}$$

$$S_G = \beta \sum_x \sum_{\nu,\mu>\nu} \left(1 - \frac{1}{3}\mathrm{ReTr}\left[U^{\square}_{\mu\nu}(x)\right]\right) \tag{1.25}$$

$$S_F = \sum_x \left\{ \begin{array}{c} -\sum\limits_{\mu=0}^{3} \frac{1}{2}\bar\psi\left[U_\mu(x)(r-\gamma_\mu)\psi(x+\mu) + U^\dagger_\mu(x-\mu)(r+\gamma_\mu)\psi(x-\mu)\right] \\ +(m+4r)\bar\psi(x)\psi(x) \end{array} \right\}. \tag{1.26}$$

Here r is a dimensionless coefficient of the lattice Laplacian, introduced by Wilson to control the fermion's dispersion relation at the Brillioun zone boundaries. r is typically set to one in order to halve the communications overhead, since $1+\gamma_\mu$ is a projection. The fermion action is more commonly written in terms of the fermion matrix with the hopping parameter $\kappa = \frac{1}{2m+8r}$,

$$S_F = \frac{1}{2\kappa}\sum_{x,y}\bar{\psi}(x)M_{\text{wilson}}(x,y)\psi(y), \tag{1.27}$$

where

$$M_{wilson}(x,y) = \delta_{x,y} - \kappa\sum_{\mu=0}^{3} U_\mu(x)(1-\gamma_\mu)\delta(y,x+\mu) + U^\dagger_\mu(x-\mu)(1+\gamma_\mu)\delta(y,x-\mu). \tag{1.28}$$

Notice that the action has been left ambiguous at $O(a)$, because operators at this order may be added to the action without changing the continuum limit. The usual Wilson action, however, contains only those terms already mentioned. This point will be returned to later when higher dimensional operators are added to alter the approach of the lattice action to its continuum limit.

1.4 The Lattice Path Integral

The lattice generating functional is written as

$$Z_{\text{latt}}(\bar{\sigma},\sigma) = \int [dU][d\psi][d\bar{\psi}]e^{-S_G-\sum_f \bar{\psi}_f M_f \psi_f} e^{-\sum_f\sum_x[\bar{\sigma}_f\psi_f + \bar{\psi}_f\sigma_f]}. \tag{1.29}$$

The Gaussian Grassmann integral may be performed immediately, and produces positive powers of the determinant of the fermion matrix. For correlation functions involving the quark fields, the usual matrix inverses arise after functional differentiation.

$$Z_{\text{latt}}(\bar{\sigma},\sigma) = \int [dU]\prod_f \det M_f(U)e^{-S_G}e^{-\sum_f \bar{\sigma}_f M_f^{-1}\sigma_f}. \tag{1.30}$$

The path integral over the gauge fields, U, is performed using a Monte Carlo algorithm. Essentially, a stochastic estimate of the integral is made, by sampling the important parts of the gauge field configuration space. The technique used involves the use of a Markov [7] process to generate sequences of configurations with the probability distribution

$$\mathcal{P}[U] = \frac{1}{Z_{\text{latt}}} e^{-S_G} \prod_{f}^{N_{\text{sea}}} \det M_f(U). \tag{1.31}$$

Having generated these sample fields, the quark correlation functions of the lattice theory can be evaluated by inverting the fermion matrix as discussed in Section 1.8. The Euclidean Green function is approximated by the average of the correlation function over these configurations. In practice a numerical simulation samples a different distibution $\mathcal{P}[U]$ in gauge space than that suggested by the Standard Model ($N_{sea} = 3$, $m_u \simeq m_d \simeq 10\text{MeV}$, $m_s \simeq 150\text{MeV}$), and in a full simulation, extrapolations in the simulation parameters must be performed.

1.4.1 The Simulated Gauge Distribution

As mentioned, in lattice simulations there is typically an uncontrolled approximation made in the sampling of gauge space by setting N_{sea} either to 0, 2, or 4 with a sea quark mass around the strange quark mass. The incorrect masses and number of sea quark flavours are clearly a major shortcoming of present day lattice QCD results, however, for computational and algorithmic reasons, these approximations are presently unavoidable:

- The simulated sea quark mass is large because of the computational expense of light quark matrix inversions involved in the generation of the distribution, and because lighter sea quarks suffer more strongly from finite volume effects.

- The use of an even number of flavours is required by the Monte Carlo algorithm used, where we write the squared fermion determinant as an additional Gaussian integral over bosonic spinors ϕ with the explicitly Hermitian bilinear $\phi^\dagger(M^\dagger M)^{-1}\phi$, added to the action. While there are proposed algorithms, there is no tried and tested technique for odd numbers of flavours. This is problematic for lattice QCD since we should simulate with $n_f = 3$.

The results presented in this thesis are performed in the quenched approximation, equivalently $n_{\mathrm{sea}} = 0$, $m_{\mathrm{sea}} \to \infty$ or $\det M_{\mathrm{sea}} = \mathrm{Constant}$. A discussion of quenching errors will be presented later when considering heavy quark systems. Fortunately the quenched approximation will be partially addressed by the coming generation of computers.

1.5 Continuum Limit of the Lattice Action

Thus far we have defined a discretised action, and discussed how to perform a path integral numerically in the regularised Euclidean field theory. It is now necessary to show that the path integral we are performing has QCD as its continuum limit. The discussion in this thesis is limited to the comments that the composite fields in the lattice action may be written as a Taylor series in the continuum fields and their derivatives, allowing the following expansion to be made:

$$S_{\mathrm{latt}} = S_{cont} + aS_1 + a^2 S_2 + \ldots, \tag{1.32}$$

where S_k are higher order terms in the local effective expansion of the lattice action, and are constructed from continuum fields.

It can be shown [8] that

$$S_G = \int d^4x \frac{1}{4} F^a_{\mu\nu} F^a_{\mu\nu} + O(a^2). \tag{1.33}$$

It can also be shown [9] that

$$S_F = \not{D} + m + a\frac{r}{2} D^2 + O(a^2). \tag{1.34}$$

The leading discretisation error in the action is therefore of $O(a)$, and in fact comes from the Wilson r term. It is possible to add terms of $O(a)$ to eliminate this leading error, as in the Symanzik [10] improvement programme, introducing the concept of *improved* actions which approach the continuum faster.

1.6 Improved Actions

1.6.1 Clover Action

Sheikholeslami and Wohlert [9] introduced the clover action which contains no $O(a)$ corrections to tree-level in perturbation theory *for on shell Green functions*, using the concept of a classically improved action. Thus far we have classified the discretisation errors in the theory according to the errors in the action. The observables of the theory are the Green functions, and we are left with the question of how the accuracy of the discrete action influences the accuracy of the Green functions of the theory. Sheikholeslami and Wohlert observed that since the tree-level vertex functions come directly from functional derivatives of the bare action, an action which is $O(a)$ improved for classical fermion fields produces $O(a)$ improved tree-level on-shell Green functions.

They add the term

$$\delta S = -C_{SW}\frac{ar}{4}\bar{\psi} ig\sigma_{\mu\nu}F_{\mu\nu}\psi^1 \tag{1.35}$$

to the Wilson action. With classical fields ψ_c this SW action is:

$$S^F_{SW} = \bar{\psi}_c\left[\not{D} + m + a\frac{r}{2}\left(D^2 - i\frac{1}{2}C_{SW}g\sigma_{\mu\nu}F_{\mu\nu}\right)\right]\psi_c \tag{1.36}$$

Setting the *clover* coefficient $C_{SW} = 1$ we can use the Euclidean continuum relation $\not{D}^{\,2} = D^2 - i\frac{g}{2}\sigma_{\mu\nu}F_{\mu\nu} = m^2$ to leading order to obtain

$$\begin{aligned} S^F_{SW} &= \bar{\psi}_c\left[\not{D} + m + a\frac{r}{2}\not{D}^{\,2}\right]\psi_c + O(a^2) && (1.37)\\ &= \bar{\psi}_c\left[\not{D} + m(1 + \frac{r}{2}am)\right]\psi_c + O(a^2). && (1.38)\end{aligned}$$

This constitutes an $O(am)$ redefinition of the bare quark mass for classical fields, and, as such, the action yields the $O(a)$ improved tree-level on-shell Green functions.

[1] Here we use the Heatlie [11] convention $\sigma_{\mu\nu} = \frac{1}{2}[\gamma_\mu, \gamma_\nu]$. Other conventions place the factor of i on the definition of σ.

1.6.2 Operator Rotations

Heatlie et al [11] considered the two link action

$$S_{2link} = \bar{\psi}\left[\not{D} + m + \Delta_1^2 - \Delta_2^2\right]\psi, \tag{1.39}$$

where $\Delta_1^2 - \Delta_2^2$ is the difference between the one-link and two-link lattice Laplacian, and breaks chiral symmetry with order $O(a^2)$ terms, avoiding the Nielson Ninomiya [12] theorem . They showed that, to one loop in perturbation theory, both the self energy diagrams and local quark bilinear vertices (relevant to weak decay amplitudes) contain neither errors of $O(a)$ nor $O(g_0^2 a \log a)$. They then show that, for amplitudes between on shell states, the SW action is equivalent to the two link action up to terms of $O(a^2)$ on making the change of variables

$$\psi'_{SW} = \left[1 - a\frac{r}{4}(\not{D} - m_0)\right]\psi_{SW}, \tag{1.40}$$

$$\bar{\psi}'_{SW} = \bar{\psi}_{SW}\left[1 + a\frac{r}{4}(\overleftarrow{\not{D}} + m_0)\right]. \tag{1.41}$$

For the external fields in on-shell Green functions the transformation may be written as one of

$$\psi'_{SW} = \left[1 - a\frac{r}{2}(\not{D})\right]\psi_{SW} \tag{1.42}$$

$$= \left[1 + a\frac{r}{2}(m)\right]\psi_{SW}. \tag{1.43}$$

The transformation can be considered a change of variables in the functional integral for the two-link action, allowing simulation with the local and hence less expensive SW action and obtain $O(a)$ improved matrix elements using the rotated operators.

1.6.3 Mean Field Improvement

The absolute minimum of the classical action is the case of zero field tensor, corresponding to some transform of the unit gauge, $U_\mu(x) = \mathbb{I}_{3\times3}$, equivalent to

$A_\mu(x) = 0$. At finite β fluctuations of the plaquettes from unity in the direction of each of the eight generators of $SU(3)$ are accepted, so that the mean traced plaquette, $u_0 = \sqrt[4]{\frac{1}{3}\langle \text{Plaq} \rangle} < 1$, for non-zero lattice spacing.

Lepage and Mackenzie [13] showed that large renormalisations of the bare lattice coupling occur, and suggested that a mean field rescaling of the link be made by non-perturbatively determining u_0 , and inserting $U'_\mu = \frac{1}{u_0} U_\mu$ in the operators of the action, motivated intuitively as resumming tadpole divergences in the lattice definition of the link $U_\mu(x) = e^{iagA_\mu(x+\frac{1}{2}\hat{\mu})}$.

The effect of this substitution is to redefine the bare coupling and mass constants without changing that part of the lattice action, while increasing the clover coefficient from 1 to about 1.4 at current quenched β values. Lepage and Mackenzie showed that low order perturbation theory in this redefined coupling more accurately reproduces non-perturbatively determined quantities. Since in the continuum $u_0 = 1$, this *tadpole improved* action has the correct continuum limit. While somewhat *ad hoc*, this prescription produces improvement coefficients much nearer to non-perturbatively determined coefficients than tree level improvement, and hence should have a faster approach to continuum for most quantities than tree level improvement.

1.6.4 Non-perturbative O(a) Improvement

The Alpha collaboration has developed an elegant lattice Schroedinger functional framework that has enabled them to study Green functions in the presence of external boundary fields [14, 15, 16]. In particular, they considered the non-perturbative $O(a)$ improvement of the Wilson action by studying the violation of the PCAC relation by lattice artifacts in different classical background fields. They note that all dimension five operators (including powers of m) that are charge, parity and gauge invariant mix non-perturbatively in a local effective expansion of the lattice action, and so are added to the action with free coefficients. These coefficients are then determined, where possible non-perturbatively, by optimally adjusting them to leave the PCAC relation minimally violated for all values of the boundary conditions. I shall briefly discuss the Alpha improvement scheme. The Alpha scheme also accounts for the non-perturbative mixing of local composite operators with those of raised dimension, but this is not discussed here.

The complete set of dimension five operators is:

$$\mathcal{O}_1 = \bar{\psi}\sigma_{\mu\nu}F_{\mu\nu}\psi, \tag{1.44}$$

$$\mathcal{O}_2 = \bar{\psi}D_\mu D_\mu\psi + \bar{\psi}\overleftarrow{D}_\mu\overleftarrow{D}_\mu\psi, \tag{1.45}$$

$$\mathcal{O}_3 = m\mathrm{Tr}[F_{\mu\nu}F_{\mu\nu}], \tag{1.46}$$

$$\mathcal{O}_4 = m\{\bar{\psi}\not{D}\psi - \bar{\psi}\overleftarrow{\not{D}}\psi\}, \tag{1.47}$$

$$\mathcal{O}_5 = m^2\bar{\psi}\psi. \tag{1.48}$$

For on-shell quantities, the operators $\mathcal{O}_2$ and $\mathcal{O}_4$ may be eliminated and the three remaining operators are added to the action. $\mathcal{O}_3$ and $\mathcal{O}_5$ can be absorbed into a mass dependent rescaling of the bare coupling and mass, however this does complicate dynamical simulations somewhat. The remaining dimension five operator to be added to the action, $\mathcal{O}_1$ is the usual clover term. The optimal clover coefficient has been calculated non-perturbatively by the Alpha collaboration, and the bare coupling dependence fitted, yielding the approximate relation

$$C_{SW}(g_0) = \frac{1 - 0.656g_0^2 - 0.152g_0^4 - 0.054g_0^6}{1 - 0.922g_0^2}. \tag{1.49}$$

At the lattice couplings used in our simulations, the various clover coefficient prescriptions are given in Table 1.1.

As mentioned, the non-perturbative C_{SW} is higher than that obtained by the mean field prescription, but leaves us confident that the mean field improved results will have a better continuum approach than $C_{SW} = 1$, while still containing some $O(a)$ effects. The calculations performed in this thesis used the mean field improved action.

Table 1.1: Clover coefficients in various improvement schemes

β	C_{SW}^{Alpha}	$C_{SW}^{\text{mean field}}$	$C_{SW}^{\text{tree level}}$	C_{SW}^{Wilson}
6.0	1.76923	1.47852	1.0	0.0
6.2	1.61387	1.44239	1.0	0.0

1.7 Properties of the fermion propagator

The (implicitly gauge dependent) lattice fermion propagator $G(x, y)$ is defined by:

$$\begin{aligned} G^{-1}(x,y) &= \left\{1 - \tfrac{irC_{SW}\kappa}{2} ig\sigma_{\mu\nu}F_{\mu\nu}\right\}\delta_{x,y} \\ &- \kappa\sum_{\mu=0}^{3} U_\mu(x)(1-\gamma_\mu)\delta_{y,x+\mu} + U_\mu^\dagger(x-\mu)(1+\gamma_\mu)\delta_{y,x-\mu}, \end{aligned} \tag{1.50}$$

and has a number of useful properties that can be used when constructing lattice correlation functions for bound states of definite quantum numbers.

γ_5 Hermiticity

$$G^{\alpha\beta}_{ab}(x,0) = \gamma_{5\ ac}\ \ G^{\beta\alpha *}_{dc}(0,x)\ \ \gamma_{5\ db} = (\gamma_5 G^\dagger \gamma_5)^{\alpha\beta}_{ab}. \tag{1.51}$$

Parity inversion

$$G(U^P; 0, -x) = \gamma_4 G(U; 0, x)\gamma_4. \tag{1.52}$$

Charge Conjugation

$$G(U; x, 0) = CG^T(U^C; 0, x)C^{-1}, \tag{1.53}$$

where

$$C = \gamma_4\gamma_2. \tag{1.54}$$

The so called γ_5 symmetry may be used to relate the forward and backwards propagators. This is of great importance to numerical simulation since the mesonic correlator from 0 to x can be constructed entirely from quark propagators starting from one origin, rather than requiring propagators from all points.

$$\begin{aligned}\langle(\bar\psi_1\gamma_5\Gamma^{\rm sink}\psi_2)(x)(\bar\psi_2\Gamma^{\rm source}\gamma_5\psi_1)(0)\rangle &= Z^{-1}\int\mathcal{D}U\,(\det M_f)^{n_{\rm sea}}\,e^{-S_G}\\ &\quad\times\left\{G_{2\ ab}^{\alpha\beta}(x,0)\ \Gamma_{bd}^{\rm source}\ G_{1\ cd}^{\alpha\beta}(x,0)^*\ \Gamma_{ca}^{\rm sink}\right\}\end{aligned} \tag{1.55}$$

Thus only one row of the inverse fermion matrix need be found by numerically solving the equation

$$M(y,x)\psi(x)=\eta(y), \tag{1.56}$$

where typically the source

$$\eta(y)=\delta_{y,0}\delta_{\alpha\beta}\delta_{ab} \tag{1.57}$$

for all spin colour combinations (β,b). As mentioned, this is performed numerically by minimising the residual r, where

$$|r|^2=\frac{\sum\limits_{x\in L^3\times T}|\sum_{x'}M(x;x')\psi(x')-\eta(x)|^2}{\sum_x|\eta(x)|^2} \tag{1.58}$$

Note that a gauge covariant non-local source, $\eta_{\rm smeared}(y)$, may be used. To preserve the J^{PC} of any operator inserted, this *smearing* must be charge and parity positive. The parity and charge conjugation symmetries of the fermion propagator may be used to infer the C and P symmetries of the correlation function obtained after performing the Grassmann integral. Operators for the most commonly used J^{PC} values are given in section 1.12

1.8 Meson Correlation Functions

We now look at the details of how the mesonic Green functions of the theory are constructed and the observable quantities obtained in a simulation. In lattice QCD simulations we calculate meson correlators of the form

$$C(\Gamma_{sk},\Gamma_{sc},x,0)\ =\ \langle 0|(\bar\psi\gamma_5\Gamma_{sk}\phi)(x)(\bar\psi(\gamma_4\Gamma_{sc}\gamma_5\gamma_4)^\dagger\phi)^\dagger(0)|0\rangle \tag{1.59}$$

$$
\begin{aligned}
&= \langle 0|(\bar{\psi}\Gamma'_{sk}\phi)(x)(\bar{\phi}\Gamma'_{sc}\psi)(0)|0\rangle && (1.60)\\
&= \langle 0|\mathcal{O}_{sk}(x)\mathcal{O}_{sc}(0)|0\rangle. && (1.61)
\end{aligned}
$$

where

$$
\begin{aligned}
\Gamma'_{sk} &= \gamma_5\Gamma_{sk} && (1.62)\\
\Gamma'_{sc} &= \Gamma_{sc}\gamma_5 && (1.63)
\end{aligned}
$$

Here the J^{PC} quantum numbers of the bilinears are chosen to match those of the particle under study, and the implicit γ_5 factors on Γ'_{sc} and Γ'_{sk} are a convention that is of use when dealing directly with the quark two-point functions as shown in the previous section. The two-point correlator is projected on to definite momentum via

$$
C_{\vec{p}}(\Gamma_{sk},\Gamma_{sc},t,0) = \sum_{\{x:x_0=t\}} C(\Gamma_{sk},\Gamma_{sc},x,0)e^{i\vec{p}.\vec{x}}. \qquad (1.64)
$$

1.9 Spectroscopy

Lattice spectroscopy is performed by analysing the zero momentum two-point function of the particle in question, to extract the rest energy.

Inserting a complete set of states $|n\rangle$ with the correct J^{PC} quantum numbers, and normalisation $2E_n$, we have

$$
C_t(\Gamma_{sk},\Gamma_{sc},t,0) = \sum_n \frac{\langle 0|\mathcal{O}_{sk}|n\rangle \langle n|\mathcal{O}_{sc}|0\rangle}{2E_n} e^{-E_n\frac{T}{2}} \cosh E_n(t-\frac{T}{2}). \qquad (1.65)
$$

Here the Minkowski e^{-iEt} time dependence of a Green function has been analytically continued to a decaying exponential. In the periodic lattice this is modified to a cosh dependence. This model is fitted to the data, and the statistical error due to a finite ensemble estimated using, for example, the bootstrap algorithm [17].

Note that if $t \gg \frac{2\log|\frac{\langle n|\mathcal{O}\rangle}{\langle 1|\mathcal{O}\rangle}|}{E_n - E_1}$ $\forall\, n$ then the correlator behaves as though only the lowest eigenstate of quantum numbers J^{PC} contributes to the sum. The mass of the ground state with quantum numbers J^{PC} can therefore be found from the asymptotic time dependence. Clearly in a lattice simulation with a finite temporal lattice extent it is desirable that the asymptotic region is reached as early as possible for the analysis of the ground state. This point will be returned to in a discussion of smeared operators for state $|m\rangle$, retaining the desired J^{PC} such that the overlaps $\langle n|\mathcal{O}_s\rangle$ are minimal for $n \neq m$. When more than one smearing is used, simultaneous fits to multiple superposed states (multi-exponential fits) may be performed.

1.9.1 Noise propagation in meson correlators

Based upon work by Kronfeld [18], and lectures given by Weingarten [19], we note that the variance in the correlation function of the bilinear $\bar{\psi}\Gamma\psi$ in a finite Monte Carlo simulation is

$$\sigma^2 = \langle\{\bar{\psi}\Gamma\psi(x)\}^2\{\bar{\psi}\Gamma\psi(0)\}^2\rangle - \langle\{\bar{\psi}\Gamma\psi(x)\}\{\bar{\psi}\Gamma\psi(0)\}\rangle^2. \tag{1.66}$$

The first part of the above has an overall $PC = ++$ source and sink, and so the variance

$$\sigma^2 \sim e^{-2m_{ps}t} - e^{-2m_\Gamma t} \overset{t\to\infty}{\propto} e^{-2m_{ps}t}. \tag{1.67}$$

Thus the signal to noise in mesonic correlation functions decays asymptotically as $e^{-(m_\Gamma - m_{ps})t}$. All but the pseudoscalar states of the meson therefore suffer from an exponential growth of the noise at large times, with larger exponent for the higher excited states. The result of this is that smearing is critical for radially and orbitally excited states to give access to plateaux in the cleaner early timeslices.

1.10 Weak Matrix Elements

The relative timescales of weak and strong decays mean we can treat the eigenstates of the Standard Model as essentially the eigenstates of the pure QCD sector. The weak decay amplitudes of mesons can therefore be approximated by the weak part of the decay process coupled to the expectation of the weak current in the pure QCD bound state. Thus we define the pseudoscalar meson decay constant, a soft QCD prefactor for weak decays, as

$$\langle 0|A_\mu(0)|P(q_\mu)\rangle = f_P q_\mu, \tag{1.68}$$

where A_μ is the renormalised axial vector current

$$A_\mu = Z_A(\bar{\psi}\gamma_5\gamma_\mu\psi)_{\mathrm{latt}}, \tag{1.69}$$

and the normalisation of the physical pseudoscalar state $|P(q_\mu)\rangle$ is

$$\langle P(q_\mu)|P(q'_\mu)\rangle = 2E(q_\mu)(2\pi)^3\delta^4(q-q'). \tag{1.70}$$

Note that a reasonably common alternative definition of f_P exists which differs by $\frac{1}{\sqrt{2}}$. Also, when the normalisation of the states is made unity, as in for example HQET, there is an additional $\sqrt{\frac{1}{E}}$ on the right hand side of (1.68).

1.11 Angular Momentum on a Cubic Lattice

It is clear both definite charge and parity quantum number operators may be defined on the lattice. However the breaking of Lorentz symmetry to hypercubic symmetry in lattice QCD, which is only restored in the continuum limit, means that it is not clear how to put an operator of arbitrary angular momentum on the lattice. The results of an irreducible representation decomposition are given in references [20, 21].

I shall give a more detailed description of how to form angular momentum operators on a cubic lattice. The representations and character structure of the cubic group used in the following can be found in appendix D of Cornwell [22]. For simplicity I consider only integer angular momentum.

1.11.1 Angular Momentum States and Representations of Rotations

For each $J \in \mathbb{N}$ we can define a homomorphism $D^J : SO(3) \to SU(2J+1)$ such that the spherical harmonics P^J_m are transformed under a rotation with Euler angles α, β, γ according to

$$R(\alpha,\beta,\gamma)P^J_m(\theta,\phi) = D^J_{mn}(R)P^J_n(\theta,\phi). \tag{1.71}$$

Such a homomorphism $D^J(R)$ is in fact an irreducible representation of the ordinary rotation group SO(3). It is necessary to simplify the following treatment by noting that the spherical harmonics may be expressed as functions of cartesian coordinates (x, y, z) lying on the unit sphere $x^2 + y^2 + z^2 = 1$. With these coordinates we write

$$X_{\pm} = \frac{x \pm iy}{\sqrt{2}}, \tag{1.72}$$

giving a form of the spherical harmonics that is particularly suited to dealing with cubic symmetries:

$$P^0_0 = 1, \tag{1.73}$$

$$\begin{aligned} P^1_0 &= Nz, \\ P^1_1 &= NX_+, \quad P^1_{-1} = NX_-, \end{aligned} \tag{1.74}$$

$$\begin{aligned} P^2_0 &= M(3z^2-1), \\ P^2_1 &= -2MzX_+, \quad P^2_{-1} = 2MzX_-, \\ P^2_2 &= \sqrt{2}MX^2_+, \quad P^2_{-2} = \sqrt{2}MX^2_-. \end{aligned} \tag{1.75}$$

A unitary transformation can be performed on the P^1's to yield the new basis

$$P^1_x = Nx, \quad P^1_y = Ny, \quad P^1_z = Nz. \tag{1.76}$$

N and M are irrelevant normalisation constants.

1.11.2 The Lattice Rotation Group O_h

In a lattice calculation, the rotational symmetry present is the cubic group O_h, naturally a subgroup of the full rotation group.

Figure 1.1: Axes of cubic rotational symmetry group

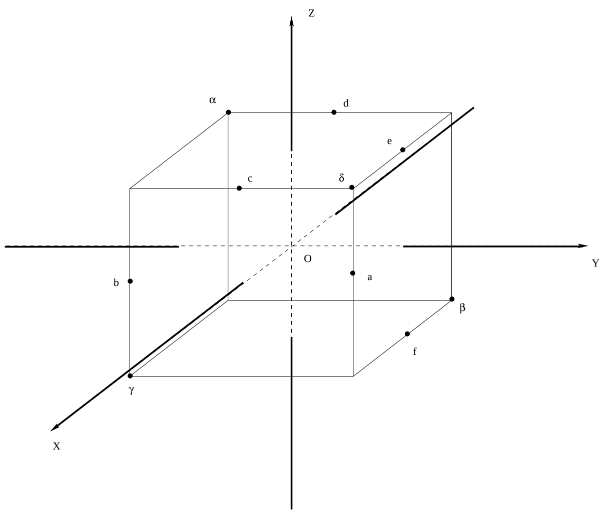

Consider the cube, Figure 1.1, centred at the origin, with the ordinate axes at face centres. Ignoring improper rotations, the group O_h is the one formed by the multiplicative span of the set of rotations about axes through the centre by

- $\frac{\pi}{2}$ about the face centres
- π about the edge centres
- $\frac{2\pi}{3}$ about the corners

Note that all of these rotations map the x, y, z axes onto some permutation thereof, with inversion allowed. I shall list one rotation matrix, operating on the column vector

$$\vec{r} = \begin{pmatrix} x \\ y \\ z \end{pmatrix}, \tag{1.77}$$

from each of the five proper conjugacy classes of O_h, $\{\mathcal{C}_1, \ldots, \mathcal{C}_5\}$. These rotations will be used to find the character of angular momentum representations D^J_h in each of the conjugacy classes of O_h. Below the rotation C_{na} refers to a $\frac{2\pi}{n}$ rotation about the axis from the origin passing through point a in Figure 1.1.

$$
\begin{aligned}
R(\,\mathbf{E}\, \in \mathcal{C}_1) &= \begin{bmatrix} 1 & 0 & 0 \\ 0 & 1 & 0 \\ 0 & 0 & 1 \end{bmatrix} & R(C_{3\delta} \in \mathcal{C}_2) &= \begin{bmatrix} 0 & 1 & 0 \\ 0 & 0 & 1 \\ 1 & 0 & 0 \end{bmatrix} \\
R(C_{2z} \in \mathcal{C}_3) &= \begin{bmatrix} -1 & 0 & 0 \\ 0 & -1 & 0 \\ 0 & 0 & 1 \end{bmatrix} & R(C_{4z}^{-1} \in \mathcal{C}_4) &= \begin{bmatrix} 0 & -1 & 0 \\ 1 & 0 & 0 \\ 0 & 0 & 1 \end{bmatrix} \\
R(C_{2b} \in \mathcal{C}_5) &= \begin{bmatrix} 0 & -1 & 0 \\ -1 & 0 & 0 \\ 0 & 0 & -1 \end{bmatrix}
\end{aligned}
\tag{1.78}
$$

The characters for the irreducible representations of the proper subgroup of O_h are given in Table 1.2, where A, E, T label one, two and three dimensional representations respectively.

Table 1.2: Character table for cubic rotation group O_h

		$\mathcal{C}_1$	$\mathcal{C}_2$	$\mathcal{C}_3$	$\mathcal{C}_4$	$\mathcal{C}_5$
Γ^1	A_1	1	1	1	1	1
Γ^2	A_2	1	1	1	-1	-1
Γ^3	E	2	-1	2	0	0
Γ^4	T_1	3	0	-1	1	-1
Γ^5	T_2	3	0	-1	-1	1

The multiplicities of the classes $\{\mathcal{C}_1, \mathcal{C}_2, \mathcal{C}_3, \mathcal{C}_4, \mathcal{C}_5, \}$ are $\{1, 8, 3, 6, 6\}$ respectively, allowing the representation orthogonality theorems to be applied.

Cornwell [22] lists sample representations, however it is not instructive to do more here than comment that the A_1 representation is always unity, the T_1 may be represented by the rotations themselves, and a particular representation for T_2 is given. As can be seen, the characters of T_1 and T_2 differ only in the classes $\mathcal{C}_5$ and $\mathcal{C}_4$, which correspond to conjugates of $x \leftrightarrow y$ and $x \leftrightarrow -y$ respectively. The sign of the character tells us that in an appropriate basis the T_{1z} component is anti-symmetric under $x \leftrightarrow y$ while the T_{2z} component is symmetric and vice versa for $x \leftrightarrow -y$.

1.11.3 Angular Momentum In the Restricted Symmetry of the Lattice

We now restrict the domain of D^J to the set O_h, calling the restricted homomorphism D^J_h. In general we find that D^J_h, while clearly a representation of O_h, is not irreducible. In simple terms the cubic structure does not have sufficient angular granularity to irreducibly support arbitrarily high angular momenta.

It is necessary to decompose D^J_h into irreducible representations of the cubic group in order to find out how our operator for a given angular momentum should transform under the cubic symmetry group. The manual calculation of this rapidly becomes a tedious task with increasing J as it involves the computation of the matrices $D^J(R)$ for one R in each of the classes $\{\mathcal{C}_2, \mathcal{C}_4, \mathcal{C}_5\}$. The traces of these matrices give the characters for each of the four non-trivial classes of proper O_h rotations. The decomposition into irreducible representations can then be easily performed using character tables and multiplicities for O_h and a basic representation theory textbook.

With the spherical harmonic bases given previously it is trivial to show that D^0_h is always unity, and that matrices of D^1_h are in fact the same as the rotation matrices given. Taking the characters from the representative matrices shows without further computation that $J = 0$ lies in the A_1 representation and $J = 1$ lies in the T_1 representation from inspection of the character table.

The calculation for $J = 2$ is somewhat less trivial, but is worthwhile since this is the first representation of rotations that becomes reducible on restriction to O_h.

To evaluate the D_h^2 matrices for each of the three rotations given above we write

$$P_m^2(x', y', z') = D_{mn}^2(R) P_n^2(x, y, z), \tag{1.79}$$

where

$$\begin{pmatrix} x' \\ y' \\ z' \end{pmatrix} = \begin{pmatrix} R_{11} & R_{12} & R_{13} \\ R_{21} & R_{22} & R_{23} \\ R_{31} & R_{32} & R_{33} \end{pmatrix} \begin{pmatrix} x \\ y \\ z \end{pmatrix}. \tag{1.80}$$

Solving this for each of the three rotations we obtain the characters of $J = 2$ in O_h. Using the listed sample elements from each conjugacy class we obtain that the representation of these as:

$$D^2(\mathbf{E} \in \mathcal{C}_\mathbf{1}) = \mathbb{I}_{5\times 5} \quad ; \quad \chi = 5, \tag{1.81}$$

$$D^2(C_{4z}^{-1} \in \mathcal{C}_4) = \mathrm{diag}(-1, -i, 1, i, -1) \quad ; \quad \chi = -1, \tag{1.82}$$

$$D^2(C_{2z} \in \mathcal{C}_3) = D^2(C_{4z})^{-2} = \mathrm{diag}(1, -1, 1, -1, 1) \quad ; \quad \chi = 1, \tag{1.83}$$

$$D^2(C_{2b} \in \mathcal{C}_5) = \begin{bmatrix} 0 & 0 & 0 & 0 & -1 \\ 0 & 0 & 0 & -i & 0 \\ 0 & 0 & 1 & 0 & 0 \\ 0 & i & 0 & 0 & 0 \\ -1 & 0 & 0 & 0 & 0 \end{bmatrix} \quad ; \quad \chi = 1. \tag{1.84}$$

Finally I compute only the diagonal elements of

$$D^2(C_{3\delta} \in \mathcal{C}_2) = \begin{bmatrix} -\frac{1}{4} & ? & ? & ? & ? \\ ? & -\frac{i}{2} & ? & ? & ? \\ ? & ? & -\frac{1}{2} & ? & ? \\ ? & ? & ? & \frac{i}{2} & ? \\ ? & ? & ? & ? & -\frac{1}{4} \end{bmatrix} \quad ; \quad \chi = -1. \tag{1.85}$$

The characters obtained are given in Table 1.3:

In principle, the general calculation would use the character orthogonality theo-

Table 1.3: Characters of lattice representation of $J = 2$

	$\mathcal{C}_1$	$\mathcal{C}_2$	$\mathcal{C}_3$	$\mathcal{C}_4$	$\mathcal{C}_5$
D^2_h	5	-1	1	-1	1

rems to calculate the multiplicity of each irreducible representation in this general representation. However, for brevity, we work back from the answer and note that these characters are the sum of those of the T_2 and E representations. Using the uniqueness of the decomposition we immediately conclude that:

$$D^{J=2}_{O_h} = T_2 \oplus E. \tag{1.86}$$

Operators in either the T_2 or E reps will therefore produce the same degenerate $J = 2$ ground state as $a \to 0$, with the appropriate PC values for the operator. The decomposition for higher angular momentum states is more complicated, and can be found in [21].

1.12 Meson Operators

Table 1.4 gives some of the operators used in this thesis. It is worth noting, recalling the discussion of irreducible representations of O_h, that given two three component operators A_i and B_i transforming under the O_h itself we can construct both T_1 and T_2 operators.

For T_1 there are the two obvious operators, i.e. A_i and B_i, while the cross product $\epsilon_{ijk}A_jB_k$ transforms as vector also, (and trivially is anti-symmetric), giving rise to the 1^{++} operator.

For the T_2 representation, one immediately sees that $A_iB_j + A_jB_i$ has the mentioned symmetry in $x \leftrightarrow y$. A bit of thought also gives the correct character for $x \to -x$, $y \to -y$ giving class $\mathcal{C}_3$. The character for the identity is trivial while the cyclic perm $x \to y \to z \to x$ is completely off diagonal giving character zero and completing the proof that the operators lie in the T_2 representation. Similar

Table 1.4: Meson operators

State	J^{PC}	Operators
$^1S_0$	0^{-+}	$\bar{\psi}\gamma_5\psi$
$^3S_1$	1^{--}	$\bar{\psi}\gamma_i\psi$
$^1P_1$	1^{+-}	$\bar{\psi}\sigma_{ij}\psi$, $\bar{\psi}\gamma_5\Delta_i\psi$
$^3P_0$	0^{++}	$\bar{\psi}\psi$, $\bar{\psi}\sum\gamma_i\Delta_i\psi$
$^3P_1$	1^{++}	$\bar{\psi}\gamma_i\gamma_5\psi$, $\bar{\psi}\{\gamma_i\Delta_j - \gamma_j\Delta_j\}\psi$
$^3P_2$	2^{++}	$\bar{\psi}\{\gamma_i\Delta_i - \gamma_j\Delta_j\}\psi$ E rep
		$\bar{\psi}\{\gamma_i\Delta_j + \gamma_j\Delta_i\}\psi$ T rep

arguments can be made for the E representation operators.

1.13 Smeared Operators

The generic meson operator has non-zero overlap with all bound states with the approriate J^{PC}, and asymptotically approximates the ground state. As mentioned in section 1.7, a gauge covariant extended source can be used in the matrix inversion. This changes the overlap of the correlator with the eigenstates, so that if the smearing function is chosen to approximate the ground state wavefunction, then the coefficients $\langle n|\mathcal{O}\rangle$ are such that the ground state dominance occurs earlier. In order to quantify this somewhat, I consider the correlation function formed with one contaminating excited state, and ignore the periodicity of the lattice.

$$C_t = Ae^{-E_1 t} + Be^{-E_2 t} \tag{1.87}$$

The effective mass of this correlator is loosely the negative of the derivative of the log:

$$M_t \simeq -\frac{d}{dt}\log C_t = \frac{E_1 + \frac{B}{A}E_2 e^{-(E_2-E_1)t}}{1 + \frac{B}{A}e^{-(E_2-E_1)t}}. \tag{1.88}$$

By inspection it can be seen that there are two distinct cases for the approach to the plateau:

- $\frac{B}{A} > 0$ approach from above

- $\frac{B}{A} < 0$ approach from below, vertical asymptote at $t = \frac{\log|\frac{B}{A}|}{E_2 - E_1}$

Note that if the same smearing function and operator is used at the source and the sink then the correlator is positive definite and that $\frac{B}{A}$ is always positive. Several techniques have commonly been used to construct gauge invariant smeared operators.

1.13.1 Jacobi Smearing

Jacobi smearing [23] is a numerically efficient method of approximating Wuppertal smearing [24], thereby covariantly producing a space filling "bell" function, as an approximation to the solution of the spatial scalar Klein Gordon equation.

The Jacobi operator is defined as

$$\mathcal{J}\psi(x) = \sum_{j=x,y,z} \left[U_j(x)\psi(x+\hat{j}) + U_j^\dagger(x-\hat{j})\psi(x-\hat{j}) \right], \tag{1.89}$$

and the smeared field

$$\psi' = e^{-4N(\kappa_s - \kappa_0)}(1 + \kappa_s \mathcal{J})^N \psi(x), \tag{1.90}$$

where $\kappa_0 = 0.185$.

Note that sink Jacobi smearing has a numerical expense of approximately 100 half-parity matrix multiplies. In practice, the relative numerical expense is higher since the fermion matrix multiply is a heavily optimised routine. Since the light propagators typically take between 300 and 1000 matrix multiplies to converge, and heavy Wilson propagators are generated with between 50 and 100 multiplies, it is clear that this form of smearing can make up a significant fraction of the cost of a quenched matrix element calculation. The following *fuzzing* technique uses a simpler non-iterative method at the cost of foresaking the space filling property.

1.13.2 Fuzzed Operators

The cost of iteratively applying the Jacobi operator N times at the sink is somewhat prohibitive. Lacock and Michael [25] suggested the use of a covariantly transported "cross" using low noise *fuzzed* links.

Figure 1.2: Fuzzed smearing

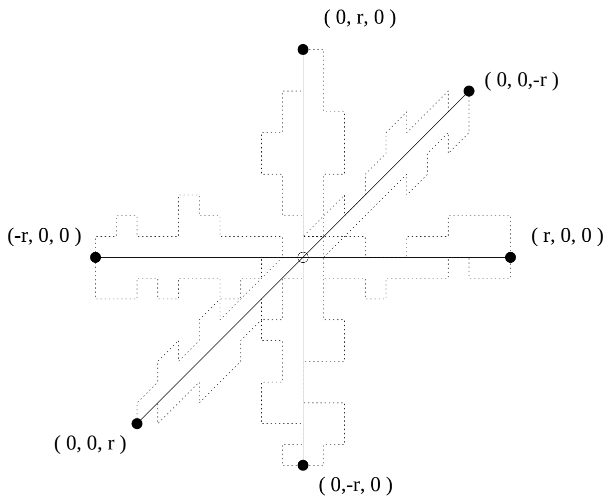

The fuzzing prescription iterates

$$U'_j(x) = c\, U_j(x) + \sum_{i \neq j} \left[U_i^{\mathrm{Staple}}(x, x+\hat{j}) + U_{-i}^{\mathrm{Staple}}(x, x+\hat{j}) \right], \tag{1.91}$$

$$U_j(x) = \mathbb{P}\, U'_j(x), \tag{1.92}$$

where $\mathbb{P}$ is a projection onto SU(3) (not closed under addition) by Cabibbo Marinari maximisation of $\mathrm{Tr}[U_j^\dagger U'_j]$ with six hits on each SU(2) subgroup. Typically c is set to 2.0, and there are 5 iterations performed. These fuzzed links are used to transport the quark field by some number of sites N along each of the spatial axes.

$$\psi'(x) = \sum_{i=x,y,z} \left[\prod_{n=1}^{r} U_i(x+(n-1)\hat{i}) \right] \times \psi(x+r\hat{i}) + \left[\prod_{n=1}^{r} U_i^\dagger(x-n\hat{i}) \right] \times \psi(x-r\hat{i}) \tag{1.93}$$

The fuzzing radius, r, is chosen to minimise the contamination of the ground state operator, and is taken as 8 at $\beta = 6.2$ for light quark propagators. Systems containing heavy quarks have smaller wave functions and a fuzzing radius of 4 or 5 should be used with the above lattice. The cost of sink fuzzing to radius 8 is approximately 16 half-parity matrix multiplies leaving the sink smearing a significantly smaller fraction of the total cost of a spectrum calculation than was the case with Jacobi smearing. Fuzzing is pictorially represented as a sum of transportation paths in Figure 1.2

1.13.3 Multi-correlator fits

Given N operators $\mathcal{O}_i$ (e.g. different smearings) for a given J^{PC} state, it is possible form the correlation matrix between the operator sets.

$$C_{ij}(t) = \sum_x \left\langle \mathcal{O}_i(t,x) \quad | \quad \mathcal{O}_j^\dagger(0) \right\rangle \tag{1.94}$$

To extract more precise lattice observables, either the row with local sink, or the whole correlator matrix, may be simultaneously fitted to N states providing the operators have sufficiently differing overlaps with the eigenstates:

- Row fit model - $2N$ parameter fit to N channels

$$C_{li} = \sum_{n=1}^{N} A_i^n \left[e^{-E_n t} + e^{E_n (t - \frac{T}{2})} \right]. \tag{1.95}$$

- Matrix fit model - $2N$ parameter fit to N^2 channels

$$C_{ij} = \sum_{n=1}^{N} A_i^n A_j^{n*} \left[e^{-E_n t} + e^{E_n (t - \frac{T}{2})} \right]. \tag{1.96}$$

The most obvious basis to attempt to use is the diagonal one, where one smeared operator is defined with wavefunction approximating each of the radially excited states. This requires, however, successively increasing numbers of nodes in the wavefunction for the excited states, which is difficult to achieve gauge covariantly, and as a result has only been performed in gauge-fixed NRQCD calculations, such as [26].

Although it appears that the more constrained matrix fit should be superior, the low noise of the local sink compared with smeared sinks means that it is frequently more effective to use the row model for spectroscopy. It is worth noting that, in addition to possible radial excitation spectrum calculations, the multi-state methods are useful in stabilising the fitted value for the ground state with respect to the fit range, and in giving useful information from the cleaner early timeslices in excited states. In general, from an N-state fit to N sufficiently distinct correlators, there are $N-1$ well determined states, and one which is fit-range dependent.

1.14 Heavy Wilson Quarks

The simulation of heavy quarks generally poses a problem for the Wilson action and its variants. The reason for this is essentially that the lattice mass of a quark $ma \geq 1$ so that higher dimension operators (such as $m^n \mathcal{O}_i$) can have large contributions. In principle, the basis of operators in the Lüscher improvement scheme could be extended to higher dimensions, however the non-perturbative determination of the improvement coefficients and operator mixings becomes exceedingly difficult for $O(a^2)$ improvement and above.

In order to show the discrepancies of the Wilson action at large lattice quark mass, consider the quark propagator in the free field. Note that the clover term is zero in the free field, so that these arguments apply equally to all $O(a)$ improvement schemes. The arguments here are a generalisation to non-zero momentum of those given in Montvay and Münster [4] for the rest energy of a Wilson quark.

1.14.1 Free Field Dispersion Relation

The Wilson fermion matrix in momentum space is

$$\begin{array}{rcl} M(p_\mu) & = & m_0 + 4r - \frac{r}{2}\sum_\mu 2\cos p_\mu + \frac{1}{2}\sum_\mu 2i\gamma_\mu \sin p_\mu \\ & = & m_0 \quad + \quad r\sum_\mu 2\sin^2\frac{p_\mu}{2} \quad + \quad i\sum_\mu \gamma_\mu \sin p_\mu \end{array}. \tag{1.97}$$

We define modified momenta $\tilde{k}_\mu$ and $\bar{k}_\mu$ which reduce to p_μ as $p_\mu \to 0$, but have different behaviour at $p_\mu = \frac{\pi}{a}$:

$$\tilde{k}_\mu = 2\sin\frac{p_\mu}{2} \tag{1.98}$$

$$\bar{k}_\mu = \sin p_\mu \tag{1.99}$$

After squaring up with the complex conjugate, we can write the denominator of the inverse matrix in momentum space as

$$(m_0 + \tfrac{1}{2}\tilde{k}^2)^2 + \bar{k}^2. \tag{1.100}$$

The energy of the quark E in Euclidean space is $E = -ip_4$, and we define $\tilde{E} = 2\sinh\frac{E}{2} = i\tilde{k}_4$ and similarly $\bar{E}$. The on-shell energy at a given momentum is given by the pole in the propagator, i.e. the zero of (1.100) . We must therefore solve

$$(m_0 + \tfrac{1}{2}\tilde{k}_i^2 - \tfrac{1}{2}\tilde{E}^2)^2 + \bar{k}^2 - \bar{E}^2 = 0, \tag{1.101}$$

$$\Rightarrow (m_0 + \tfrac{1}{2}\tilde{k}_i^2 - A)^2 + \bar{k}^2 - 2A - A^2 = 0, \tag{1.102}$$

where $A = \cosh E - 1 = 2\sinh^2\frac{E}{2}$. This can trivially be solved for A, giving the energy momentum relation

$$\cosh E(p) = 1 + \frac{1}{2}\frac{(m_0 + \frac{1}{2}\tilde{k}_i^2)^2 + \bar{k}_i^2}{1 + m_0 + \frac{1}{2}\tilde{k}_i^2}. \tag{1.103}$$

The rest energy is therefore

$$m_1 \equiv E(0) = \log(1 + m_0), \tag{1.104}$$

while the kinetic mass,

$$(2m_2)^{-1} \equiv \frac{\partial E}{\partial(p^2)}|_{\vec{p}=0}, \tag{1.105}$$

is easily found using the low momentum limit of $\tilde{k}$ and $\bar{k}$ to be

$$m_2 = \frac{2m_0(1+m_0)(2+m_0)}{2+4m_0+m_0^2}. \tag{1.106}$$

It is worth noting that for $m_0 \ll 1$, $m_2 \sim m_1 \sim m_0$, and that m_2 can be written in terms of m_1 as

$$m_2 = e^{m_1}\frac{\sinh m_1}{1+\sinh m_1}. \tag{1.107}$$

1.14.2 Heavy Quark Discretisation Effects

The discussion of the previous section highlights the problems found if the lattice quark mass is too large. In general, the two mass definitions agree for lattice masses $m_1 \leq 0.5$. On current lattices, however, the scale $a^{-1} \sim 2 - 2.7$ GeV, which means that the charm quark (1.5 GeV) is just above the acceptable level, while the beauty quark (4.5 GeV) is well outwith the range that can be directly simulated. We therefore need to consider what can be done in the regime where $m_1 \geq 0.5$.

Firstly, it is clear that we have to accept the presence of significant discretisation effects, and that continuum results can only be obtained from controlled extrapolation in the lattice spacing.

Secondly we are free to choose either of the above mass prescriptions to define the quark mass; given our first point, and that the definitions rapidly become equivalent as we approach the continuum, we may choose the prescription which has the flatter approach.

The kinetic (i.e. inertial) mass [27] more strongly influences the dynamics of the bound system than the pole mass, since the kinetic term determines the spin independent spectrum. Based on both experience and prejudice, it is common to choose to use the kinetic mass to define the quark mass in heavy-quark extrapolations. We note that it has been demonstrated by Aoki et al [28] that the same continuum results are obtained with both mass prescriptions. With only one or two β values the use of the kinetic mass to get closer to scaling behaviour, with the acceptance of increased statistical error, is the best way to proceed.

Chapter 2

Bound States of Heavy Quarks

2.1 Heavy Quark Bound States

The topic of this thesis is the phenomenology of systems containing heavy quarks. These systems have $M_Q \gg O(\Lambda_{QCD})$, the typical exchange energy, allowing the prediction of the bound state properties due to the non-relativistic nature of the heavy quark's motion.

In quarkonium systems both quarks are non-relativistic and the exchange degrees of freedom have an effectively instantaneous characteristic timescale. The system can therefore be understood in terms of a spherically symmetric relative potential $V(r)$, with an effective Hamiltonian written in terms of this potential, giving the usual simultaneous $E,\ J,\ J_z$ eigenstate basis.

For heavy-light systems the light degrees of freedom are essentially independent of the spin and flavour of the heavy quark, allowing symmetries to be applied when comparing heavy-light systems. The PDG experimental spectrum values have been tabulated in appendix A.

In this chapter I shall obtain the potential from the S-matrix with non-relativistic asymptotic states using the inverse of the Born approximation, with the spin-dependent potential obtained from the leading relativistic corrections to the S-matrix. This leads to the Breit Fermi Hamiltonian, and allows an understanding of the angular momentum structure of quarkonium.

Asymptotic freedom allows the short distance potential to be inferred from tree-level scattering, while the long range confining potential involves the non-perturbative sector of the S-matrix, and we are reduced to guessing the form and Dirac structure in phenomenological potential models in order to reproduce the observed hadrons. Using common potentials, the expected form for the mass dependence of the quarkonium splittings is obtained.

The second half of the Chapter studies heavy-light mesons, and I derive the formal expression of the spin and flavour symmmetries, namely Heavy Quark Effective Theory. Both HQET and Hamiltonian models are then applied to understand the angular momentum structure and mass dependence of the splittings in heavy-light mesons.

We commence with the non-relativistic QCD potential.

2.2 QCD Potential from the S-Matrix

In this section we consider the S-matrix for low momentum external states, and relate this to the effective QCD potential. The time independent Schroedinger equation for a two particle system with central potential $V(|\vec{r}_1 - \vec{r}_2|)$ in the centre of mass frame with relative coordinate x and reduced mass $\mu = \frac{m}{2}$ is

$$\mathcal{H}\psi(x) = \left[-\frac{\nabla^2}{2\mu} + V(x)\right]\psi(x) = E\psi(x). \tag{2.1}$$

The inelastic scattering problem requires the solution of the time independent Schroedinger equation subject to the boundary condition

$$\psi(x) \to e^{ik_0.x} + F(\theta,\phi)\frac{e^{ikr}}{r} \tag{2.2}$$

at large distances, where $k_0 = \mu(v_1 - v_2) = mv_1$ is the momentum of one of the incident particles, and $k = |k_0|$. Particle flux arguments give that the differential cross-section is then

$$\frac{d\sigma}{d\Omega} = |F(\theta,\phi)|^2 \tag{2.3}$$

$$= \frac{1}{64\pi^2}|\mathcal{M}_{fi}|^2. \tag{2.4}$$

Here $\mathcal{M}_{fi}$ is the Feynman amplitude for the scattering evaluated with spinor normalisation $u^\dagger u = \sqrt{\frac{1}{2m}}$ The wavefunction is the solution of the integral equation

$$\psi(r) = e^{ik_0.r} - \int_{\mathcal{R}} d^3x V(x)\psi(x)G(r-x), \tag{2.5}$$

where $\mathcal{R}$ is the region containing the potential, and $G(y)$ is the Green function of the Helmholtz operator $\nabla^2 + k^2$, using Appendix B,

$$G(p) = \frac{1}{k^2 - p^2}, \tag{2.6}$$

$$G(r) = -\frac{1}{4\pi}\frac{e^{ikr}}{r}. \tag{2.7}$$

Assuming that the potential is such that the scattering amplitude is small, then we can approximate the wavefunction in the integral by $e^{ik_0.x}$ making the first order Born approximation:

$$\psi(r) = e^{ik_0.r} + \frac{1}{4\pi}\int_{\mathcal{R}} d^3x V(x) e^{ik_0.x}\frac{e^{ik|r-x|}}{|r-x|}. \tag{2.8}$$

If we assume that the interaction takes place predominantly within some scattering centre, we can take limit $|r| \gg |x|$ and set $|r-x| \simeq r(1 - \frac{r.x}{r^2})$ and writing $k_1 = k\hat{r}$ we obtain

$$\psi(r) \simeq e^{ik_0.r} - \frac{e^{ikr}}{r}\frac{1}{4\pi}\int_{\mathcal{R}} d^3x V(x) e^{i(k_0-k_1).x}. \tag{2.9}$$

Thus the S-matrix with non-relativistic ($k \ll m$) external states in the centre of momentum frame, and the effective potential of a field theory are related via a Fourier transform in the transferred momentum $k = k_1 - k_0$:

$$V(x) = -(2\pi)^3 \int d^3k e^{-ik.x} M_{fi}(k). \tag{2.10}$$

2.2.1 Potential From Tree Level S-Matrix

We can apply tree level perturbation theory to calculate the S-matrix for quark-antiquark scattering and find the leading perturbative contribution to the QCD potential (dominant at high momentum and hence short-distance due to asymptotic freedom).

At tree level the $q\bar{q}$ scattering diagrams are the one gluon exchange and the annihilation diagrams Figure 2.1 and Figure 2.2.

Figure 2.1: Scattering by one gluon exchange

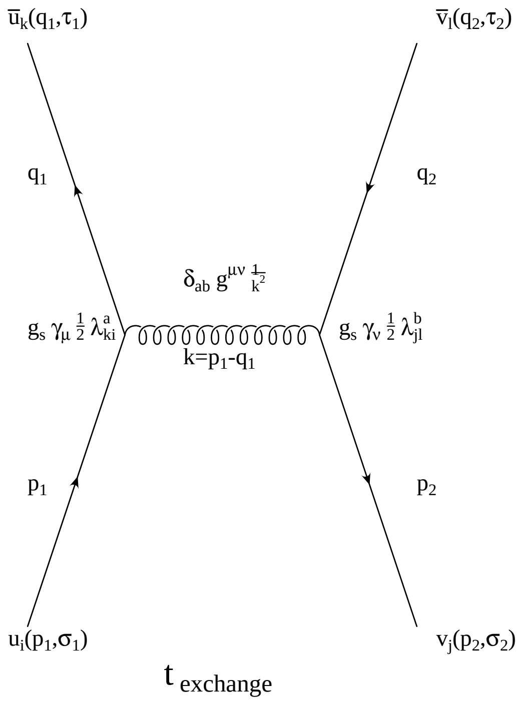

In the rest of this chapter we denote the momentum transfer $k = p_1 - q_1 = q_2 - p_2$ and the incident 3-momentum $\mathbf{p} = \mathbf{p_1} = -\mathbf{p_2}$. The exchange Feynman amplitude

Figure 2.2: Scattering by one gluon annhiliation

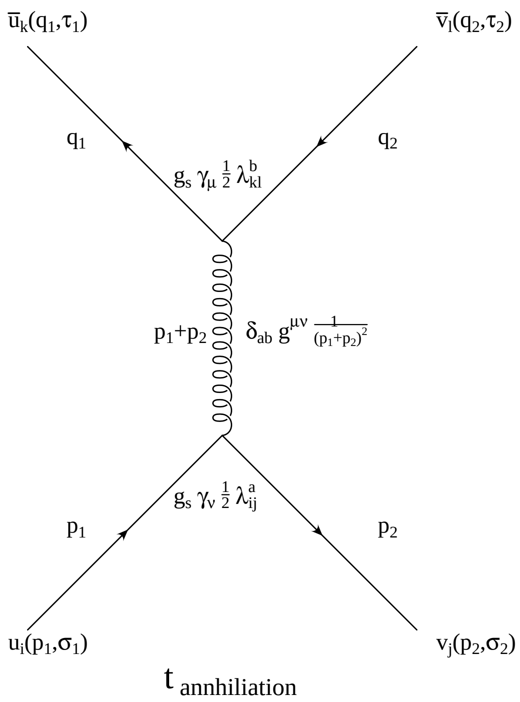

in Feynman gauge is

$$t_{\text{exch}} = -\frac{g_s^2}{k^2}\frac{\lambda_{ki}^a}{2}\frac{\lambda_{jl}^a}{2}\bar{u}_k(q_1,\tau_1)\gamma_\mu u_i(p_1,\sigma_1)\bar{v}_j(p_2,\sigma_2)\gamma^\mu v_l(q_2,\tau_2). \tag{2.11}$$

The annihilation graph has the amplitude

$$t_{\text{ann}} = \frac{g_s^2}{(p_1+p_2)^2}\frac{\lambda_{ji}^a}{2}\frac{\lambda_{kl}^a}{2}\bar{u}_k(q_1,\tau_1)\gamma_\mu v_l(q_2,\tau_2)\bar{v}_j(p_2,\sigma_2)\gamma^\mu u_i(p_1,\sigma_1). \tag{2.12}$$

Here the gluon propagator $\frac{g_{\mu\nu}}{(p_1+p_2)^2} \simeq \frac{g_{\mu\nu}}{(2m)^2}$ leaves this process $O(\frac{k^2}{m^2})$ suppressed with respect to the exchange process and is therefore a relativistic correction to the static potential. In order to define a gauge-invariant scalar potential for QCD we must restrict the argument to the potential between colour singlet quark anti-quark pairs $\frac{1}{\sqrt{3}}(r\bar{r}+b\bar{b}+g\bar{g})$. This essentially means we must consider the Fourier transform of the S-matrix for colour singlet quark anti-quark scattering, and so we set the external state to be

$$u_i(p_1,\sigma_1)\bar{v}_j(p_2,\sigma_2) = u(p_1,\sigma_1)\bar{v}(p_2,\sigma_2)\frac{1}{\sqrt{3}}\delta_{ij}, \tag{2.13}$$

and

$$\bar{u}_k(q_1,\tau_1)v_l(q_2,\tau_2) = \bar{u}(q_1,\tau_1)v(q_2,\tau_2)\frac{1}{\sqrt{3}}\delta_{kl}. \tag{2.14}$$

This produces a colour factor in the amplitude of

$$\frac{1}{3}\mathrm{Tr}\left[\frac{\lambda^a}{2}\frac{\lambda^a}{2}\right] = \frac{1}{3}\frac{1}{2}\delta^{aa} = \frac{4}{3}. \tag{2.15}$$

Further, in the non-relativistic limit, the term

$$\bar{u}(q_1,\tau_1)\gamma_\mu u(p_1,\sigma_1)\bar{v}(p_2,\sigma_2)\gamma^\mu v(q_2,\tau_2) = \delta_{\tau_1\sigma_1}\delta_{\tau_2\sigma_2}, \tag{2.16}$$

producing helicity preserving delta functions.

The tree level potential obtained is therefore the Fourier transform of t_{exch},

$$V(r) = -\frac{1}{(2\pi)^3}\int d^3k e^{-ik.x}\frac{4}{3}\frac{g_s^2}{k^2}, \tag{2.17}$$

and hence

$$V(r) = -\frac{4}{3}\frac{g_s^2}{4\pi r} = -\frac{4}{3}\frac{\alpha_s}{r}. \tag{2.18}$$

Thus the short distance QCD potential is Coulombic in nature. The tree level S-matrix used to evaluate this potential is only valid in the high momentum transfer regime, and hence the potential is correct at short distances. To obtain the potential at larger distances higher order contributions to the S-matrix must be included when evaluating the potential. It is common to include some higher order effects by redefining the Coulombic part of the potential to contain the running coupling $\alpha_s(Q^2 = M^2_{\text{meson}})$ where

$$\alpha_s(Q^2) = \frac{3}{33-2n_f}\frac{4\pi}{\log\frac{Q^2}{\Lambda^2}}. \tag{2.19}$$

2.2.2 Potential from Non-perturbative S-Matrix

The long range (confining) potential is determined by the S-matrix in the soft regime, and as such is a non-perturbative feature. When considering the non-perturbative scattering amplitude, we must argue in the absence of full solutions about the general form and Lorentz structure. We write the transition matrix as

$$t_{fi} = \sum_{\Sigma=1,\gamma_5,\gamma_\mu,\gamma_5\gamma_\mu,\sigma_{\mu\nu}} t_\Sigma, \tag{2.20}$$

where

$$t_\sigma = \bar{u}(q_1,\tau_1)\Gamma_\Sigma u(p_1,\sigma_1)\bar{v}(p_2,\sigma_2)\Gamma_\Sigma v(q_2,\tau_2)K_\Sigma(k^2). \tag{2.21}$$

The various Lorentz structures that enter into this decomposition of the scattering amplitude do not necessarily arise from exchange of a fundamental particle, but have to be interpreted as the effective exchange of a particle of the appropriate Lorentz symmetry. We make the ansatz that the dominant contributions to the QCD phenomenological potential are the vector and scalar pure potential terms; this can be justified using the form of the static potentials to neglect the pseudoscalar, axial vector and tensor couplings, and the argument can be found in [29].

$$V_{NR}(r) = V_V(r) + V_S(r) \tag{2.22}$$

The Lorentz structure of the S-matrix is particularly important in deciding the form of the spin dependent corrections to the Hamiltonian associated with each part of the non-relativistic potential, and, following our ansatz, I compute these corrections for the scalar and vector coupling terms. Note that asymptotic freedom implies that the vector coupled potential should reduce to the tree level potential at short distances.

2.3 Spin Dependent Potential

In this section we derive the leading order spin-dependent relativistic corrections to the vector and scalar potentials. The Lorentz structure of the coupling determines how the relativistic small components enter the S-matrix and hence the potential. We write the low momentum Dirac spinors u and v in terms of two component spinors χ and χ^c:

$$u(p,\sigma_1) = \sqrt{\frac{E_p+m}{2m}} \begin{pmatrix} 1 \\ \frac{\sigma.p}{E_p+m} \end{pmatrix} \chi_{\sigma_1} \simeq \begin{pmatrix} 1 \\ \frac{\sigma.p}{2m} \end{pmatrix} \chi_{\sigma_1} \tag{2.23}$$

$$v(p,\sigma_2) = \sqrt{\frac{E_p+m}{2m}} \begin{pmatrix} \frac{\sigma.p}{E_p+m} \\ 1 \end{pmatrix} \chi^c_{\sigma_2} \simeq \begin{pmatrix} \frac{\sigma.p}{2m} \\ 1 \end{pmatrix} \chi^c_{\sigma_2}. \tag{2.24}$$

We define the expectation of each quark's spin as

$$S_1 = \frac{\sigma^1}{2} = \frac{\chi^\dagger_{\tau_1}\sigma\chi_{\sigma_1}}{2}, \tag{2.25}$$

$$S_2 = \frac{\sigma^2}{2} = \frac{\chi^\dagger_{\tau_2}\sigma\chi_{\sigma_2}}{2}, \tag{2.26}$$

and note for future use that the structure constants of SU(2) allow us to write

$$\sigma_i \sigma_j = \delta_{ij} + i\epsilon_{ijk}\sigma_k. \tag{2.27}$$

2.3.1 Spin Interaction with Scalar Potential

Here we consider the spin dependent corrections to the coupling, dropping spin independent relativistic corrections as they arise

$$\begin{aligned} t_S &\equiv \bar{u}(q_1,\tau_1)u(p_1,\sigma_1)\bar{v}(p_2,\sigma_2)v(q_2,\tau_2)K_S(k^2) && (2.28)\\ &= (u^\dagger\gamma_0 u)(v^\dagger\gamma_0 v)K_S(k^2) && (2.29)\\ &= -\left[\chi^\dagger(1-\frac{(\sigma.q_1)(\sigma.p_1)}{4m^2})\chi\right]\left[\chi^{c\dagger}(1-\frac{(\sigma.p_2)(\sigma.q_2)}{4m^2})\chi^c\right]K_S(k^2) && (2.30)\\ &= -\left[1-\frac{1}{2m^2}i\epsilon_{ijk}p_i k_j(\frac{\sigma^1}{2}+\frac{\sigma^2}{2})_k\right]K_S(k^2). && (2.31) \end{aligned}$$

Fourier transforming this amplitude produces the spin dependent contribution to the Hamiltonian

$$\mathcal{H}_{L.S}^{\text{scalar}} = -\frac{1}{2m^2 r}L.S\frac{\partial V_S(r)}{\partial r}. \tag{2.32}$$

In the above it is useful to note that the spin dependent part of $(\sigma.p)(\sigma.q)$ is

$$i\epsilon_{ijk}p_i q_j \sigma_k \equiv i(p\times q).\sigma \equiv -i(p\times(p-q)).\sigma \equiv -i(p\times k).\sigma, \tag{2.33}$$

giving rise to the spin-orbit term in a spherical potential since the resulting radial gradient in the Fourier transform produces a $(x\times p)$ orbital angular momentum operator.

2.3.2 Spin Interaction with Vector Potential

We consider the spin dependent relativistic corrections to the coupling

$$\begin{aligned} t_v &\equiv \bar{u}(q_1,\tau_1)\gamma_\mu u(p_1,\sigma_1)\bar{v}(p_2,\sigma_2)\gamma^\mu v(q_2,\tau_2)K_V(k^2) && (2.34)\\ &= [(u^\dagger u)(v^\dagger v)-(u^\dagger\gamma_0\gamma_i u)(v^\dagger\gamma_0\gamma_i v)]K_V(k^2) && (2.35) \end{aligned}$$

and hence, performing some manipulation we obtain,

$$\begin{aligned} t_v &= \left[\chi^\dagger(1+\tfrac{(\sigma.q_1)(\sigma.p_1)}{4m^2})\chi\right]\left[\chi^{c\dagger}(1+\tfrac{(\sigma.p_2)(\sigma.q_2)}{4m^2})\chi^c\right]K_V(k^2) \\ &- \tfrac{1}{4m^2}\left[\chi^\dagger(\sigma_i(\sigma.p_1)+(\sigma.q_1)\sigma_i)\chi\right]\left[\chi^{c\dagger}(\sigma_i(\sigma.q_2)+(\sigma.p_2)\sigma_i)\chi^c\right]K_V(k^2) \end{aligned} \tag{2.36}$$

$$\begin{aligned} t_v &= K_V(k^2)+\tfrac{i\epsilon_{ijk}p_ik_j\sigma_k^1+i\epsilon_{ijk}p_ik_j\sigma_k^2}{4m^2}K_V(k^2) \\ &+ \tfrac{[(2p-k)_i+i\epsilon_{ijk}k_j\sigma_k^1][(2p-k)_i+i\epsilon_{ilm}k_l\sigma_m^2]}{4m^2}K_V(k^2) \end{aligned} \tag{2.37}$$

$$t_v = \{1+\frac{3i\epsilon_{ijk}p_ik_j(\frac{\sigma^1}{2}+\frac{\sigma^2}{2})_k - 2(\frac{\sigma^1}{2}.\frac{\sigma^2}{2})k^2+2(\frac{\sigma_1}{2}.k)(\frac{\sigma_2}{2}.k)}{2m^2}\}K_V(k^2). \tag{2.38}$$

Fourier transforming this gives the following contributions to the Hamiltonian, having written $\nabla_i\nabla_jV = \left(\frac{x_ix_j}{r^2}-\frac{1}{3}\delta_{ij}\right)\left(V''-\frac{1}{r}V'\right)+\frac{1}{3}\delta_{ij}\nabla^2V$,

$$\mathcal{H}_{L.S} = \frac{3}{2m^2r}(r\times p).S\frac{\partial V_V(r)}{\partial r} = \frac{3}{2m^2r}L.S\frac{\partial V_V(r)}{\partial r}, \tag{2.39}$$

$$\mathcal{H}_{S.S} = \frac{2}{3m^2}S_1.S_2\nabla^2V_V(r), \tag{2.40}$$

$$\mathcal{H}_T = \frac{1}{12m^2}\mathcal{S}_{12}\left[\frac{1}{r}\frac{\partial}{\partial r}V_V(r)-\frac{\partial^2}{\partial r^2}V_V(r)\right], \tag{2.41}$$

$$\mathcal{S}_{12} = 12\left[\frac{(S_1.x)(S_2.x)}{r^2}-\frac{1}{3}S_1.S_2\right]. \tag{2.42}$$

Table 2.1: Tensor coupling spin factors

J	$l+1$	l	$l-1$
$\langle\mathcal{S}_{12}\rangle$	$-\frac{2l}{2l+3}$	2	$-\frac{2(l+1)}{2l-1}$

The tensor Hamiltonian $\mathcal{H}_T$ gives rise to the usual long range dipole-dipole force for a Coulombic vector exchange potential.

It can be shown (e.g. page 96 of Landau and Lifschitz [30] and Lucha [31]) that

$$\mathcal{S}_{12} = \frac{4}{(2l+3)(2l-1)}[S^2L^2 - \frac{3}{2}L\cdot S - 3(L\cdot S)^2]. \tag{2.43}$$

The definite eigenvalues of S_{12} can therefore be found easily in the $L-S$ coupled basis. For either $S=0$ or $L=0$ we immediately have $\mathcal{S}_{12}=0$. For $S=1$ we have the definite eigenvalues in Table 2.1.

It is worth noting that for a $\frac{1}{r}$ vector exchange potential the spin-spin Hamiltonian is a δ-function at the origin. When the running coupling is used in the potential, the slow variation is used to ignore the extra contributions to the divergence away from the origin.

2.3.3 Generalised Breit Fermi Hamiltonian

Collating the spin corrections of the last few sections we obtain the generalised Breit-Fermi Hamiltonian

$$\mathcal{H} = 2m + \frac{p^2}{2\mu} + V_{NR}(r) + \mathcal{H}_{L.S} + \mathcal{H}_{S.S} + \mathcal{H}_T, \tag{2.44}$$

where

$$V_{NR}(r) = V_V(r) + V_S(r), \tag{2.45}$$

$$\mathcal{H}_{L.S} = \frac{1}{2m^2r}L.S\left[3\frac{\partial V_V(r)}{\partial r} - \frac{\partial V_S(r)}{\partial r}\right], \tag{2.46}$$

$$\mathcal{H}_{S.S} = \frac{2}{3m^2}S_1.S_2\nabla^2 V_V(r), \tag{2.47}$$

and

$$\mathcal{H}_T = \frac{1}{12m^2}\mathcal{S}_{12}\left[\frac{1}{r}\frac{\partial}{\partial r}V_V(r) - \frac{\partial^2}{\partial r^2}V_V(r)\right]. \tag{2.48}$$

The Hamiltonian may be re-written as

$$\mathcal{H} = 2m + \frac{p^2}{2\mu} + V_{NR}(r) + \mathcal{H}_{SD}, \tag{2.49}$$

where the spin dependent Hamiltonian is

$$\mathcal{H}_{SD} = \frac{\langle L.S\rangle}{2m^2}[\mathcal{T}_1 + 2\mathcal{T}_2] + \frac{\langle S_1.S_2\rangle}{m^2}\mathcal{T}_3 + \frac{\langle S_{12}\rangle}{m^2}\mathcal{T}_4. \tag{2.50}$$

Here, assuming a Coulombic form for the vector coupled potential,

$$\begin{aligned}
\mathcal{T}_1 &= -\langle \tfrac{1}{r}\tfrac{dV_S}{dr}\rangle + \mathcal{T}_2, && \\
\mathcal{T}_2 &= \langle \tfrac{1}{r}\tfrac{\partial V_V}{\partial r}\rangle &&= \tfrac{4\alpha_s}{3}\langle r^{-3}\rangle, \\
\mathcal{T}_3 &= \langle \tfrac{2}{3}\nabla^2 V_V\rangle &&= \tfrac{32\pi\alpha_s}{9}\langle |\psi(0)|^2\rangle, \\
\mathcal{T}_4 &= \langle \tfrac{1}{12}\left[\tfrac{1}{r}\tfrac{\partial V_V}{\partial r} - \tfrac{\partial^2 V_V}{\partial r^2}\right]\rangle &&= \tfrac{\alpha_s}{3}\langle r^{-3}\rangle.
\end{aligned} \tag{2.51}$$

Since $\langle S_{12}\rangle$, $\langle S_1.S_2\rangle$ and $\langle L.S\rangle$ are diagonal in the L-S coupled angular momentum basis we can immediately write down the eigenstates, and evaluate the angular momentum factors in the Hamiltonian.

2.3.4 Angular Momentum Structure

We first couple the quark spins to form a spin-1 triplet and spin-0 singlet, which are then coupled to $L = 0, 1, 2, \ldots \equiv S, P, D, \ldots$, to form the states in Table 2.2

Table 2.2: LS coupled angular momentum states

	$L=0$			$L=1$		
		State	J^{PC}		State	J^{PC}
S=0	Pseudoscalar	$^1S_0$	0^{-+}	Singlet h state	$^1P_1$	1^{+-}
S=1	Vector	$^3S_1$	1^{--}	Triplet χ states	$^3P_0$	0^{++}
					$^3P_1$	1^{++}
					$^3P_2$	2^{++}

Here we have used the spectroscopic notation ^mL_J where $m = 2s + 1$ is the spin multiplicity, L is the orbital angular momentum and J is the total angular momentum. Since the quarks are degenerate in mass we have associated both definite parity and charge quantum numbers via the assignments

$$P = (-1)^{L+1} \qquad C = (-1)^{L+S}. \tag{2.52}$$

The expectation values of the angular momentum operators in the spin dependent Hamiltonian in this basis are given in Table 2.3:

Table 2.3: Spin factors for quarkonium Hamiltonian

State	J^{PC}	$\langle S_1 \cdot S_2 \rangle$	$\langle L.S \rangle$	$\langle S_{12} \rangle$
$^1S_0$	0^{-+}	$-\frac{3}{4}$	0	0
$^3S_1$	1^{--}	$\frac{1}{4}$	0	0
$^1P_1$	1^{+-}	$-\frac{3}{4}$	0	0
$^3P_0$	0^{++}	$\frac{1}{4}$	-2	-4
$^3P_1$	1^{++}	$\frac{1}{4}$	-1	-2
$^3P_2$	2^{++}	$\frac{1}{4}$	1	$-\frac{2}{5}$

This gives us the machinery to study the phenomenology of non-relativistic systems given an ansatz for the QCD potential, and turn our attention to some frequently used potential models.

2.4 Phenomenological Model Potentials

Phenomenological potentials [31, 29, 32] can be used to make estimates of various operators in the J/ψ,Υ, B_C and, occasionally and somewhat dubiously, heavy-light systems.

One of the most frequently used potential models for QCD is the Cornell potential

$$V(r) = -\frac{4}{3} \cdot \frac{\alpha_s}{r} + Kr, \tag{2.53}$$

where K is the string tension which is inferred from experiment to be 0.440GeV, and the coupling is set at a scale $Q^2 = M^2_{\text{meson}}$.

Other commonly used potentials are the Richardson potential

$$V(r) = -\frac{4}{3}\frac{48\pi^2}{33-2n_F}\frac{1}{(2\pi)^3}\int d^3k \frac{e^{ik\cdot r}}{k^2\log(1+\frac{k^2}{\Lambda^2})}, \tag{2.54}$$

and the Buchmuller potential

$$V(r) = -\frac{4}{3}\frac{1}{(2\pi)^2}\int d^3k e^{ik\cdot r}\frac{4\pi\alpha_s(k^2)}{k^2}. \tag{2.55}$$

As is shown in Appendix C, the solution of these potential models reduces to solving a one dimensional second order ODE for the spin-independent Hamiltonian, yielding both the radial wavefunctions and the spin independent mass spectrum. The spin-dependent Hamiltonian is treated as a perturbation about these solutions, requiring the expectation of various operators to be evaluated. It is worth noting that the Virial theorem shows that Υ is self consistent as a non-relativistic system, while J/ψ should suffer from significant relativistic corrections. Again see Appendix C for details.

2.5 Mass Dependence of Quarkonium Spectrum

2.5.1 Mass Dependence of Hyperfine Splitting

The hyperfine splitting may be found using the expectation of the spin-spin Hamiltonian assuming the 1-gluon exchange $V_V = -\frac{4}{3}\frac{\alpha_s}{r}$ potential, and that $\nabla^2\frac{1}{r} = -4\pi\delta^3(r)$,

$$\langle\mathcal{H}_{S.S}\rangle = \frac{\langle S_1\cdot S_2\rangle}{M^2}\frac{32\pi}{9}\alpha_s(M_Q)|\psi(0)|^2. \tag{2.56}$$

This gives the hyperfine splitting to be

$$\frac{\frac{1}{4}-\frac{(-3)}{4}}{M^2}\cdot\frac{32\pi}{9}\alpha_s(M_Q)|\psi(0)|^2 = \frac{32\pi}{9M^2}\alpha_s(M_Q)|\psi(0)|^2. \tag{2.57}$$

In the Cornell potential we have from Appendix C,

$$|\psi(0)|^2 = \frac{M}{4\pi}\langle\frac{4}{3}\frac{\alpha_s}{r^2} + K\rangle, \tag{2.58}$$

so that for sufficiently light quarks, when the linear potential dominates,

$$|\psi(0)|^2 = \frac{M}{4\pi} \cdot K \tag{2.59}$$

and then the hyperfine splitting is inversely proportional to M. A common alternative to this phrasing is that $\Delta M^2 = M^2_{\text{vector}} - M^2_{\text{pseudo}}$ is constant.

This law will break down for sufficently heavy quarks. Empirically, however, the law holds when comparing charm and beauty systems.

2.5.2 Hyperfine Splitting in the Quenched approximation

Since current lattice simulations are performed in the quenched approximation it becomes imperative to ask what effect this has on the observed spectrum. This has been discussed in [33, 34], and a summary of the arguments is presented here.

The arguments start with the observation that many phenomenological potentials employ the running coupling Equation (2.19)

$$\alpha_s(Q^2) = \frac{3}{33 - 2n_f}\frac{4\pi}{\log\frac{Q^2}{\Lambda^2}} \tag{2.60}$$

to take account of sea quark screening effects. In the quenched approximation of QCD, $n_F = 0$ so that the coupling's Q^2 dependence will be slower than the full theory. The potential in the quenched approximation cannot therefore simultaneously have the long distance and short distance potential correct.

In a lattice calculation the coupling is set by choosing the dimensionful lattice spacing to match some observable to the experimental QCD value. The choice of observable used as input is a question of statistical precision and relevance to the calculation. Typically a long distance quantity such as the string tension or the $\rho - \pi$ splitting is used. This choice causes the potential to be incorrect at short distances due to the incorrect screening effect of the running coupling. Additionally we expect the full theory to demonstrate string breaking effects at larger distances, while the quenched theory should maintain a linear potential indefinitely.

El-Khadra et al [33, 34] estimate the change in $|\psi(0)|^2$ due to the slower fall off of the Richardson potential, to obtain that $|\psi_{\text{Quenched}}(0)|^2$ is $\sim$ 30% less than the full theory, and hence the same discrepancy for the hyperfine splitting in the quenched approximation. This calculation is, however, model dependent.

It is often suggested that for heavy quark systems the lattice spacing should be set through a shorter distance quantity such as a quarkonium observable, so that the short distance potential is correct. This clearly has the disadvantage that the confining potential is then incorrect. The proponents, however, argue that it is more imperative to approximate well the short range physics for quarkonia.

The simulation of systems such as heavy-light mesons, where both large and small scales are involved, is clearly problematic and will be one of the most exciting areas to study beyond the quenched approximation.

2.5.3 Quarkonium Fine Structure

The fine structure can be estimated via

$$\langle 1P|\, \mathcal{H}_{L\cdot S} + \mathcal{H}_T \,|1P\rangle = \frac{\mathcal{L}\cdot\mathcal{S}}{2m^2}\left[3\langle\frac{V_V'(r)}{r}\rangle - \langle\frac{V_S'(r)}{r}\rangle\right] + \frac{\mathcal{S}_{12}}{12m^2}\left[\langle\frac{1}{r}V_V'(r) - V_V''(r)\rangle\right] \tag{2.61}$$

In the Cornell potential this becomes

$$\langle 1P|\, \mathcal{H}_{L\cdot S} + \mathcal{H}_T \,|1P\rangle = \frac{1}{2m^2}\left\{\left[4\mathcal{L}\cdot\mathcal{S} + \frac{2}{3}\mathcal{S}_{12}\right]\alpha_s\langle r^{-3}\rangle - \mathcal{L}\cdot\mathcal{S}K\langle r^{-1}\rangle\right\} \tag{2.62}$$

The expectations of this perturbation for the different P-states are [31] given in Table 2.4, where we have given the perturbation $2m^2\Delta E$ of the state in the Cornell potential. We define the ratio

Table 2.4: Quarkonium P-state spin perturbations

	State	$2m^2\Delta E$
h	$^1P_1$	0
χ_0	$^3P_0$	$-\frac{32}{3}\alpha_s\langle r^{-3}\rangle + 2K\langle r^{-1}\rangle$
χ_1	$^3P_1$	$-\frac{8}{3}\alpha_s\langle r^{-3}\rangle + K\langle r^{-1}\rangle$
χ_2	$^3P_2$	$-\frac{8\cdot 7}{3\cdot 5}\alpha_s\langle r^{-3}\rangle - K\langle r^{-1}\rangle$

$$\rho = \frac{\chi_2 - \chi_1}{\chi_1 - \chi_0} = \frac{1}{5}\cdot\frac{8\alpha_s\langle r^{-3}\rangle - \frac{5}{2}K\langle r^{-1}\rangle}{2\alpha_s\langle r^{-3}\rangle - \frac{1}{4}K\langle r^{-1}\rangle} \tag{2.63}$$

We can identify two clear extreme cases for ρ : if the Coulomb part of the potential dominates the fine structure, $\rho \leq \frac{4}{5}$, while if the linear part dominates $\rho \geq 2$.

Experimentally $\rho \sim 0.6$ and which suggests (but by no means guarantees) that the Coulombic part of the potential dominates the fine structure. If we now consider the absolute values of the fine splittings, then the dominant terms are $\propto \frac{1}{2m^2}\langle r^{-3}\rangle$.

Empirically the fine structure decreases from charm to beauty and is well approximated by $\frac{1}{M}$ scaling. This suggests that the wavefunction should shrink with mass such that $\langle r^{-3}\rangle \propto M$. This is indeed the case for the Coulomb potential, however the phenomenological potentials typically used must be solved numerically and there is no further useful intuition that can be gained analytically.

2.5.4 Spin Independent Splittings

Empirically the spin averaged S-P splitting and 2S-1S splittings are approximately the same in the J/ψ and Υ systems, as shown in Table 2.5. The numerical solutions of the phenomenological potentials do indeed show this behaviour, however there are no analytic solutions from which we can obtain this intuition.

Table 2.5: Experimental quarkonium spin independent splittings

System	S-P Splitting	$2S-1S$ Splitting
J/ψ	458 MeV	590 MeV
Υ	460 MeV	560 MeV

2.6 Heavy-Light meson systems

In order to understand the expected behaviour of heavy-light systems such as D and B mesons we must consider the heavy quark effective theory. I therefore present a derivation of HQET directly from the QCD Lagrangian. The derivation is heavily based on the Mannel paper [35].

2.7 Heavy Quark Effective Theory

Heavy Quark Effective Theory can be derived as an effective Lagrangian directly from the QCD functional integral. As is usual for an effective low energy theory (such as the four-Fermi interaction) the fields of a massive particle are integrated out and the resulting (non-local) action is expanded in terms of local operators. The series is then truncated at some order making the resulting theory approximate. In the following treatment all unnecessary indices will be suppressed.

$$Z(\eta,\bar{\eta},\lambda)=\int[dQ][d\bar{Q}][d\phi_\lambda]e^{iS_Q+iS_\lambda+i\int d^4x(\bar{\eta}Q+\bar{Q}\eta+\phi_\lambda\lambda)}, \tag{2.64}$$

where $\phi_\lambda = q, A^a_\mu$ denotes light quark and gluon degrees of freedom, $\phi_\lambda\lambda$ is a shorthand for the sources for the light degrees of freedom, and Q is the heavy quark field.

The action is

$$S_\lambda=-\frac{1}{4}F^a_{\mu\nu}F^{\mu\nu}_a+\sum_{u,d,s}\bar{q}(i\not{D}-m_q)q, \tag{2.65}$$

where

$$D_\mu=\partial_\mu+igA^a_\mu T^a \quad , \quad [D_\mu,D_\nu]=igF^a_{\mu\nu}T^a. \tag{2.66}$$

The heavy quark action is

$$S = \int d^4x \bar{Q}(i\not{D} - m_Q)Q. \tag{2.67}$$

We now wish to describe a hadron containing a valence heavy quark. We define the four velocity of the hadron $v_\mu = \frac{p_\mu}{M_{had}}$. We expect that the heavy quark will fluctuate around this by terms of $O(\frac{\Lambda_{QCD}}{M_Q})$. This velocity vector has $v^2 = 1$, and can be used to project the upper and lower components in the rest frame of the hadron:

$$\phi = \frac{1}{2}(1+\not{v})Q \quad , \quad \bar{\phi} = \frac{1}{2}\bar{Q}(1+\not{v}) \tag{2.68}$$

$$\chi = \frac{1}{2}(1-\not{v})Q \quad , \quad \bar{\chi} = \frac{1}{2}\bar{Q}(1-\not{v}). \tag{2.69}$$

We can use the velocity vector to define the longitudinal and transverse covariant derivatives as follows:

$$\not{D} = \not{v}(v.D) + \not{D}^\perp \tag{2.70}$$

$$\not{D}^\perp = \gamma^\mu(g_{\mu\nu} - v_\mu v_\nu)D^\nu \tag{2.71}$$

$$\{\not{D}^\perp, \not{v}\} = 0. \tag{2.72}$$

Writing $Q = \frac{1}{2}(1+\not{v})Q + \frac{1}{2}(1-\not{v})Q$ in the heavy quark action gives

$$S = \int d^4x \left[\bar{\phi}\{i(v.D) - m_Q\}\phi - \bar{\chi}\{i(v.D) + m_Q\}\chi + \bar{\phi}\; i\not{D}^\perp\chi + \bar{\chi}\; i\not{D}^\perp\phi\right]. \tag{2.73}$$

We now reparametrise the fields to fluctuate around the space-time dependence of the plane wave solution travelling at v,

$$\phi = e^{-im_Q(v.x)}h_v \ , \ \chi = e^{-im_Q(v.x)}H_v. \tag{2.74}$$

The action expressed in terms of the new fields is

$$S_v = \int d^4x \left[\bar{h}_v i(v.D)h_v - \bar{H}_v\{i(v.D) + 2m_Q\}H_v + \bar{h}_v i\not{D}^\perp H_v + \bar{H}_v i\not{D}^\perp h_v\right]. \tag{2.75}$$

In order to study the Green functions of the theory, we re-write the source terms of the original fields in terms of the transformed variables,

$$\int d^4x\bar{Q}\eta + \bar{\eta}Q = \int d^4x\bar{\rho}_v h_v + h_v\bar{\rho}_v + \bar{R}_v H_v + \bar{H}_v R_v, \tag{2.76}$$

where

$$\rho_v = \frac{1}{2}(1+\not{v})e^{im_Q(v.x)}\eta\ ,\ \bar{\rho}_v = \bar{\eta}e^{-im_Q(v.x)}\frac{1}{2}(1+\not{v}). \tag{2.77}$$

Since we restricted the theory to hadrons containing no anti-quarks of the heavy flavor, we need not consider any Green functions with external H legs. Thus the terms of the form $\bar{R}H$ in the generating functional may be dropped and we may perform the Gaussian integral over these fields by completing the square in the exponent. This leaves the following generating functional,

$$Z(\rho_v, \bar{\rho}_v, \lambda) = \int [dh_v][d\bar{h}_v][d\lambda]\det M e^{iS'_v + iS_\lambda} e^{i\int d^4x\left[\bar{\rho}_v h_v + \bar{h}_v\rho_v + \phi_\lambda\lambda\right]}, \tag{2.78}$$

where

$$M = i(v.D) + 2m_Q - i\epsilon, \tag{2.79}$$

$$S'_v = \int d^4x\left[\bar{h}_v i(v.D)h_v - \bar{h}_v \not{D}^\perp M^{-1}\not{D}^\perp h_v\right]. \tag{2.80}$$

The M^{-1} term in the new action convolves the particle fields with the (twice mass suppressed) anti-particle propagator giving the anticipated non-locality.

The determinant is gauge-invariant, and can easily be shown to be constant in the axial gauge $v.A = 0$, and hence can be dropped from the generating functional. We expand the anti-particle propagator as

$$(i(v.D)+2m_Q-i\epsilon)^{-1} = \frac{1}{2m_Q}\left[1 - \frac{i(v.D)-i\epsilon}{2m_Q} + \left(\frac{i(v.D)-i\epsilon}{2m_Q}\right)^2 - \ldots\right], \tag{2.81}$$

writing $\gamma_\mu\gamma_\nu = g_{\mu\nu} - i\sigma_{\mu\nu}$,

$$\not{D}^\perp\not{D}^\perp = D^\mu(g_{\mu\nu} - v_\mu v_\nu)D^\nu + \frac{g}{2}\sigma_{\mu\nu}F^{\mu\nu}, \tag{2.82}$$

and we obtain the heavy quark effective action to order $\frac{1}{m_Q}$

$$S'_v = \int d^4x \left[\bar{h}_v i(v.D) h_v + K_v + M_v + O(\frac{1}{m_Q^2}) \right], \tag{2.83}$$

where

$$K_v = \frac{1}{2m_Q} \bar{h}_v D^\mu (G_{\mu\nu} - v_\mu v_\nu) D^\nu h_v \tag{2.84}$$

and

$$M_v = \frac{g}{4m_Q} \bar{h}_v \sigma_{\mu\nu} F^{\mu\nu} h_v. \tag{2.85}$$

Several important conclusions may be drawn from the form of this lowest order Lagrangian. Firstly at this order there is no heavy quark mass dependence, so that there is a manifest heavy flavour symmetry in, for example, the kinematics of heavy-light mesons.

Additionally, as shall be dealt with in more detail later, the $\frac{1}{m_Q}$ dependence of the leading spin term results in a $\frac{1}{m_Q}$ dependence of spin splittings in heavy-light mesons.

It is interesting to note that the leading heavy quark spin dependent term, M_v, is essentially the clover term (both arise from the continuum identity $\not{D}^{\,2} = D^2 + \frac{g}{2}\sigma_{\mu\nu}F^{\mu\nu}$) so that it is to be expected that there will be large discretisation errors in heavy quark spin dependent terms in poorly improved actions.

2.8 Structure of Heavy-Light Meson Spectra

We can now obtain some intuition for the structure and spectrum of heavy-light mesons [36, 37, 38, 39, 40]. Using the approximate spin and flavour symmetries, we ignore the heavy quark and construct $J_{\text{light}} = L + S_q$ angular momentum states, which approximate the physical eigenstates. In practice, there will be some mixing between these states at $\mathcal{O}(\frac{1}{M_Q})$. We then couple the heavy quark spin, to form the total angular momentum $J = J_{\text{light}} + S_Q = J_{\text{light}} \pm \frac{1}{2}$, forming a doublet for each J_{light} state, split at $\mathcal{O}(\frac{1}{M_Q})$. This gives the low-lying states in Table 2.6, and Figure 2.3.

Table 2.6: JJ coupled angular momentum states

			Doublets		
J_{light}	L	$L \cdot S_{\text{light}}$	States		
$\frac{1}{2}$	0	0	0^-	1^-	
$\frac{1}{2}$	1	-1	0^+	$1^+_{\frac{1}{2}}$	
$\frac{3}{2}$	1	$\frac{1}{2}$		$1^+_{\frac{3}{2}}$	2^+

Figure 2.3: Structure of low-lying heavy-light spectrum

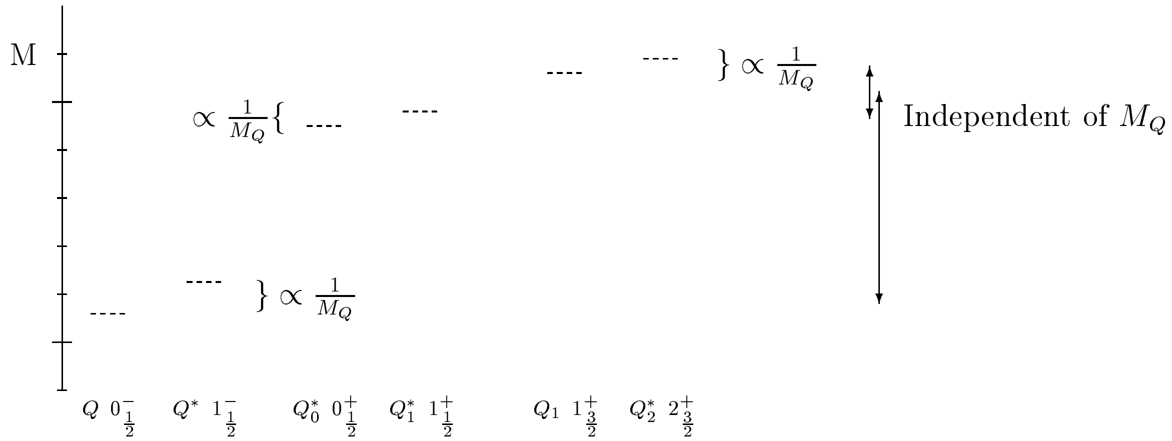

The splittings between the doublets are independent of the heavy quark mass, being purely a property of the light degrees of freedom, with $O(\frac{1}{M})$ corrections.

To date, only the $J_{\rm light} = \frac{3}{2}$ doublet has been observed in the D , D_s, B, and B_s systems (actually just an unresolved mixture [41] of the $1^+_{\frac{3}{2}}$ and the 2^+ for B and B_s). The association of the D_1 with $J_{\rm light} = \frac{3}{2}$ is made because of its narrow width [39, 42].

These states are charge conjugation indefinite, and the two 1^+ states have the same J^P. This causes difficulties in isolating the physical eigenstates when performing a lattice simulation. In order to better understand the mixing between these states it is necessary to consider Hamiltonian models.

2.9 $^3P_1 -^1 P_1$ mixing in non-degenerate mesons

Hamiltonian models have been applied [43, 44, 39, 45] to estimate the behaviour of heavy light and B_c systems. Based on HQET we know that in the degenerate limit the mass eigenstates are the $^3P_1 -^1 P_1$ basis, while in the $M_Q \to \infty$ limit the $J_{\rm light}$ basis forms the physical eigenstates. At intermediate mass differences, we expect that the mass eigenstates are some mixture of the two bases.

For non-degenerate mesons we proceed by writing down a Hamiltonian formulation for the heavy-light system. This is justified for B_C, but for the systems we are ultimately interested in this procedure cannot be exact, although Godfrey et al [43, 44] use a model which partially corrects for relativistic effects in heavy-light systems.

The Hamiltonian in the non-degenerate case is

$$\mathcal{H} = m_q + m_Q + \frac{p^2}{2\mu} + V_V(r) + V_S(r) + \mathcal{H}_{SD}, \tag{2.86}$$

where the spin-dependent Hamiltonian is given by

$$\begin{aligned} \mathcal{H}_{SD} &= \frac{\langle L\cdot S_q\rangle}{2m_q^2}\mathcal{T}_1 + \frac{\langle L\cdot S_Q\rangle}{2m_Q^2}\mathcal{T}_1 + \frac{\langle L\cdot S_q\rangle}{m_q m_Q}\mathcal{T}_2 \\ &+ \frac{\langle L\cdot S_Q\rangle}{m_q m_Q}\mathcal{T}_2 + \frac{\langle S_q\cdot S_Q\rangle}{m_q M_Q}\mathcal{T}_3 + \frac{\langle S_{qQ}\rangle}{m_q M_Q}\mathcal{T}_4. \end{aligned} \tag{2.87}$$

Here the $\mathcal{T}_i$ are the expectations in Equation (2.51). Three bases for the total angular momentum J can be formed depending on the order of the coupling of the angular momenta:

- $J = L + S$; $S = S_q + S_Q$; Definite $\langle S_q.S_Q\rangle$,$\langle L.S\rangle$
- $J = J_q + S_Q$; $J_q = L + S_q$; Definite $\langle S_q.L\rangle$,$\langle J_q.S_Q\rangle$
- $J = J_Q + S_q$; $J_Q = L + S_Q$; Definite $\langle S_Q.L\rangle$,$\langle J_Q.S_q\rangle$

Since the Hamiltonian involves terms in $L.S_q$, $L.S_Q$ and $S_q.S_Q$ the Hamiltonian is not diagonal in any of the above bases. To proceed we must pick one basis and evaluate the off-diagonal Hamiltonian matrix, diagonalising to obtain the eigenstates and eigenvalues. Since HQET implies that in the $m_Q \to \infty$ limit the J_q basis is the physical basis, we evaluate the matrix elements of $\langle S_q \cdot S_Q\rangle$ and $\langle L\cdot S_Q\rangle$ in the J_q basis. To do so we must know the basis transformation matrices between each of the bases.

The general problem of relating the bases for three coupled angular momenta $J = j_1 \oplus j_2 \oplus j_3$ is most conveniently solved using $6j$ symbols. Suppose we couple either $j_{12} = j_1 \oplus j_2$ or $j_{23} = j_2 \oplus j_3$ first. Then the matrix

$$\langle j_{12}|j_{23}\rangle = (-1)^{j_1+j_2+j_3+J}\sqrt{2j_1+1}\sqrt{2j_3+1}\left\{\begin{array}{ccc} j_1 & j_2 & j_{12} \\ j_3 & J & j_{23} \end{array}\right\}, \tag{2.88}$$

where the general form and tables of the $6j$ symbol $\left\{\begin{array}{ccc} j_1 & j_2 & j_{12} \\ j_3 & J & j_{23} \end{array}\right\}$ can be found in Landau and Lifschitz [30] and Edmonds [46]. Evaluating these matrix elements $\langle j_{12}|j_{23}\rangle$ enables us to transform between each of the bases, and, in particular, transform the parts of the Hamiltonian that are diagonal in the $L-S$ and J_Q bases to the J_q basis.

The transformation matrices obtained are as follows:

$$M_{qQ} = \begin{bmatrix} \langle J_q = \frac{1}{2} | J_Q = \frac{1}{2} \rangle & \langle J_q = \frac{1}{2} | J_Q = \frac{3}{2} \rangle \\ \langle J_q = \frac{3}{2} | J_Q = \frac{1}{2} \rangle & \langle J_q = \frac{3}{2} | J_Q = \frac{3}{2} \rangle \end{bmatrix} = \begin{bmatrix} \frac{1}{3} & -\frac{\sqrt{8}}{3} \\ \frac{\sqrt{8}}{3} & \frac{1}{3} \end{bmatrix} \quad (2.89)$$

$$M_{qS} = \begin{bmatrix} \langle J_q = \frac{1}{2} | S = 0 \rangle & \langle J_q = \frac{3}{2} | S = 0 \rangle \\ \langle J_q = \frac{1}{2} | S = 1 \rangle & \langle J_q = \frac{3}{2} | S = 1 \rangle \end{bmatrix} = \begin{bmatrix} \frac{1}{\sqrt{3}} & \frac{\sqrt{2}}{\sqrt{3}} \\ \frac{\sqrt{2}}{\sqrt{3}} & -\frac{1}{\sqrt{3}} \end{bmatrix}. \quad (2.90)$$

We now write the spin dependent Hamiltonian as a sum of three pieces, each diagonal in a different basis:

$$\mathcal{H}_{SD} = \mathcal{H}_{J_q} + M_{qQ}\mathcal{H}_{J_Q}M_{qQ}^{\dagger} + M_{qS}\mathcal{H}_{L\cdot S}M_{qS}^{\dagger}, \quad (2.91)$$

where in the J_q basis:

$$\mathcal{H}_{J_q} = \begin{bmatrix} -1 & 0 \\ 0 & \frac{1}{2} \end{bmatrix} \left(\frac{\mathcal{T}_1}{2m_q^2} + \frac{\mathcal{T}_2}{m_q m_Q} \right) \quad (2.92)$$

$$M_{qQ}\mathcal{H}_{J_Q}M_{qQ}^{\dagger} = \begin{bmatrix} \frac{1}{3} & -\frac{\sqrt{2}}{3} \\ -\frac{\sqrt{2}}{3} & -\frac{5}{6} \end{bmatrix} \left(\frac{\mathcal{T}_1}{2m_Q^2} + \frac{\mathcal{T}_2}{m_q m_Q} \right) \quad (2.93)$$

$$M_{qS}\mathcal{H}_{L\cdot S}M_{qS}^{\dagger} = \begin{bmatrix} \frac{4}{3} & \frac{2\sqrt{2}}{3} \\ \frac{2\sqrt{2}}{3} & \frac{2}{3} \end{bmatrix} \frac{\mathcal{T}_4}{m_q m_Q}. \quad (2.94)$$

As in the potential model calculations for quarkonia, the quantities $\mathcal{T}_1, \ldots, \mathcal{T}_4$ can be found by solving the one dimensional spin-independent reduced Schroedinger equation, and the spin dependent Hamiltonian treated as a perturbation. The solution for the spin-dependent eigenstates and energy eigenvalues then reduces to simply diagonalising the 2×2 matrix $\mathcal{H}_{SD}$.

This approach has allowed various potential model calculations [38, 39, 44] to make predictions for the splittings and mixing angles of the 1^+ P-states for B_c and heavy-light systems.

2.10 Simulation of Heavy Quarks

In this chapter we have considered QCD based arguments for the m_Q dependence of the spectrum of quarkonia and heavy light mesons. This allows an appropriate parametrisation of fits to simulation data enabling extrapolations in the quark mass to be performed to the physical values. Additionally, an intuitive understanding of the dependence is essential in the evaluation of the quality of a lattice simulation: for example previous simulations with the Wilson and Clover actions on current lattices have had the extrapolated hyperfine splittings vanish at finite quark mass signifying discretisation errors.

The Virial theorem results for the average kinetic energy also play a role in our choice of the simulated action:

2.10.1 Relativistic or not...

As mentioned in chapter 1 the Wilson action suffers from severe discretisation effects when the $ma \geq O(1)$, while the inverse lattice spacing is limited to below about 2.7GeV in current simulations putting an upper limit on the mass range that can be accurately simulated.

There are essentially two approaches to the simulation of heavy quarks above this range, these are:

- Simulate in the regime where the action is accurate, and use HQET to fit the leading quark mass dependence to the simulation data, allowing extrapolation to heavier masses.
- Truncate the HQET expansion of the full action, and simulate directly at the desired heavy quark mass with this approximate NRQCD action.

The breakdown of the non-relativistic approximation for charm quarks leaves the Wilson approach as the most systematically controllable technique for simulating charm. Discretisation errors will of course be large, however a continuum extrapolation will allow conclusions to be drawn about the continuum limit. At the beauty mass however, the relativistic corrections to the NRQCD action are thought to be under control in the currently used actions and, as such, NRQCD is the most accurate technique for obtaining results at the beauty mass.

The remainder of this thesis presents the results obtained when simulating the systems described in this chapter with heavy quark masses around that of the charm ~ 1.5GeV, using the heavy Wilson quark approach, and the techniques described in chapter 1.

Chapter 3

Quenched Heavy Meson Spectrum at $\beta = 6.0$

This chapter presents the results obtained from a simulation of the meson spectrum at $\beta = 6.0$ using the tadpole improved Wilson action. Before presenting the details and analysis of this simulation, it is worth making a brief discussion of the analysis of lattice data, and of quenched data in particular.

3.1 Analysing Quenched Data

3.1.1 Interpreting the theory with massless quarks

In order to interpret quenched data and answer the question "what is the quenched prediction for the hadron spectrum" we must consider carefully which quenched theory we refer to. Firstly, consider the theory with only massless quarks. In this case all dimensionful quantities are proportional to some power of one dynamically generated dimensionful parameter, Λ_{QCD}.

$$\mathcal{O}_i = c_i \times (\Lambda_{\mathrm{QCD}})^{n_i} \tag{3.1}$$

where c_i are dimensionless constants of the theory.

In the lattice theory the observables are dimensionless with the appropriate power of a cancelling the dimension of the physical observable, so that dimensionless ratios of observables are the predictions of the theory. We define the continuum limit of ratios of observables i and j having the same mass dimension

$$R_{ij}^{\mathrm{quench}} = \frac{c_i}{c_j} = \lim_{g_0 \to 0} R_{ij}(g_0) = \lim_{g_0 \to 0} \frac{\mathcal{O}_i(g_0)}{\mathcal{O}_j(g_0)} \tag{3.2}$$

We do not expect these quenched ratios, R_{ij}^{quench} , to be the same as in the full theory, R_{ij}^{full}, and, in certain cases, do not expect the quenched observables to be well defined.

We can answer the question "what is the quenched universe in which the quantity $\mathcal{O}_r$ is exactly as in the real world" by choosing one particular reference observable $\mathcal{O}_r^{\text{latt}}$, and comparing all other observables of the quenched theory to the full theory by looking at the ratios R_{ir}. We can make dimensionful predictions for $\mathcal{O}_i$ in this particular quenched theory by, for simplicity, assuming the operator has dimension L^{-1},

$$O_i^{\text{phys}} = R_{ir}^{\text{quench}} \mathcal{O}_r^{\text{expt}} \tag{3.3}$$

$$= a_r^{-1} \times \mathcal{O}_i^{\text{latt}} \tag{3.4}$$

where

$$a_r^{-1} = \frac{\mathcal{O}_r^{\text{expt}}}{\mathcal{O}_r^{\text{latt}}} \tag{3.5}$$

We expect that the quenched ratios differ from the full theory, and that the inverse lattice spacings obtained from different reference observables are related by

$$a_i^{-1} = R_{ij}^{\text{full}} / R_{ij}^{\text{quench}} \times a_j^{-1}. \tag{3.6}$$

The predictions of observables in the quenched approximation therefore depend on the quantity used to set the scale. If the reference quantity is chosen such that $R_{ir}^{\text{quench}} \simeq R_{ir}^{\text{full}}$, then the quenched prediction for $\mathcal{O}_i^{\text{phys}}$ is immediately rather good, leading to the argument made by those who wish to produce useful phenomenological predictions from the lattice that a quantity determined by a similar physical process to the observables under study should be used to set the scale. This constitutes deliberately taking the best case scenario for phenomenology and has a significant role to play when predicting experimentally undetermined quantities, however care should be taken when commenting on, for example, the remarkable success of the quenched approximation in predicting known quantities such as the spectrum.

If one wishes to rigorously study the deficiencies or otherwise of the quenched approximation, one should calculate all observables using one or more definitions of the lattice spacing, but using each definition consistently across the range of observables in order to see quenching effects more clearly.

3.1.2 Interpreting Lattice results with non-zero quark masses

With non-zero quark masses present, the question of what is meant by the quenched prediction is somewhat ambiguous since theory is now a function of these quark masses. We proceed on the assumption that the quenched approximation is good, and fix the lattice spacing and quark mass parameters using the observables of the theory that depend on these parameters. Again, we find that disagreements between the quenched theory and the real world produce ambiguities in both the lattice spacing and the quark masses, as well as incorrect phenomenological predictions.

It is natural to use some dynamically generated reference observable $\mathcal{O}_r$ such as the string tension or m_ρ to set the lattice spacing, since intuitively this is analogous to matching the renormalised lattice coupling to the physical coupling at some scale. We then set the quark masses in the theory (typically by post simulation extrapolation) by defining the bare mass parameter $a_r m_{0,r}^{\text{latt}}(g_0)$ such that some observable $\mathcal{O}_i$, typically the pseudoscalar mass, matches its physical value using some definition of the lattice spacing, i.e.

$$R_{ir}^{\text{quench}}(g_0, a_r(g_0) m_{0,r}^{\text{latt}}(g_0)) = R_{ir}^{\text{phys}} \tag{3.7}$$

We then take the continuum limit for all other observables, running the bare lattice quark mass to keep the ratio R_{ir}^{quench} fixed at the physical value:

$$R_{jr} = \lim_{g_0 \to 0} R_{jr}^{\text{quench}}(g_0, a_r(g_0) m_{0,r}^{\text{latt}}(g_0)). \tag{3.8}$$

Clearly, the lattice spacing used not only affects the conversion of lattice observables $\mathcal{O}_j$ to physical values, but also the way in which the quark mass is tuned. This can cause both enhanced and reduced uncertainties on observables due to lattice spacing ambiguities, depending on the quark mass dependence of $\mathcal{O}_j$.

The final comment of this section is that in practice simulations mix up both quenching and discretisation effects; the $g_0 \to 0$ extrapolation is in general difficult to perform unambiguously.

For sufficiently fine lattices, all well defined quenched quantities should scale; predictions formed using different definitions of the lattice spacing, each of which scale, will differ, indicating quenching effects which have been resolved from the discretisation effects.

3.2 Simulation Details - $\beta = 6.0$ calculation

The simulation was performed using 499 sample gauge configurations from a quenched distribution at $\beta = 6.0$ on a $16^3 \times 48$ lattice, using UKQCD time on the Cray T3D in the EPCC at Edinburgh University.

Table 3.1: $\beta = 6.0$ light quark kappas

κ	aM_{PS}	Fuzzing Radius
0.13856	0.228(2)	6
0.13810	0.293(1)	6
0.13700	0.4135(10)	6

Table 3.2: $\beta = 6.0$ heavy quark kappas

κ	$aM_{PS}(Q\bar{Q})$	Fuzzing Radius	MR Iterations
0.13000	0.9283(7)	3	95
0.12600	1.1618(6)	3	75
0.12200	1.3755(6)	3	65
0.11800	1.5751(6)	3	60
0.11400	1.7644(6)	3	55

In this simulation three light quark masses and five heavy quark masses were used, as given in Table 3.1 and Table 3.2

The light quark propagators were generated using a mixture of the MR, BiCG(γ_5) and BiCGSTAB algorithms [47], with convergence to a residue of $r = 10^{-7}$, to invert the tadpole improved Clover action with $C_{SW} = 1.47852$, corresponding to $U_0 = 0.8778$.

In order to define the meaning of the *adequate convergence* of a numerical inversion, we must consider the final observables - the correlation functions - and require that the statistical error in the ensemble averaged correlation functions is several orders of magnitude larger than the convergence error in the quark propagator. For heavy quark propagators the convergence criterion $r = 10^{-7}$ where

$$|r|^2 = \frac{\sum\limits_{x \in L^3 \times T} |\sum_{x'} M(x;x')\psi(x') - \eta(x)|^2}{\sum_x |\eta(x)|^2} \tag{3.9}$$

is a poor metric because the magnitude of the propagator varies greatly - the ratio is of order $\cosh 24aM = 10^{10}$, so that it is conceivable that the convergence criterion will be met purely by "getting the early timeslices right", irrespective of the errors near the middle of the lattice.

A more appropriate quantity than the residue for measuring the convergence of heavy propagators can be formed by defining the *timesliced residue*

$$|r_t|^2 = \frac{\sum\limits_{x \in L^3} |\sum_{x',t'} M(x,t;x',t')\psi(x',t') - \eta(x,t)|^2}{\sum\limits_{x \in L^3} |\psi(x,t)|^2} \tag{3.10}$$

Here the normalisation of the metric reflects the exponential fall off of the pseudoscalar correlator.

The central timeslices are precisely the asymptotic region we are interested in and so it is necessary to check the convergence here. Heavy-light meson correlators were generated on two configurations at $\beta = 6.2$ in 64 bit arithmetic using the different numbers of iterations $n_{\rm iter} \in \{50, 60, 65, 75, 100, 120, 130, 160, 200, 300\}$ for $\kappa_h = \{0.11900, 0.13200\}$, with the $n_{\rm iter} = 300$ correlators taken as a reference for accurate convergence .

Assuming $\frac{1}{\sqrt{N}}$ scaling of the statistical error from previous calculations on smaller data sets gives that the statistical fluctuations are much larger than 1 part in 10^4 on the average of all components. This level of error was used to define "adequacy", and comparison of the correlators with $n_{\text{iter}} = 300$ gave that adequate convergence occurred with 55 iterations for the $\kappa = 0.11900$ and within 120 iterations for the $\kappa = 0.13200$ propagators. This corresponded to a timesliced residue on timeslice 24 (the noisiest under this metric) of $r_{t=24} = O(10^{-11})$, which was used to define the convergence of all other heavy kappas.

Both local and fuzzed sources were used, which in combination with sink fuzzing allowed a 2×2 smearing matrix

$$\langle \mathcal{O}_i \mathcal{O}_j \rangle = \begin{pmatrix} \langle \mathcal{O}_L(x)\mathcal{O}_L(0)\rangle & \langle \mathcal{O}_F(x)\mathcal{O}_L(0)\rangle \\ \langle \mathcal{O}_L(x)\mathcal{O}_F(0)\rangle & \langle \mathcal{O}_F(x)\mathcal{O}_F(0)\rangle \end{pmatrix} \tag{3.11}$$

to be constructed. The full smearing matrices of mesons composed of the pairs of κ's given in Table 3.3 were correlated, where the heavier quark, κ_2, was smeared in the non-degenerate mesons.

Table 3.3: $\beta = 6.0$ meson combinations

		κ_2							
		3856	3810	3700	3000	$\kappa_{\text{charm}} = 2600$	2200	1800	1400
	3856	$q\bar{q}$	$q\bar{q}$	$q\bar{q}$	$Q\bar{q}$	$Q\bar{q}$	$Q\bar{q}$	$Q\bar{q}$	$Q\bar{q}$
	3810		$q\bar{q}$	$q\bar{q}$	$Q\bar{q}$	$Q\bar{q}$	$Q\bar{q}$	$Q\bar{q}$	$Q\bar{q}$
	3700			$q\bar{q}$	$Q\bar{q}$	$Q\bar{q}$	$Q\bar{q}$	$Q\bar{q}$	$Q\bar{q}$
κ_1	3000				$Q\bar{Q}$				
	2600					$Q\bar{Q}, Q\bar{c}$	$Q\bar{c}$	$Q\bar{c}$	$Q\bar{c}$
	2200						$Q\bar{Q}$		
	1800							$Q\bar{Q}$	
	1400								$Q\bar{Q}$

For the quark mass lying closest to the charm mass, $\kappa = 0.12600$, additional non-degenerate quarkonia correlators were generated, of interest for B_c. Three additional propagators, from derivative sources $\Delta_x, \Delta_y, \Delta_z$, were generated at this kappa allowing the differential operators in Table 1.4 to be constructed for the combinations given in Table 3.4. The most important result of this is that we now have access to the angular momentum 2 P-state.

Table 3.4: $\beta = 6.0$ differential operator combinations

		κ_2							
		3856	3810	3700	3000	$\kappa_{\text{charm}} = 2600$	2200	1800	1400
κ_1	3856					$Q\bar{q}$			
	3810					$Q\bar{q}$			
	3700					$Q\bar{q}$			
	3000								
	2600				$Q\bar{c}$	$Q\bar{Q}, Q\bar{c}$	$Q\bar{c}$	$Q\bar{c}$	$Q\bar{c}$
	2200								
	1800								
	1400								

3.3 Mass Fitting of Correlators

In what follows, all fits to correlators were made using correlated fits with the Marquardt Levenberg algorithm [48], and the bootstrap algorithm [17] was used to estimate the errors, using 1000 boot samples. Single exponential, row fit (Equation (1.95)) and matrix fit (Equation (1.96)) models were used and the fit ranges were varied, with $t_{\max}$ holding typically three values selected by inspection of the effective mass plots, and $t_{\min}$ varied over the entire range in which the Marquardt algorithm converged for the fit model. This procedure was carried out for each operator $\mathcal{O} \in \{0^{-+}, 1^{--}, 0^{++}, 1^{++}, 1^{+-}\}$ and where the data existed for the 2^{++} operator.

There were a total of 29 mass combinations, with 5 channels and three fit models. The volume of effective mass plots, tables of fitted masses, Q and χ^2/dof values prohibits the inclusion of this information in the thesis. The information was used to select a fitting range satisfying the following criteria:

- Stable in the fitted ground state when varying t_{min} by 1

- Stable in the bootstrapped statistical error on the ground state
- Acceptable $Q \geq \mathcal{O}(0.1)$ and $\chi^2/\mathrm{dof} \leq \mathcal{O}(1.5)$
- Consistency between single exponential and multi exponential fits

In practice it is not always possible to satisfy all criteria, for example the light-light vector fits, and in these circumstances an admittedly subjective compromise was taken to minimally break these conditions. For each meson state it was found that the one fitting range could be used for all kappa combinations in the same sector, obtaining the fit ranges in Table 3.5.

Table 3.5: $\beta = 6.0$ fitted timeslice ranges

Sector	Pseudoscalar	Vector	P-states
Light-Light	6-22 (FL,LL)	7-22 (FL,LL)	
Heavy-Light	8-21 (FL,LL)	8-21 (FL,LL)	7-13 (FF Single Exponential)
Heavy-Heavy	8-20 (FL,LL)	8-20 (FL,LL)	6-18 (FL,LL)

A feeling of the quality of data shall be conveyed by presenting one plot for each channel from each of the $q\bar{q}$, $Q\bar{q}$, and $Q\bar{Q}$ sectors using the optimal fit range.

The effective mass plots obtained with the selected fit range for systems involving the intermediate light quark mass $\kappa_q = 0.13810$ and the heavy quark nearest to charm, $\kappa_{\mathrm{Q}} = 0.12600$, for a row fit to the local - local and fuzzed - local [1] correlator are displayed in Figure 3.1 to Figure 3.7.

Inspection of the effective mass plots gives a few initial impressions of the data, which, as we shall see, are borne out by extrapolations.

Firstly the fuzzed-local correlators have double approaches to plateaux, suggesting similar strength of contamination by more than one excited state, but with opposite sign. This implies that the two exponential ansatz is not applicable on

[1] Convention is fuzzed - local $\Rightarrow$ source fuzzed, local sink.

Figure 3.1: Light-light pseudoscalar and vector effective masses

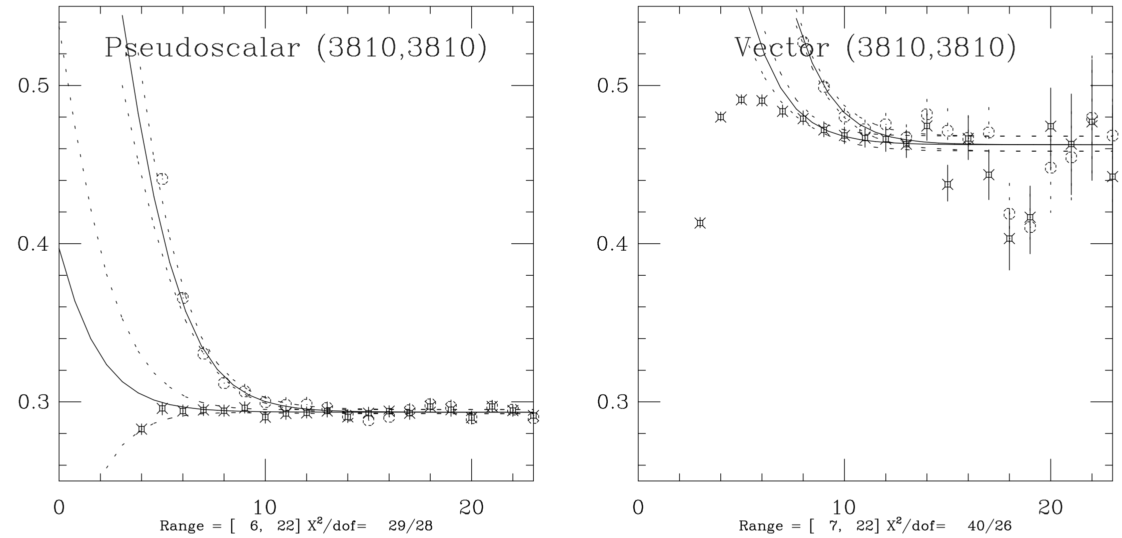

Figure 3.2: Heavy-light pseudoscalar and vector effective masses

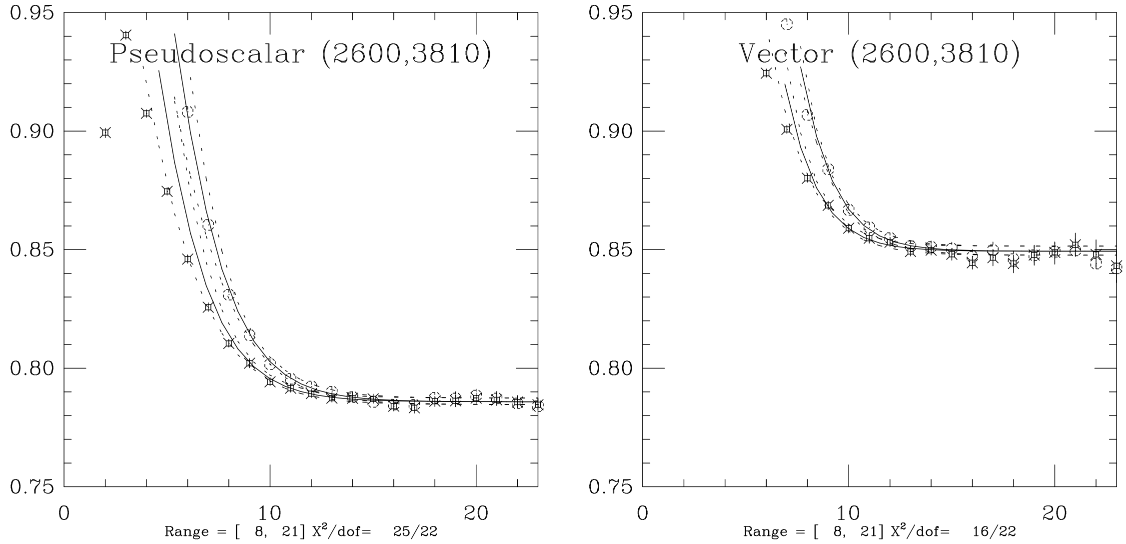

Figure 3.3: Heavy-heavy pseudoscalar and vector effective masses

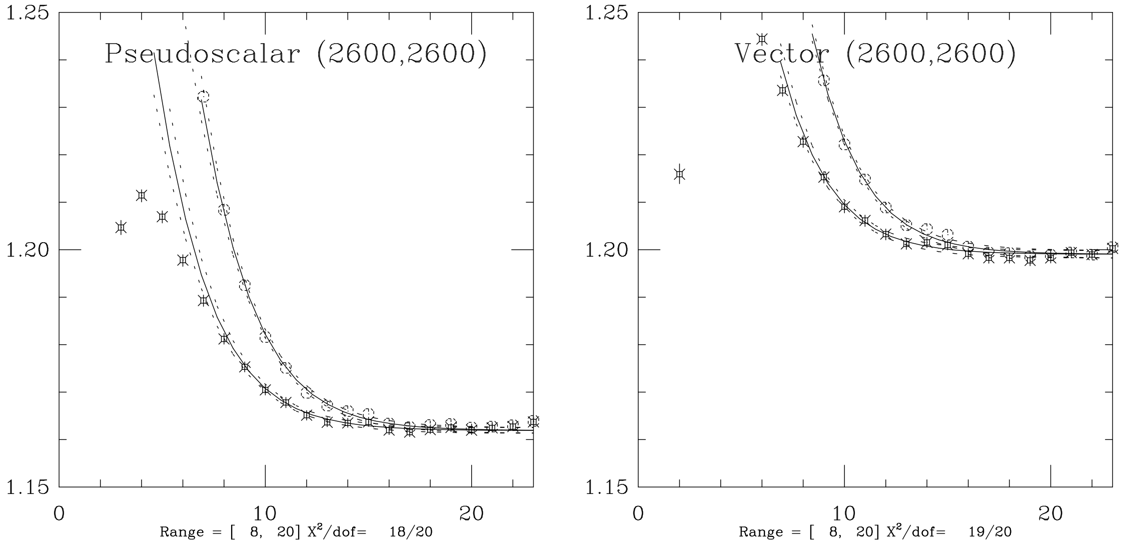

Figure 3.4: Heavy-light 0^{+},1^{+},2^{+} P state effective masses

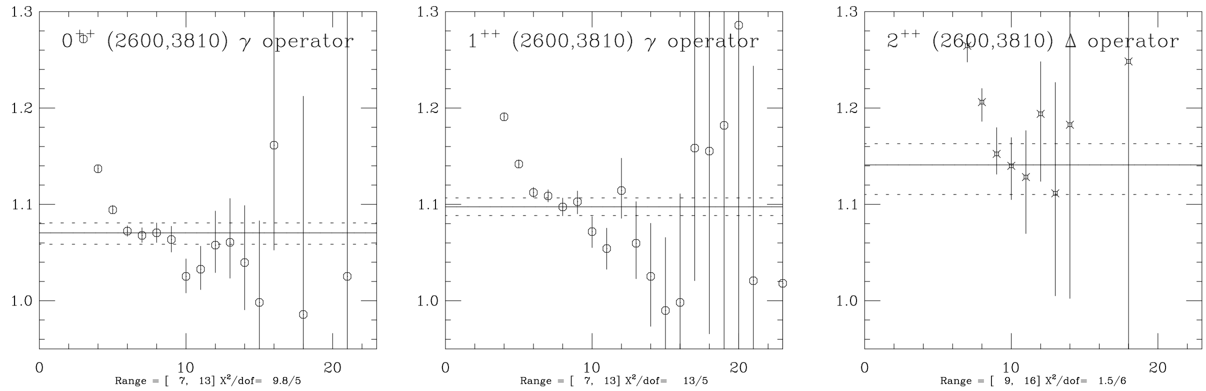

Figure 3.5: Consistency of single and triple-exponential fits to heavy-light P-states

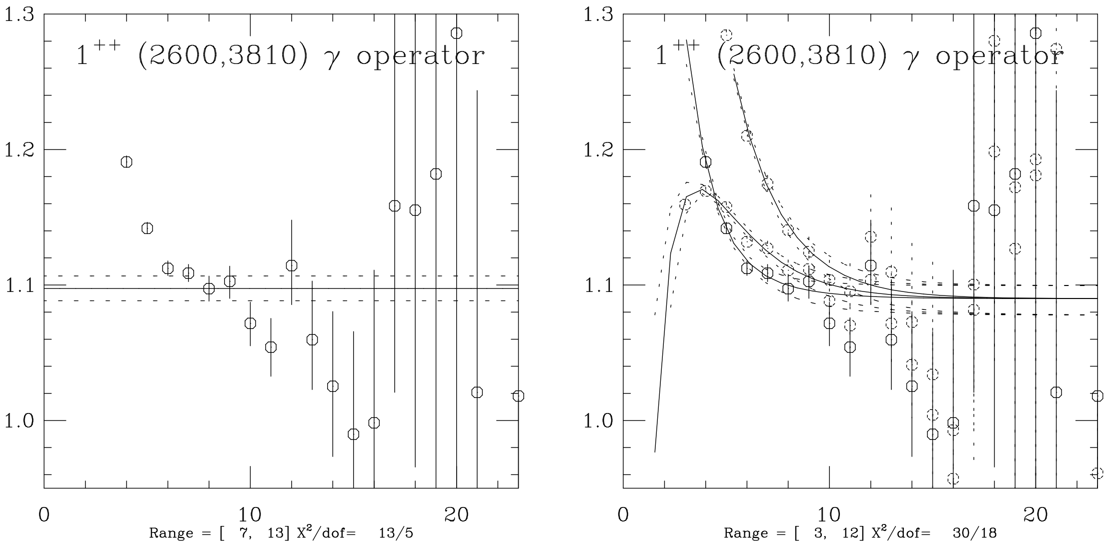

Figure 3.6: Quarkonium χ_0,χ_1, and h states using γ operators

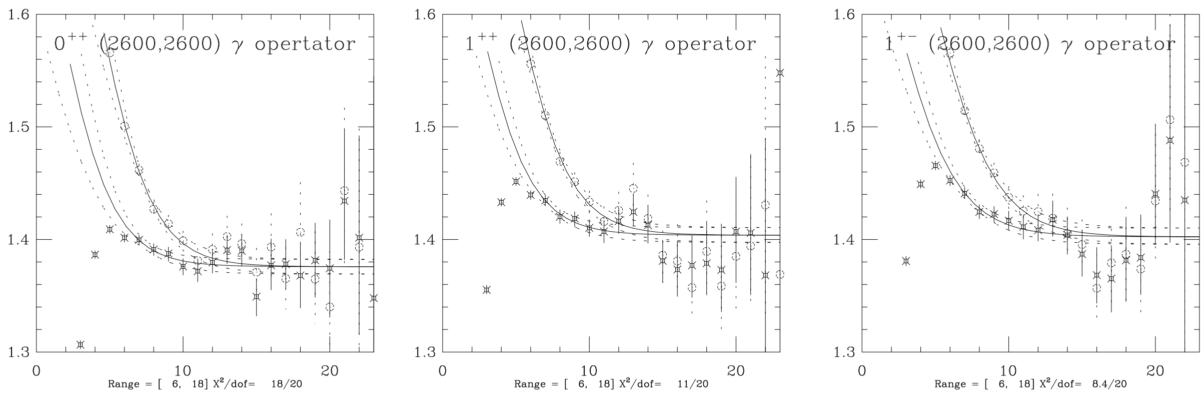

Figure 3.7: Quarkonium χ_0,χ_1, and χ_2 states using differential operators

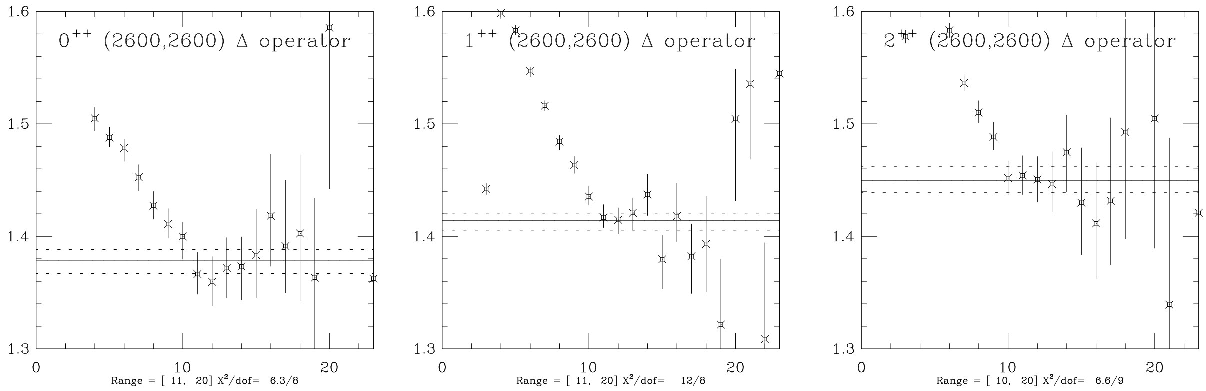

timeslices below the point of inflection of the final approach to the plateau, so that care must be taken when selecting $t_{\min}$ in the final fit.

Secondly, since the P-states have a large splitting from the pseudoscalar, the noise grows rapidly with time, and it is essential to perform part of the fit at short timeslices to obtain a good signal. For the heavy-light systems the fuzzed-fuzzed correlator formed the most convincing plateau and was used for single exponential fits; due to the rapid decay into noise these plateaux are not very long, however the consistency with double and triple exponential fits, Figure 3.5, gives us confidence in the selection of the range for the fitted plateau. Clearly the signal for the fine structure would benefit enormously from improved smearing techniques, which would give access to plateaux at earlier times. Figure 3.7 clearly shows the complete fine structure of the χ states in charmonium. We do not resolve the χ_1 from the h. The signal for the fine structure of the heavy-light P-states is poorer; the D_1 and D_0^* are resolved while the D_2^* is too noisy to expect to resolve the fine structure. The existence of even a marginal signal for fine structure is a big improvement over previous calculations and gives us confidence in our ability to estimate the $S - P$ splittings.

As an example of the selection of the optimal fit range, I present the sliding window fits for the (3810,3810) pseudoscalar single exponential fits, Table 3.6, and double exponential fits, Table 3.7. The fit method selected was the range 6-22 with a double exponential fit.

Table 3.6: Single exponential sliding window fit

tmin	tmax	χ^2/dof	χ^2	Q	Pseudo (3810,3810)
8	22	0.63	8.1	0.83	0.294(1)
9	22	0.56	6.7	0.88	0.293(1)
10	22	0.55	6.0	0.87	0.294(1)
11	22	0.60	6.0	0.81	0.294(1)
12	22	0.65	5.8	0.76	0.294(1)
13	22	0.67	5.3	0.72	0.293(2)
14	22	0.71	5.0	0.66	0.294(2)

Table 3.7: Double exponential sliding window fit

tmin	tmax	χ^2/dof	χ^2	Q	Pseudo (3810,3810)	Pseudo$'$ (3810,3810)
3	22	2.6	89.	8.4e-07	0.294(1)	1.27(1)
4	22	1.4	45.	0.069	0.294(1)	1.11(3)
5	22	1.0	31.	0.42	0.294(1)	0.99(4)
6	22	1.0	29.	0.41	0.293(1)	0.91(7)
7	22	1.0	26.	0.47	0.293(1)	0.77(8)
8	22	1.1	25.	0.39	0.293(1)	0.75(10)

The optimally fitted lattice masses to each of the channels and mass combinations used are presented in the Tables D.11 - D.23.

3.4 Kinetic Masses

As was discussed in Section 1.14.2, we use the dispersion relation Equation (1.105) to define the kinetic quark mass

$$(2m_2)^{-1} = \frac{\partial E}{\partial(p^2)}|_{\vec{p}=0}. \tag{3.12}$$

The correlation functions were computed at momenta

$$a\vec{p} = \frac{2\pi}{16}\vec{n}, \tag{3.13}$$

where the values of the vector $\vec{n}$ are those in Table 3.8, and the factor of $\frac{1}{16}$ comes naturally from the number of sites in the lattice. This allows us to compute the dispersive mass by fitting the dispersion relation

$$E(p^2) = m_1 + \frac{p^2}{2m_2} + Cp^4. \tag{3.14}$$

Table 3.8: $\beta = 6.0$ momenta

Momentum Directions		
	(0,0,0)	
(1,0,0)	(0,1,0)	(0,0,1)
(1,1,0)	(1,0,1)	(0,1,1)
	(1,1,1)	
(2,0,0)	(0,2,0)	(0,0,2)

It was found that the statistical noise at non-zero momentum was such that a single exponential fit was adequate. The non-zero momentum behaviour of the $(2600, 2600)$ pseudoscalar , Figure 3.8, Figure 3.9, and Figure 3.10 is considered typical, and the fitted lattice masses are given in Table D.18 and Table D.24.

Making the assumption that the kinetic mass shift for a meson on the lattice comes at leading order from the kinetic mass shifts of the free propagator of the constituent heavy quarks, we produce the following relations for heavy-heavy and heavy-light systems respectively.

$$M_2(ps) = 2M_{2,\text{pert}}(M_1/2). \tag{3.15}$$

$$M_2(ps) = M_{2,\text{pert}}(M_1). \tag{3.16}$$

Here $M_{2,\text{pert}}$ is the free Wilson Fermion expression Equation (1.107). The over-

Figure 3.8: Pseudoscalar (2600, 2600) at non-zero momentum

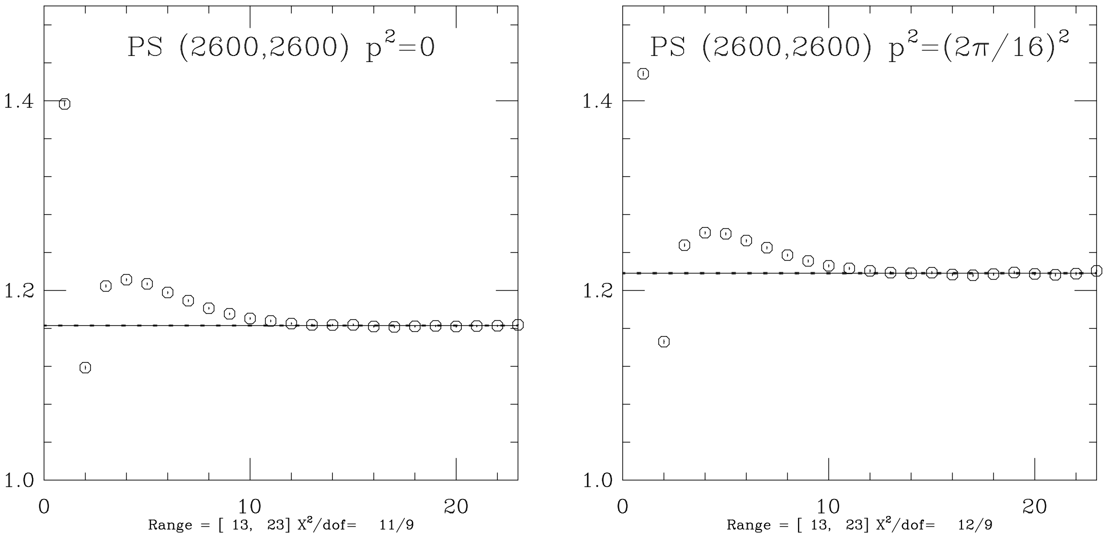

Figure 3.9: Pseudoscalar (2600, 2600) at non-zero momentum

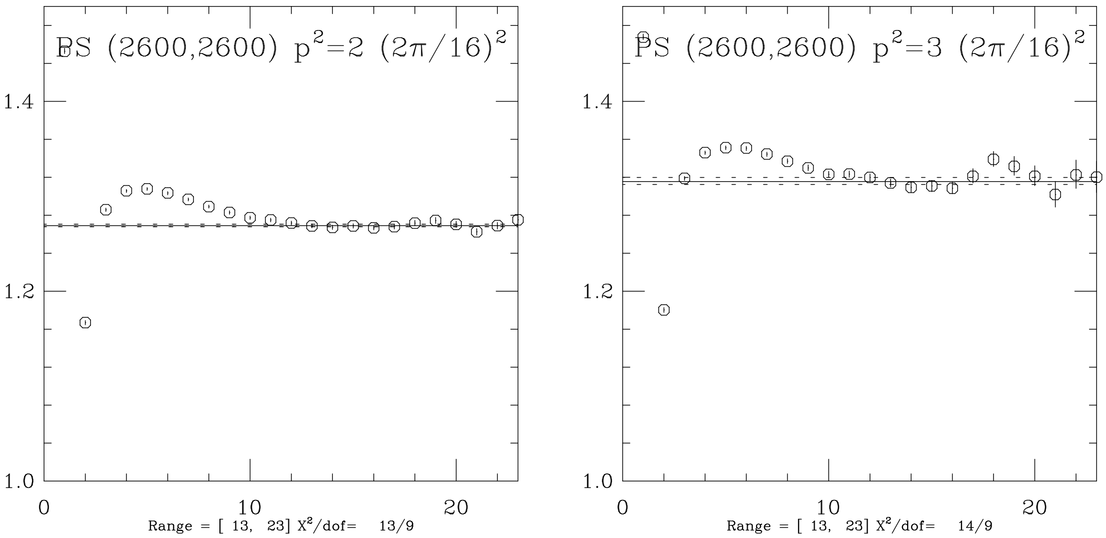

Figure 3.10: Pseudoscalar $(2600, 2600)$ at non-zero momentum

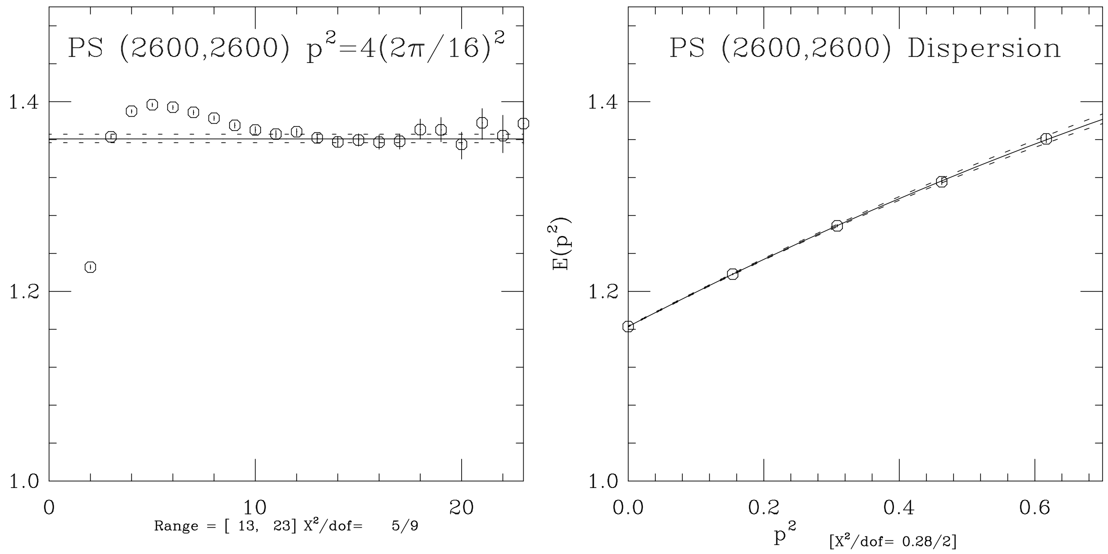

layed curve in Figure 3.11 is the perturbative shift for heavy-heavy systems so that we find, surprisingly, that the kinetic mass - pole mass difference is well described by Equation (3.15) in all cases, including the heavy-light mesons.

Figure 3.11 shows the kinetic mass difference as a function of M_1 for both light, heavy-light and heavy-heavy states, all lying on the free field curve.

We define the nominal heavy quark kinetic mass shift $\Delta_m(Q)$ as

$$\Delta_m(Q) = \frac{M_{2ps}(Q\bar{Q}) - M_{1ps}(Q\bar{Q})}{2}. \tag{3.17}$$

We define the discrepancy in a system as the mass shift in that system with the heavy quark mass shifts of the constituent heavy quarks subtracted

$$D_{kin}(P) = M_2(P) - M_1(P) - \sum_{h \in P} \Delta_(Q_h). \tag{3.18}$$

Figure 3.11: Pseudoscalar kinetic mass and free field value

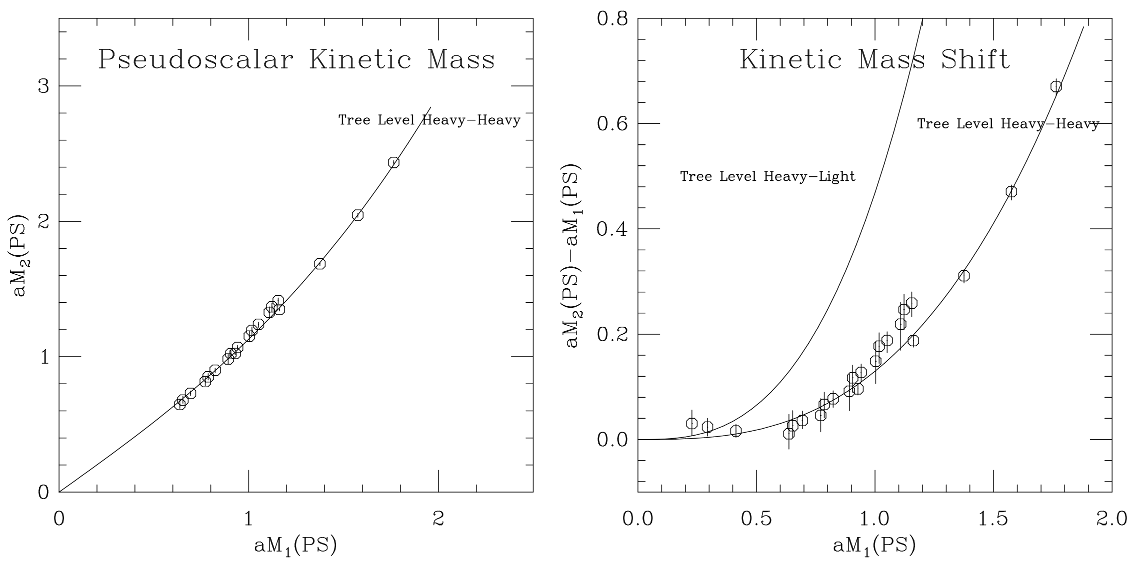

Figure 3.12 presents the kinetic mass shift discrepancies D_{kin} in heavy-light and non-degenerate heavy-heavy systems. This effect was noted by Collins et al [49], with the conclusion that it is not possible to consistently determine κ_Q for both quarkonia and heavy-light systems while simulating with Wilson type quarks on current lattices, where $am_Q \geq 0.5$.

When comparing the same quarks in different states, the consistency of the mass shift is much better. Figure 3.13 shows the difference in the mass shift between the vector and pseudoscalar states in heavy-light (diamonds) and heavy-heavy (circles) systems.

$$\delta\Delta_m(\text{Hyperfine}) = (M_2(ps) - M_1(ps)) - (M_2(v) - M_1(v)) \quad (3.19)$$

$$= (M_1(v) - M_1(ps)) - (M_2(v) - M_2(ps) \quad (3.20)$$

The difference is consistent with zero within statistics, while the statistical error on the M_2 determination discourages its use in calculating mass splittings.

Further problems would occur if attempting to calculate the M_2 for P-states; firstly the statistical noise is much larger in these states, rendering the non-zero momentum channels exceedingly noisy. The more subtle reason is that the projection onto non-zero momentum is parity indefinite, and so the ground states for our angular momentum 0 and 1 operators at non-zero momentum are in fact the pseudoscalar and vector.

Following the Fermilab interpretation of the heavy Wilson quark action [27] we therefore fix the quark mass using $M_2(ps)$ and determine the mass splittings for the various states at this quark mass using the differences in the pole masses. It will be demonstrated later that this prescription for the quark mass produces near scaling behaviour for the hyperfine splittings.

Figure 3.12: Inconsistency of pseudoscalar kinetic mass shift in different systems

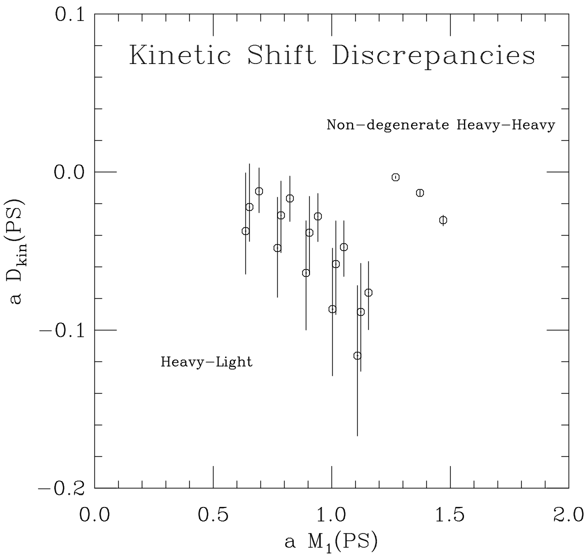

Before getting involved in the extrapolations of the data to physical quark masses, it is convenient to determine the lattice spacing from the quarkonium S-P splitting for later use, and to present the unextrapolated data for the hyperfine splitting.

Figure 3.13: Kinetic mass consistency between pseudoscalar and vector systems

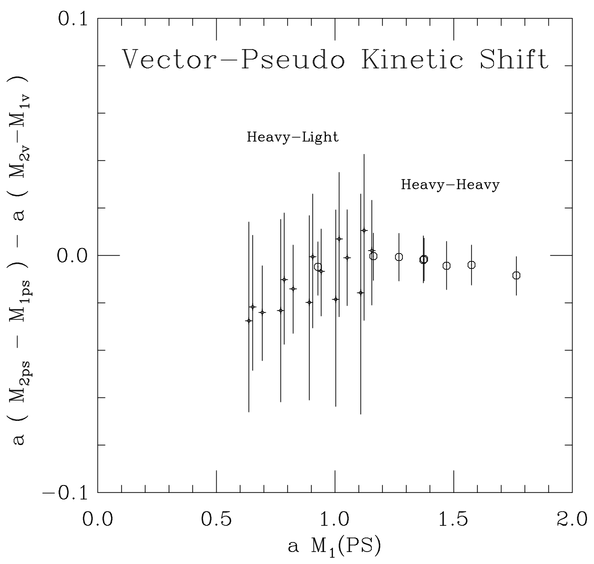

3.5 Scale from Quarkonium S-P splitting

Experimentally the J/ψ and Υ $S-P$ splittings are the same to 2%. Since this mass splitting is empirically independent of M_Q, we should be able to simulate with a sufficiently heavy bare quark mass, extract the splitting, and use this to set the scale.

When quarkonia have been simulated (using either NRQCD or the heavy Wilson approach) quenched calculations have obtained a large slope that does not exist in experiment. This definition of the lattice spacing therefore depends on the mass of the heavy quarks used to determine it. The mass dependence of the lattice spacing found using tadpole improved quarks on this lattice is shown in Figure 3.14.

The question arises of how to interpret this slope. It has been claimed [50] that the slope arises because of the incorrect running of the quenched effective coupling from soft scales to scales of $O(M_Q)$ and that a^{-1} appropriate to quarkonia should

Figure 3.14: Inverse lattice spacing from quarkonium S-P splitting

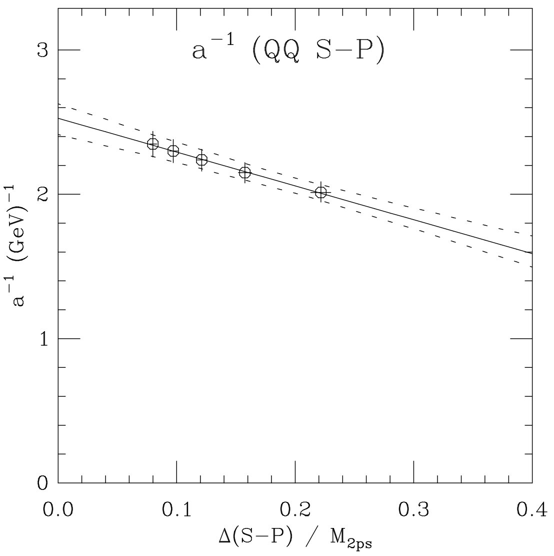

be set using the S-P splitting.

The inverse lattice spacings at $\beta = 6.0$ obtained for J/ψ and Υ are 2.17(6) and 2.4(1) GeV respectively. The value obtained using NRQCD on the same lattice was 2.5(1) GeV for the Υ systems [51]. The inverse lattice spacings obtained from M_ρ and $\sqrt{K}$ are 1.96(4) and 2.02(3) GeV respectively.

3.6 Hyperfine Splitting

A non-relativistic potential model argument, Section 2.5.1, gives that for sufficiently light quarks the quantity $(M_v^2 - M_{ps}^2)$ is constant, and we compare the simulation data using both M_1 and M_2 to define the $(M_v + M_{ps})$ factor in Figure 3.15.

Here m_ρ has been used to set the scale so that the data are normalised to experiment at zero pseudoscalar mass. The experimental points are flat for the light and heavy-light systems, while lying slightly higher for J/ψ. This proba-

Figure 3.15: Hyperfine splitting

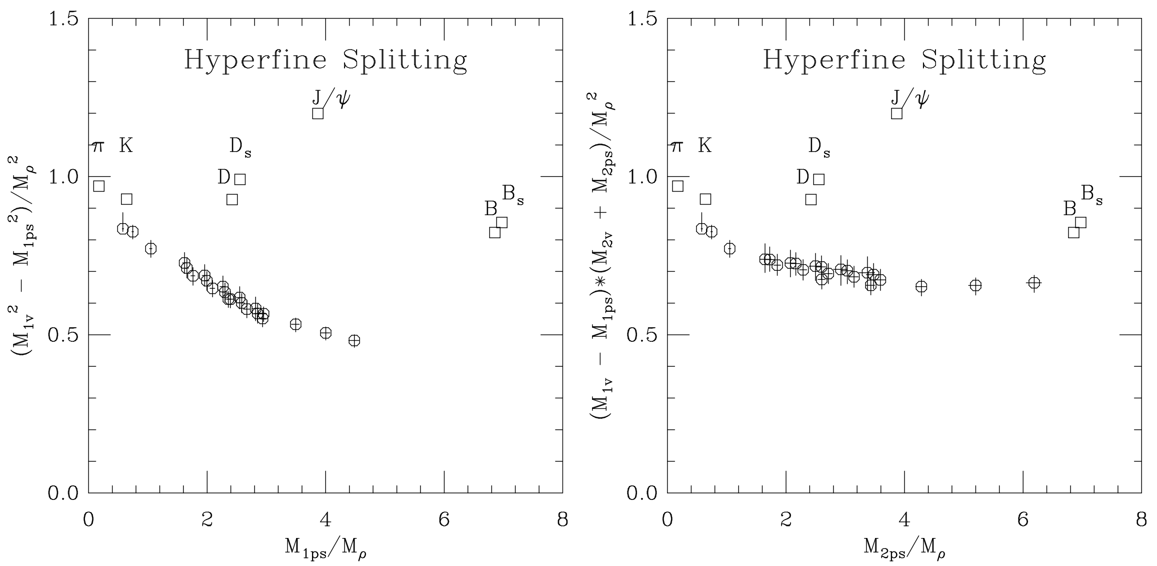

bly results from the quarkonium S-states being significantly determined by the Coulomb part of the potential. The simulation is indeed very flat above the D meson using M_2, and somewhat worryingly there are no "emergent" quarkonium points. Since the data is normalised at zero quark mass, it appears that in the quenched approximation the hyperfine splittings fall disproportionately quickly with quark mass when compared with the real world in the π, K, D sector. This statement does not depend on the (constant) choice of lattice spacing.

We now proceed to extrapolate to the physical quark masses and make phenomenological predictions.

3.7 Light Quark Sector

In order to study the heavy quark spectrum we must obtain both $\kappa_{\rm crit}$ and $\kappa_{\rm strange}$ from the light meson spectrum.

At zero bare quark mass the Wilson term breaks chiral symmetry and so there is no associated Ward identity. This allows the pseudoscalar mass to acquire an additive renormalisation, and the pion mass therefore vanishes at some hopping parameter $\kappa_{\rm crit}$, differing from the free value of $\frac{1}{8}$, defined by

$$m_\pi^2(\kappa_{\rm crit}) = 0. \tag{3.21}$$

Chiral symmetry at zero quark mass should be restored in the continuum since the Wilson term is an irrelevant operator. The PCAC relation [3] implies that

$$m_\pi^2 f_\pi \pi(x) = \partial_\mu A^\mu(x) = 2im_q\pi(x), \tag{3.22}$$

giving that $m_\pi^2 \propto m_q$. We therefore perform a fit to the form

$$m_{\rm Pseudo}^2 = A(\frac{1}{2\kappa_{eff}} - \frac{1}{2\kappa_{\rm crit}}), \tag{3.23}$$

where

$$\frac{1}{\kappa_{eff}} = \frac{1}{2\kappa_1} + \frac{1}{2\kappa_2} \tag{3.24}$$

obtaining Figure 3.16. Determining $\kappa_{\rm crit}$ using a quadratic model,

$$m_{\rm Pseudo}^2 = A(\frac{1}{2\kappa_{eff}} - \frac{1}{2\kappa_{\rm crit}}) + B(\frac{1}{2\kappa_{eff}} - \frac{1}{2\kappa_{\rm crit}})^2, \tag{3.25}$$

does not significantly alter the result, while the linear model has an acceptable χ^2. The resulting bootstrap distribution with $\kappa_{\rm crit} = 0.139249(12)$ was used in subsequent extrapolations.

3.7.1 Lattice ρ mass determination

Similarly we determine the lattice ρ mass by fitting the form

$$M_v(\kappa_{\rm eff}) = m_\rho + A(\frac{1}{2\kappa_{eff}} - \frac{1}{2\kappa_{\rm crit}}), \tag{3.26}$$

as shown in Figure 3.17. We find that $aM_\rho = 0.393(8)$, and the bootstrap distribution was used in later fits.

Figure 3.16: Determination of $\kappa_{\rm crit}$ from pion mass

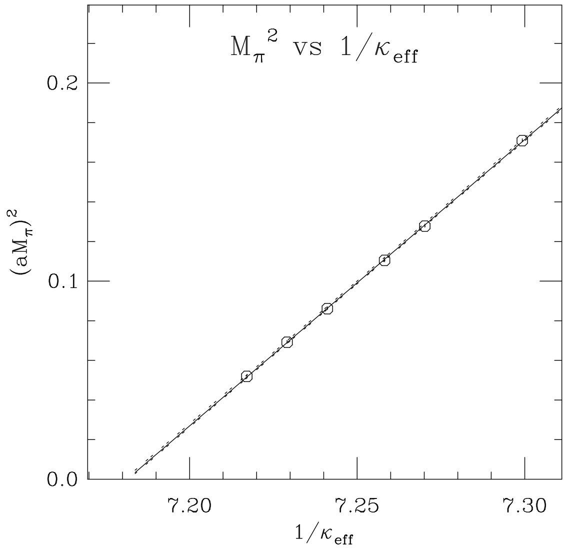

Figure 3.17: Determination of $M_\rho(\text{crit})$ from lattice data

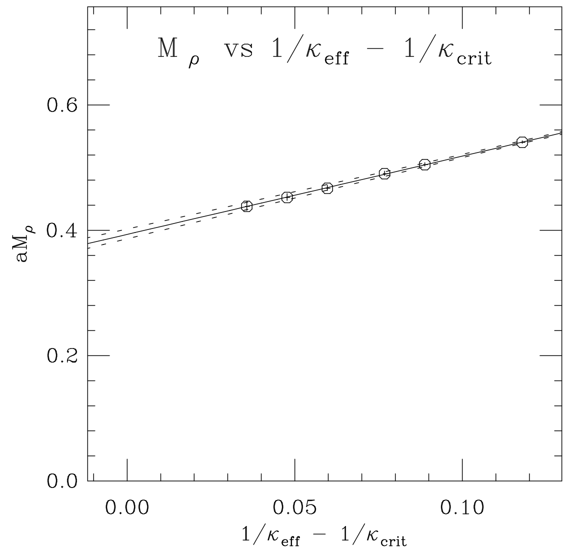

3.7.2 $\kappa_{\rm strange}$ Determination

We now determine $\kappa_{\rm strange}$ from the physical value of the K mass to ρ mass ratio to obtain $\kappa_{\rm strange} = 0.13756(7)$, as shown in Figure 3.18.

Figure 3.18: Determination of $\kappa_{\rm strange}$ from $\frac{M(K)}{M(\rho)}$

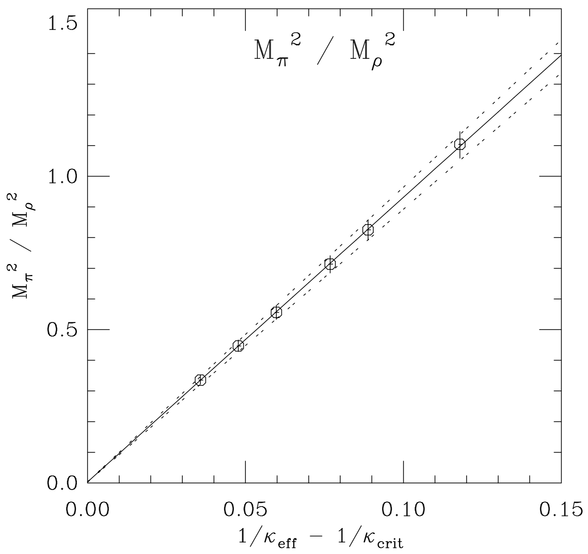

We now have the required light sector results to analyse the heavy-light spectrum.

3.8 Heavy Light Mesons

Motivated by the Chiral and HQET approximate symmetries we fit all masses and mass splittings as a linear function of the light quark mass in a given heavy-light system, then perform either linear or quadratic extrapolations in the inverse heavy quark mass for mass splittings at (fixed) $\kappa_{\rm crit}$ and $\kappa_{\rm strange}$.

$$\Delta_{m_Q}(m_q) = A(m_Q) + B(m_Q)(\frac{1}{2\kappa_{eff}} - \frac{1}{2\kappa_{\rm crit}}) \tag{3.27}$$

$$\Delta_q(m_Q) = \Delta(\infty) + C\frac{1}{m_Q} + D\frac{1}{m_Q^2}. \tag{3.28}$$

Here we may choose D to be zero and perform linear fits to the m_Q dependence if this model is deemed appropriate, however this cannot be an a priori assumption, and is instead empirically determined from the lattice data. Since there are only three light quarks we are restricted to using a linear model in all cases for the m_q dependence. Figure 3.19 presents the typical chiral extrapolation for the heavy-light hyperfine splitting; likewise Figure 3.21 and Figure 3.22 present the typical chiral extrapolation for the S-P splitting and the $1^+ - 0^+$ fine splitting respectively. These fits were used to create bootstrap distributions for each of the splittings for each heavy quark at κ_{crit} and κ_{strange}.

Figure 3.19: Chiral extrapolation of heavy-light hyperfine splitting

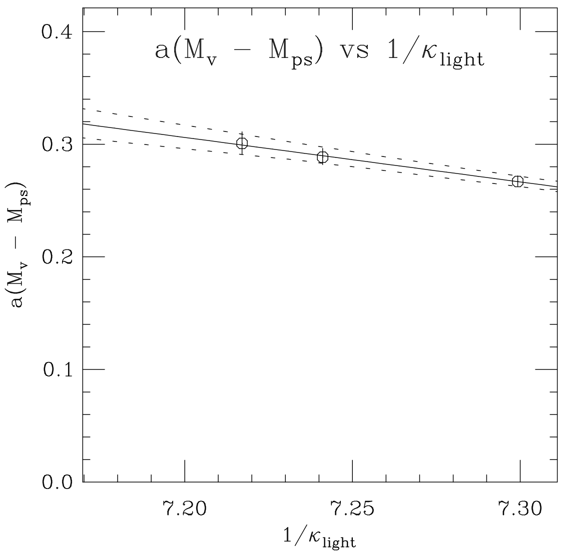

The chiral extrapolations of the P-states were somewhat problematic, generally the fitted mass for the $\kappa = 0.13856$ quark was heavier than the $\kappa = 0.13810$ quark, with increased error, Figure 3.20.

This does not make sense physically, and may be either statistical fluctuation,

Figure 3.20: Light quark mass dependence of fitted heavy-light P-state

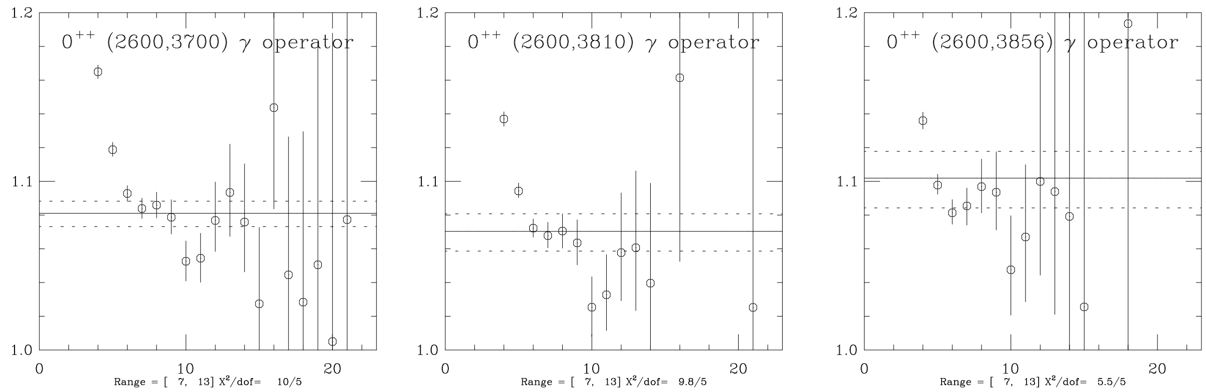

or a systematic effect from the increased noise on this correlator making plateau identification difficult. In order to proceed, only the $\kappa = 0.13700$ and $\kappa = 0.13810$ points were used in the chiral extrapolations of these states, Figure 3.21 and Figure 3.22, and in the analysis of the chirally extrapolated value we bear in mind that there may be an unknown systematic error in the light quark dependence.

3.8.1 Heavy Quark Extrapolations

We fix the bare quark masses for charm and for beauty by requiring that the kinetic mass of the relevant Q_s pseudoscalar meson have its physical value. This must be done using some other observable to set the scale for the dimensionless mass, and given the discussion of Section 3.1, the bare quark mass obtained depends on this choice. The same analysis was performed using the string tension, the ρ mass, and the quarkonium S-P splitting to set the scale, however the extrapolations are identical up to multiplicative constants on both axes, so that I show only the extrapolations performed for the string tension though results will be quoted for each method. The extrapolations shown for the heavy-strange mesons used the Kaon to ρ mass ratio to fix the bare strange quark mass.

The hyperfine splittings with massless and strange light quarks are extrapolated

Figure 3.21: Chiral extrapolation of heavy-light S-P splitting

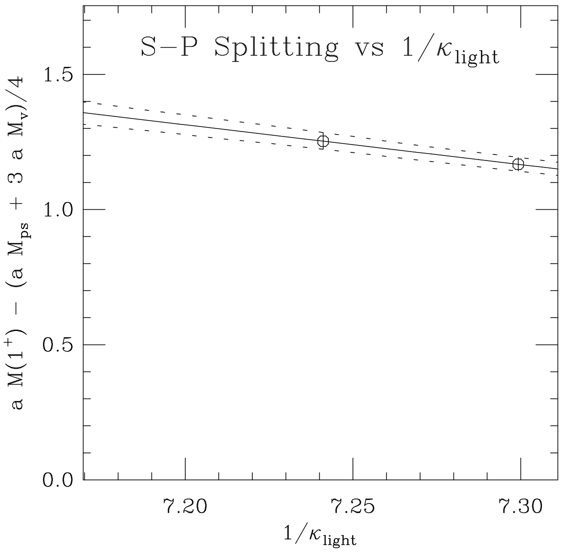

Figure 3.22: Chiral extrapolation of heavy-light $1^+ - 0^+$ fine splitting

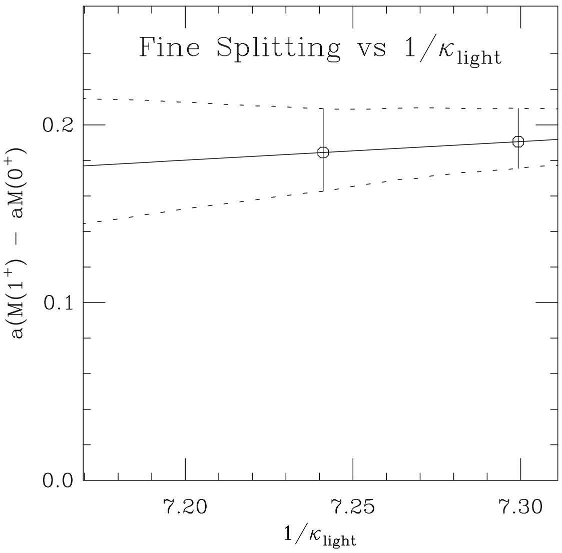

Figure 3.23: Heavy quark extrapolation of heavy-strange hyperfine splitting

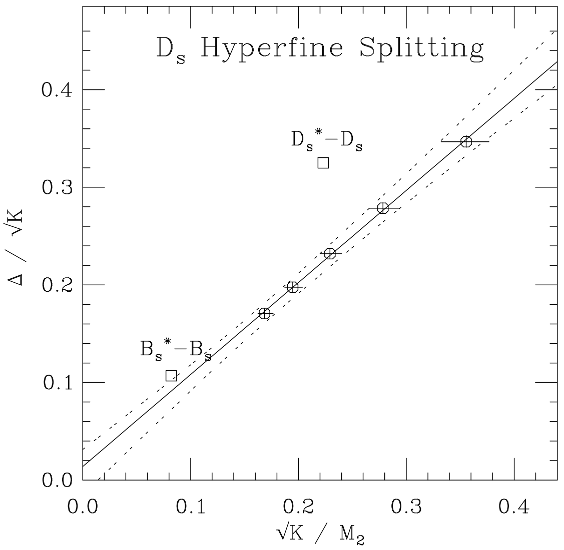

Figure 3.24: Heavy quark extrapolation of heavy-light hyperfine splitting

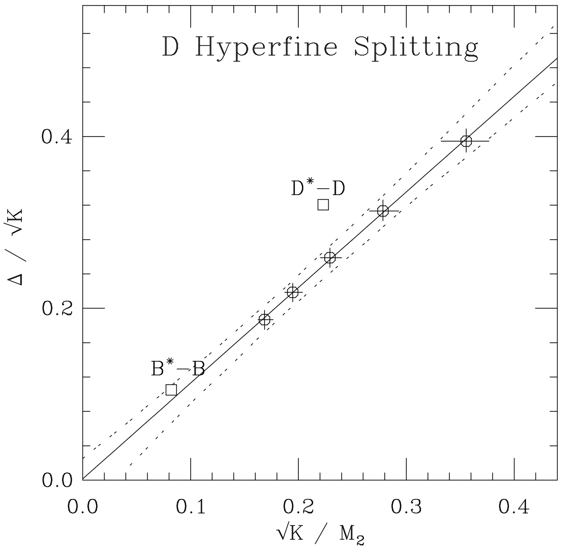

in Figure 3.24 and Figure 3.23 respectively. These figures are linear fits, and have a very acceptable χ^2/dof, showing that a linear dependence on $\frac{1}{M}$ is the appropriate model with this level of statistical error.

As can be seen the hyperfine splitting is consistent with a straight line passing through the origin, which is as both HQET intuition and experimental evidence suggest. The splitting does however appear to be systematically low, and whether this is a quenching or discretisation effect shall be discussed when analysing the scaling behaviour in chapter 4. The adequacy of a linear fit to the data was found to be typical of the analysis, and shall not commented on again, however it should be noted that this was not a priori clear, and is a conclusion based upon the non-perturbative calculation rather than model dependent input.

Figure 3.25: Previous heavy quark extrapolation of hyperfine S-P splitting

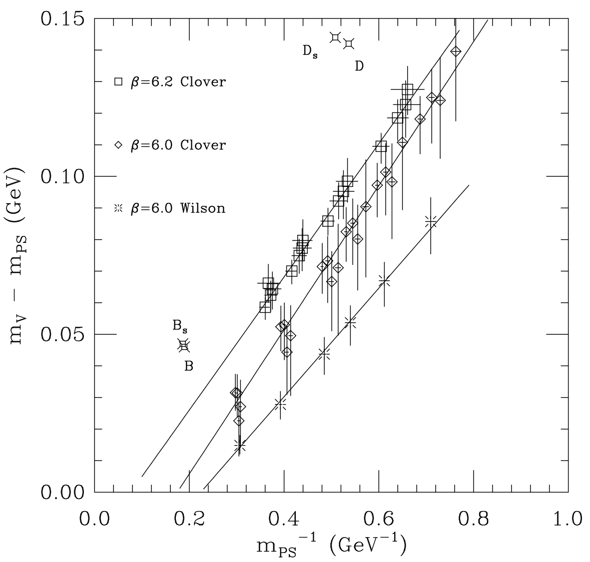

Previous UKQCD results for the hyperfine splitting using the unimproved Wilson and tree-level Clover actions can be found in Figure 3.25, and, as can be seen, do not pass through the origin, thus violating a HQET prediction. This is not a surprise since the leading discretisation correction $\sigma_{\mu\nu}F^{\mu\nu}$ is precisely the leading heavy quark spin coupling, so that reducing the discretisation effects associated with this operator has plausibly brought us closer to the HQET predicted behaviour.

Figure 3.26: Heavy quark extrapolation of heavy-strange S-P splitting

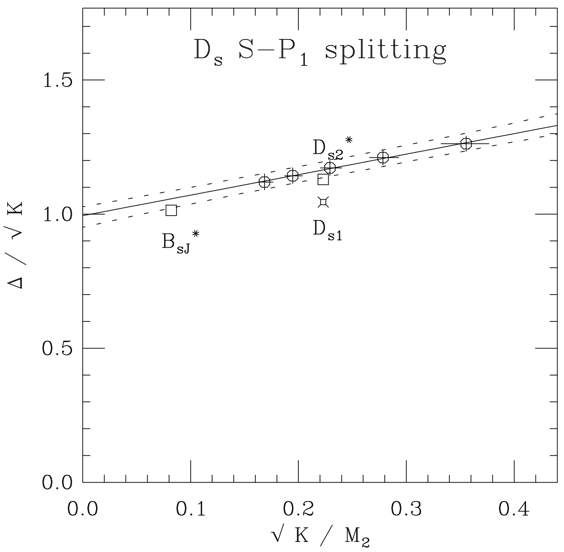

The extrapolations of the heavy-light S-P splittings can be found for strange and massless light quarks in Figure 3.26 and Figure 3.27 respectively. The experimental points in these plots are not directly comparable since they correspond to $j_{\text{light}} = \frac{3}{2}$ systems, however they are estimated to differ by only $O(50)$MeV [39], and serve as a guide to the plausibility of the lattice data. The results for the strange quark are reasonable while the chirally extrapolated point appears to be too high. The chiral extrapolations of the P-states are in question, however, so this is not unduly worrying. An NRQCD calculation [52] on the same configurations found that the mass of the P-state was independent of the light quark mass within statistical error, giving a similar behaviour when chirally extrapolating the P-states (since the S-states differ by $O(100)$ MeV).

We predict the spin averaged $D_s - D$ splitting, the extrapolation of which is given

Figure 3.27: Heavy quark extrapolation of heavy-light S-P splitting

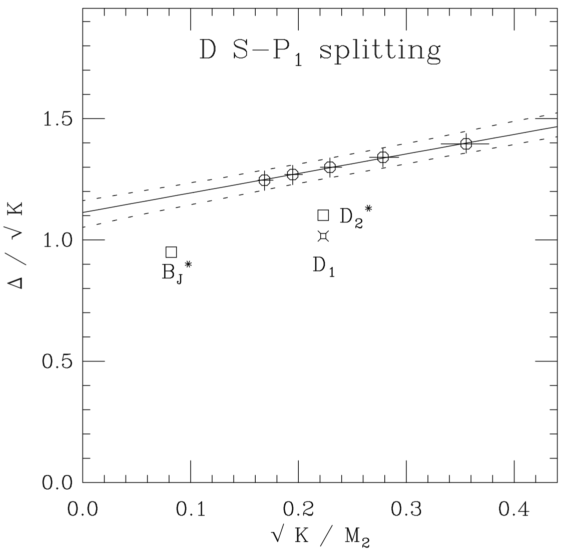

in Figure 3.28. This shows a satisfactory agreement with experiment using the string tension.

A signal for the $1^+ - 0^+$ splitting was obtained, surviving chiral extrapolation, although, as mentioned, the extrapolation to the chiral limit may be dubious. The splitting is extrapolated to the charm and beauty masses in Figure 3.29 and Figure 3.30. As discussed in Chapter 2, the ground state of the 1^+ correlators is the $J_{\text{light}} = \frac{1}{2}$ physical state, which is split from the 0^+ by terms proportional to $\frac{1}{M}$. The slope of the D_s extrapolation is plausible, however the question of resolving $1^+ - 1^{+\prime}$ mixing is still a great challenge that will require better smearing and analysis techniques, and this sector is still far from well understood. The option of increasing the Monte-Carlo sample, while helping the analysis is not going to solve this issue without improved calculational techniques.

Table 3.9 presents the spectral quantities calculated using the three scale setting observables for both the D and B systems. The error on the scaling quantity has

Figure 3.28: Heavy quark extrapolation of strange-critical spin averaged splitting

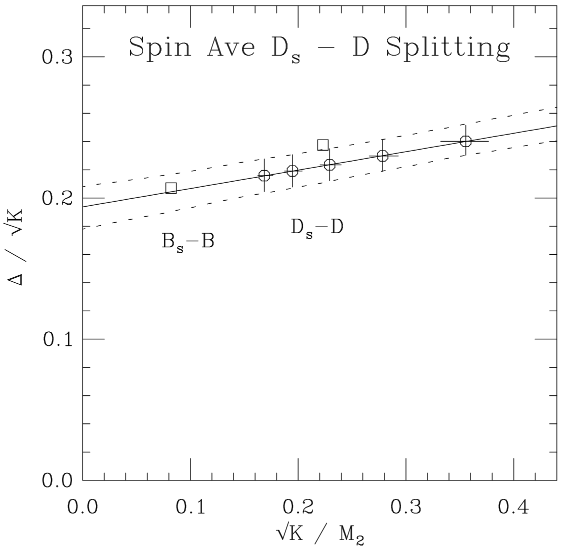

Figure 3.29: Heavy quark extrapolation of heavy-critical 1^+ - 0^+ splitting

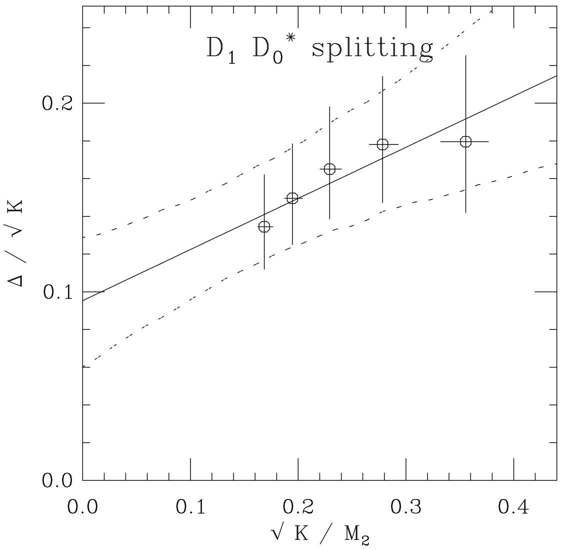

Figure 3.30: Heavy quark extrapolation of heavy-strange 1^+ - 0^+ splitting

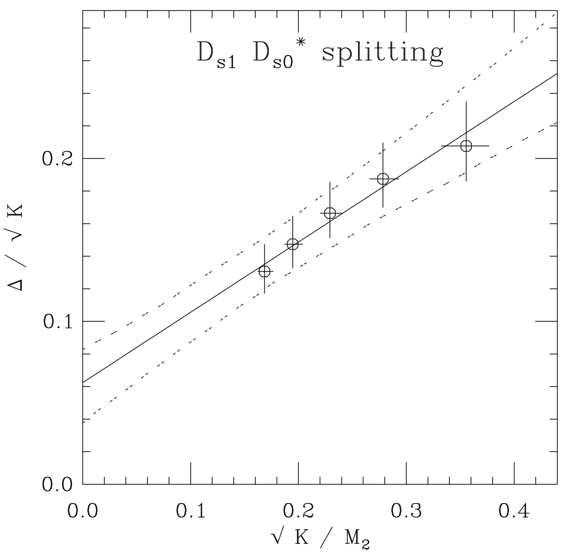

been bootstrapped for the M_ρ and S-P splitting definitions. There is no calculation of the string tension on the same configurations, so that an uncorrelated error was assumed, and the rules for addition of Gaussian noise used to add the contribution to the statistical error on each splitting. In most cases the error due to the string tension is negligable compared with the error in the hadronic observables, leaving this an acceptable, if somewhat redundant procedure.

As an illustration of the calculation results Figure 3.31 shows the D meson spectrum predicted by the simulation, while Figure 3.32 shows the results extrapolated to the B meson. In both these diagrams the string tension was used to set the scale and the results are fixed relative to the spin average of the heavy-strange S-state, so that the overall position of the linear combination of $\frac{D_s+3D_s^*}{4}$ is not a prediction, and likewise for the B. This combination was chosen since it is statistically relatively clean and contains no leading order spin dependent terms which are thought to be poorly approximated by quenching.

Table 3.9: $\beta = 6.0$ heavy-light mass splittings

Splitting (MeV)	$\sqrt{K}$	M_ρ	$Q\bar{Q}$ S-P Splitting	Experiment
$D^* - D$	110(7)	106(8)	129(10)	142
$D_s^* - D_s$	99(5)	95(6)	115(9)	144
$\bar{D}_s \bar{D}$	98(5)	96(5)	107(6)	105
$D_1 \bar{D}$	540(30)	530(30)	600(30)	459
$D_{s1} \bar{D}_s$	494(18)	480(20)	545(20)	460
$D_1 D_0^*$	45(20)	44(20)	47(25)	-
$D_{s1} D_{s0}^*$	57(12)	56(11)	64(13)	-
$B^* - B$	41(9)	39(10)	59(11)	46
$B_s^* - B_s$	40(6)	38(7)	57(8)	47
$\bar{B}_s \bar{B}$	90(6)	88(6)	110(7)	91
$B_1 \bar{B}$	490(30)	480(30)	590(40)	419
$B_{s1} \bar{B}_s$	440(20)	430(20)	540(30)	446
$B_1 B_0^*$	50(20)	50(20)	60(20)	-
$B_{s1} B_{s0}^*$	43(11)	42(10)	54(12)	-

Figure 3.31: D spectrum diagram using string tension to set scale

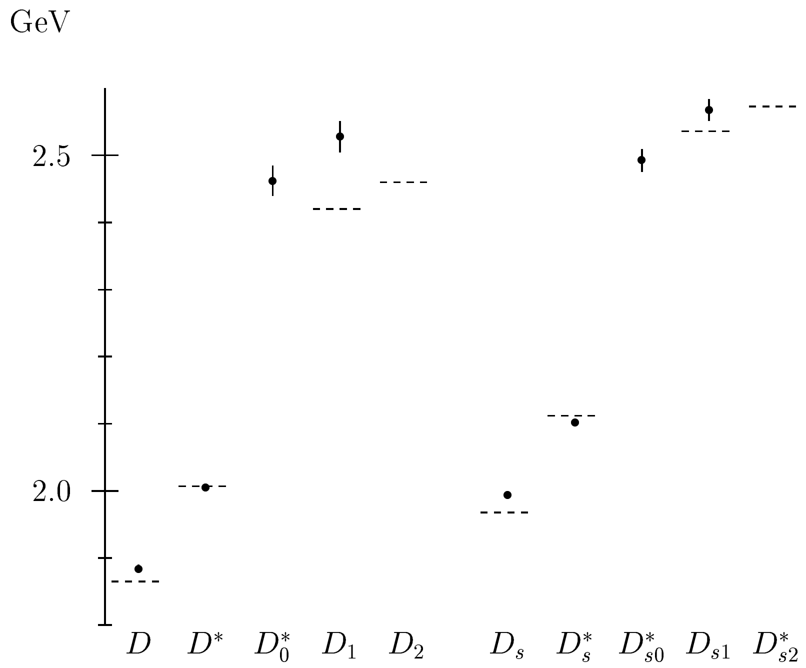

Figure 3.32: B spectrum diagram using string tension to set scale

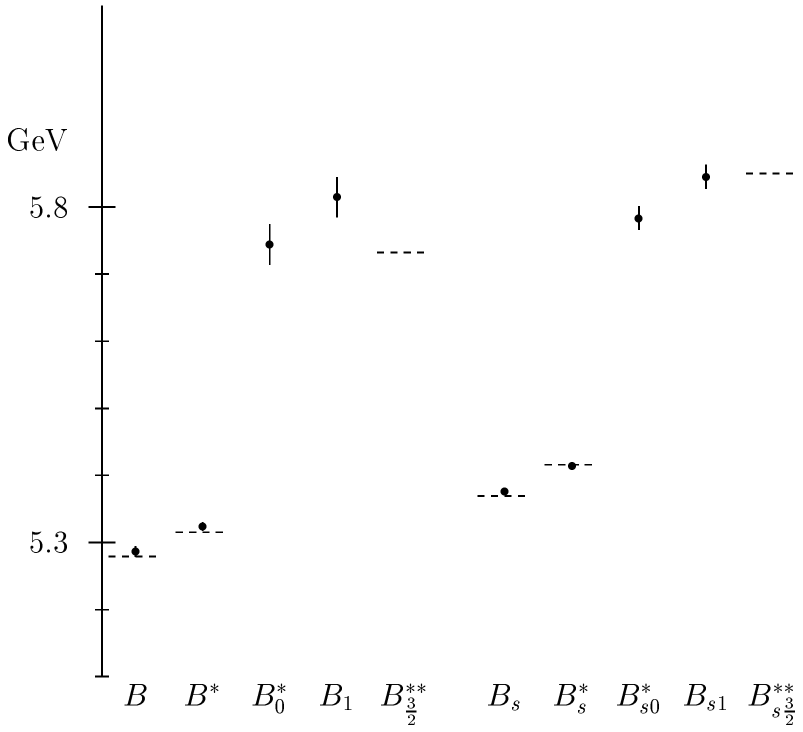

3.8.2 Relevant NRQCD Calculations

For comparison, some results obtained using the leading competing approach for heavy-light spectroscopy, namely mixing the NRQCD heavy quark formulation with some form of the Wilson action for the light quarks, are presented here; the plots were obtained from the source in the hep-lat e-print archive. Because NRQCD breaks down for $aM_Q \leq 1$ these calculations are only available for the B meson.

A subset of 35 of the UKQCD configurations were used to calculate NRQCD heavy quarks with tree level clover light quarks, obtaining the following plots Figure 3.33 and Figure 3.34 [52]. The results obtained for the quenched NRQCD B spectrum are given in Table 3.10.

Collins et al [53] calculated the heavy-light spectrum using 100 samples of a dynamical gauge distribution at $\beta = 5.6$, with two sea quarks of mass $aM_Q = 0.01$,

Table 3.10: $\beta = 6.0$ NRQCD-clover mass splittings

Splitting	MeV
$\bar{B}_s - \bar{B}$	100(14)
$B^* - B$	46(6)
$B_s^* - B_s$	47.0(2.6)
$B^{**} - \bar{B}$	550(40)

Figure 3.33: Quenched NRQCD (squares) and tree level clover (circles) heavy-light hyperfine splitting at a non-physical light quark mass

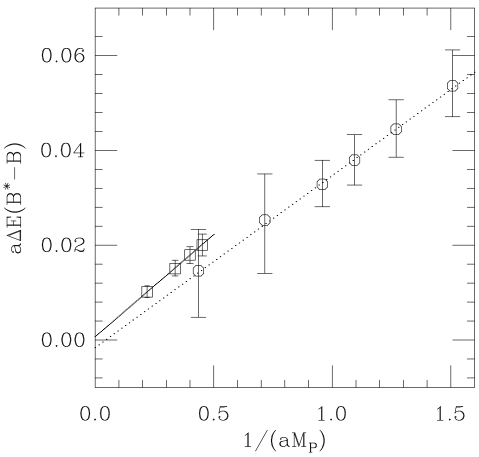

Figure 3.34: Quenched NRQCD and tree level clover S-P splitting at a non-physical light quark mass

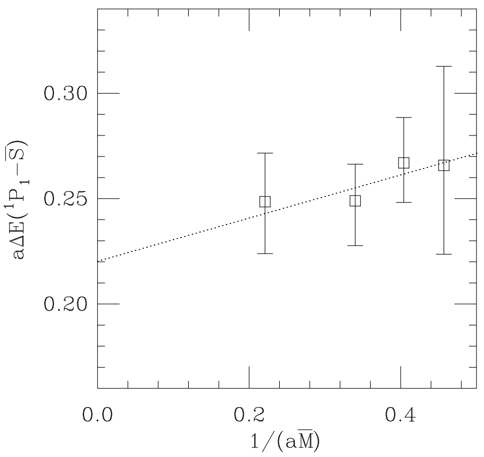

corresponding to a lattice spacing from the string tension of $a^{-1} = 2.05$ GeV. The calculation is therefore broadly comparable to our $\beta = 6.0$ quenched calculation. The spectrum results quoted are given in Table 3.11 and include an error estimate encompassing the different methods for setting the scale. The heavy quark extrapolations of the hyperfine and S-P splitting are given in Figure 3.35 and Figure 3.36. None of the NRQCD heavy-light spectrum calculations have obtained evidence for the fine structure.

Figure 3.35: NRQCD heavy - Wilson light hyperfine splitting with dynamical staggered quarks

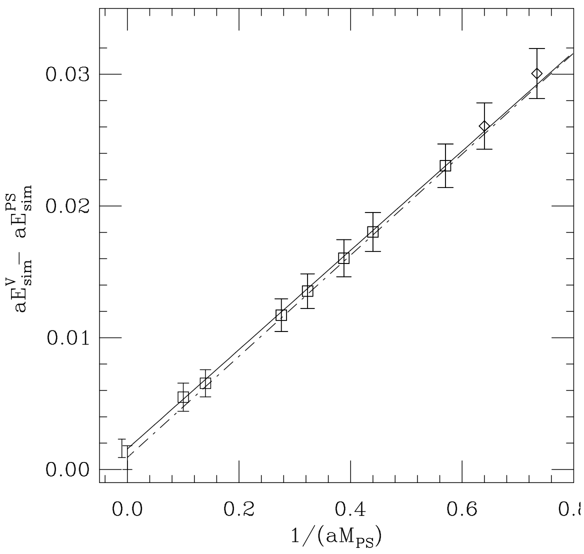

Table 3.11: $\beta = 5.6$ NRQCD B spectrum with staggered sea quarks

Splitting	MeV
$\bar{B}_s - \bar{B}$	90-130
$B^* - B$,$B_s^* - B_s$	25-40
$B^{**} - \bar{B}$	400-700

Figure 3.36: NRQCD and Wilson heavy-light S-P splitting with dynamical staggered quarks

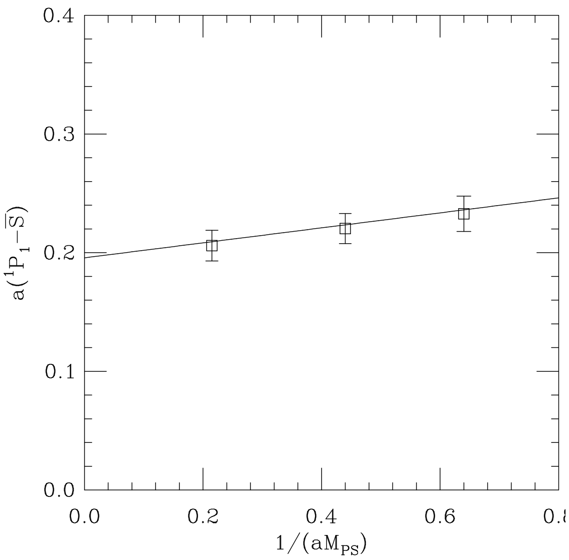

3.9 Heavy Heavy Mesons

As with the heavy-light meson analysis, the extrapolations in heavy quark mass for the heavy-heavy systems were amenable to a linear fit at the current level of statistical errors. The hyperfine splitting, S-P splitting and 1^{+-} - 1^{++} - 0^{++} fine structure were calculated and extrapolated using degenerate pairs of quarks.

Figure 3.37: Heavy quark extrapolation of quarkonium hyperfine splitting

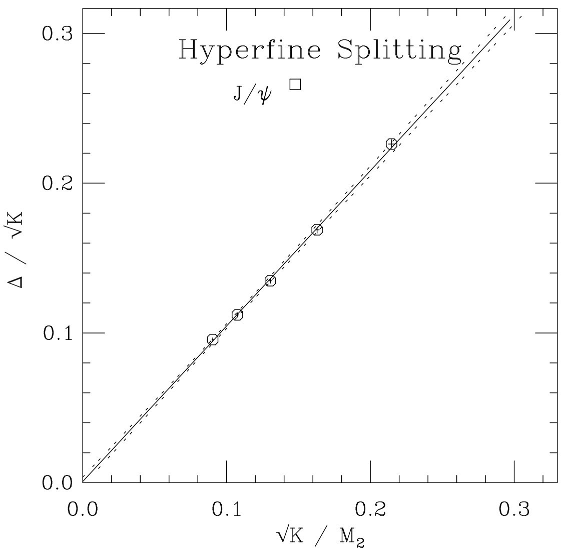

Figure 3.37 presents the extrapolation of the quarkonium hyperfine splitting using the string tension to scale the extrapolation. The mass dependence of the splitting is a straight line through the origin, in agreement with the non-relativistic expansion of QCD, and in contrast to the extrapolations obtained with the tree-level clover and unimproved Wilson actions, [54, 55], as seen in Figure 3.38. The slope of the hyperfine splitting is in clear disagreement with experiment. Such a discrepancy is expected, Section 2.5.2, to occur due to quenching, but evidence of scaling is required to rule out discretisation effects.

The S-P splitting is extrapolated in Figure 3.39, and appears to display a stronger

Figure 3.38: Previous heavy quark extrapolation of quarkonium hyperfine splitting

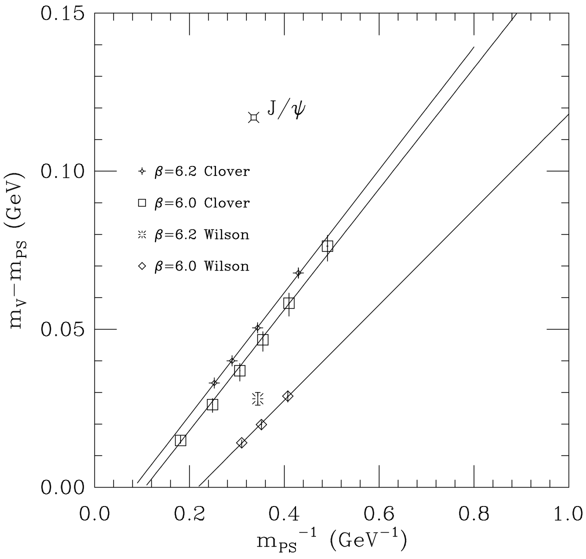

Figure 3.39: Heavy quark extrapolation of quarkonium S-P splitting

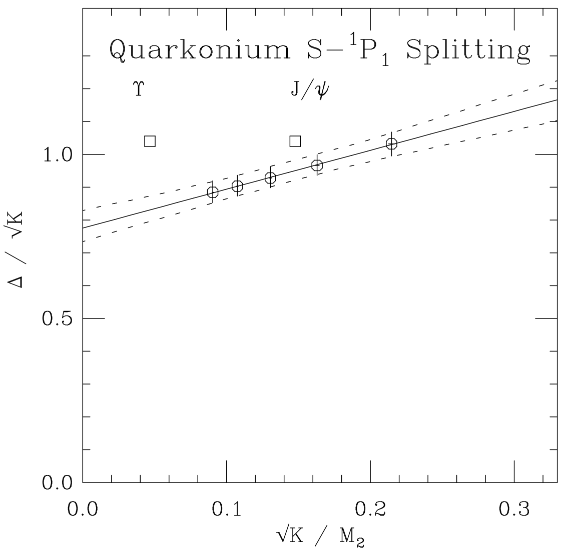

slope than experiment, while broadly agreeing at sufficently light quark masses. This manifests itself as a rise in a^{-1} defined by the quarkonium S-P splitting at larger quark masses, and is commonly interpreted as resulting from the incorrect running of the quenched coupling from soft to hard scales. This may be a quenching effect, and shall be returned to in the following chapter where the scaling behaviour of the spectrum is discussed, though the use of this quantity to set the scale in a system dependent way depends on whether we wish to form best estimates of phenomenologically undetermined quantities, or look at the deficiencies of the quenched spectrum. Currently the first lattice calculations incorporating the effect of Wilson sea quarks (at unphysically large mass) are being undertaken, so that the areas where quenching effects were implicitly removed by not analysing the entire spectrum with a uniform choice of scale are now candidates for consistent study, since they should be most sensitive to the presence of such unphysical sea quarks.

The fine structure extrapolations require some explanation. The 2^{++} state required extra derivative source propagators generated only at $\kappa = 0.12600$, so that the fine splittings involving the 2^{++} state were extrapolated using non-degenerate mesons, to the point where the non-degenerate pseudoscalar kinetic mass was equal to the η_c mass.

This analysis is not ideal but can be justified since the non-degenerate Hamiltonian in [29] is easily re-written in terms of the the combinations $(m_1 + m_2)$ and $(m_1 - m_2)$ giving that the corrections to the Hamiltonian for non-degenerate quarks are proportional to $\frac{m_1 - m_2}{m_1 + m_2}$. In extrapolating to charm from the nearby $\kappa = 0.12600$, the correction to the *fine splitting* is of order 10%, which is more than satisfactory for this first calculation, and certainly lower than the level of statistical error. Extrapolations to the beauty systems via this method however are clearly problematic.

The extrapolations are performed using degenerate quarks when not involving the 2^{++} state, and are shown in Figures 3.40, 3.41, 3.42 and 3.43.

Gupta et al presented a signal for the $1^+ - 0^+$ fine splitting for charmonium using unimproved Wilson quarks [56], however, as far as the author knows, this thesis contains the first relativistic calculation that competely resolves the χ triplet.

The results obtained using each of the string tension, the ρ mass, and the quarkonium S-P splitting extrapolated to both the J/ψ and Υ systems can be found in Table 3.12 [2].

As an illustration of the resulting data we present diagrams for the spectrum obtained using the string tension for both the J/ψ, Figure 3.44, and the Υ, Figure 3.45, systems

[2]Using Estimates of η_b and h_b from potential models

Table 3.12: $\beta = 6.0$ heavy-heavy mass splittings

Splitting (MeV)	$\sqrt{K}$	M_ρ	$Q\bar{Q}$ S-P Splitting	Experiment
$J/\psi - \eta_c$	68(2)	65(2)	79(4)	117
$^1P_1 - \bar{S}$	418(13)	408(16)	-	458
$\chi_{c2} - \chi_{c1}$	81(28)	78(27)	93(33)	46
$\chi_{c1} - \chi_{c0}$	51(7)	49(7)	59(11)	95
$\chi_{c2} - \chi_{c0}$	133(28)	128(28)	153(35)	141
$\Upsilon - \eta_b$	22(1)	21(1)	31(3)	40
$^1P_1 - \bar{S}$	366(17)	358(20)	-	460
$\chi_{b2} - \chi_{b1}$	43(30)	42(30)	56(32)	21
$\chi_{b1} - \chi_{b0}$	26(9)	25(9)	33(10)	32
$\chi_{b2} - \chi_{b0}$	65(30)	63(27)	85(32)	53

Figure 3.40: Heavy quark extrapolation of quarkonium $\chi_{c1} - \chi_{c0}$ fine splitting

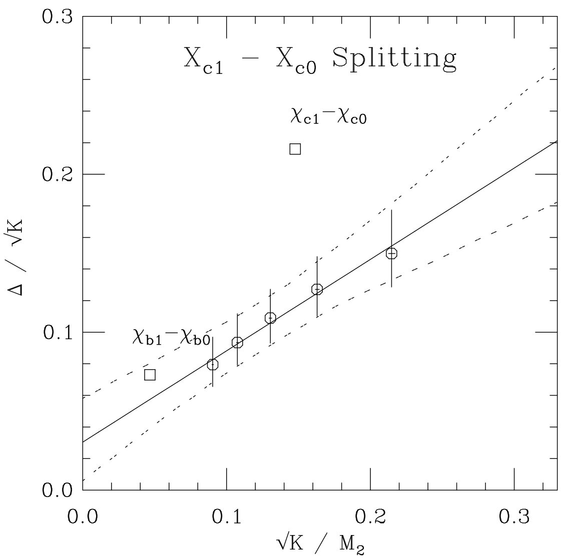

Figure 3.41: Heavy quark extrapolation of quarkonium $\chi_{c1} - h_c$ fine splitting

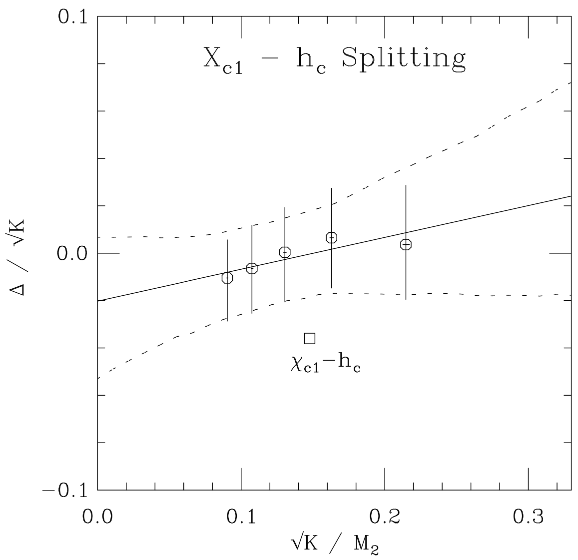

Figure 3.42: Heavy quark extrapolation of quarkonium $\chi_{c2} - h_c$ fine splitting

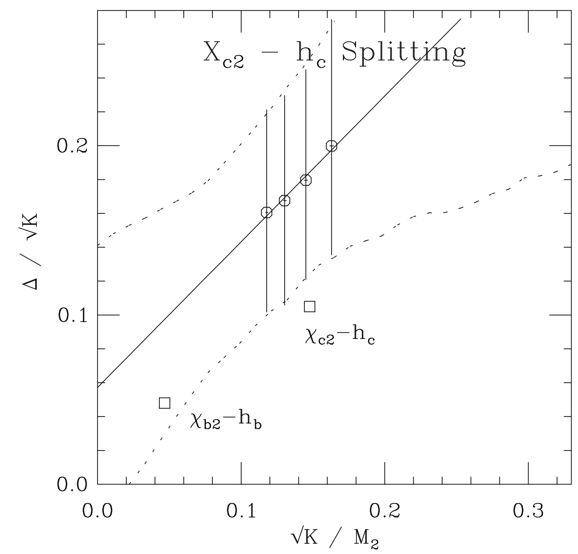

Figure 3.43: Heavy quark extrapolation of quarkonium $\chi_{c2} - \chi_{c0}$ fine splitting

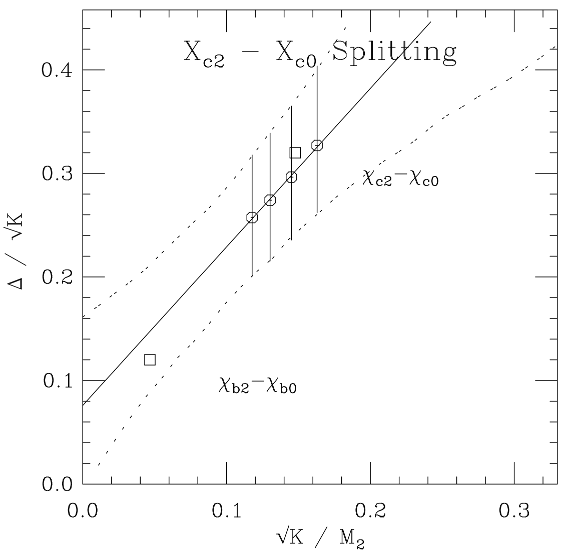

Figure 3.44: Charmonium spectrum diagram using string tension to set scale

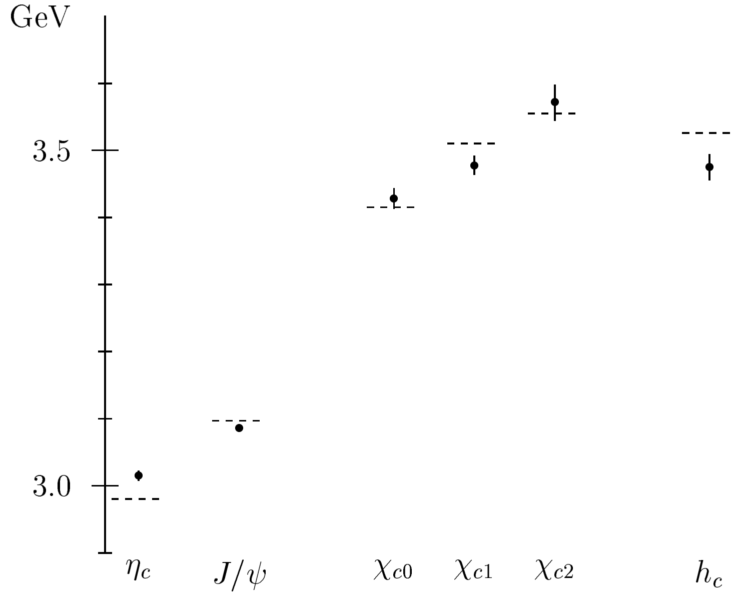

Figure 3.45: Upsilon spectrum diagram using string tension to set scale

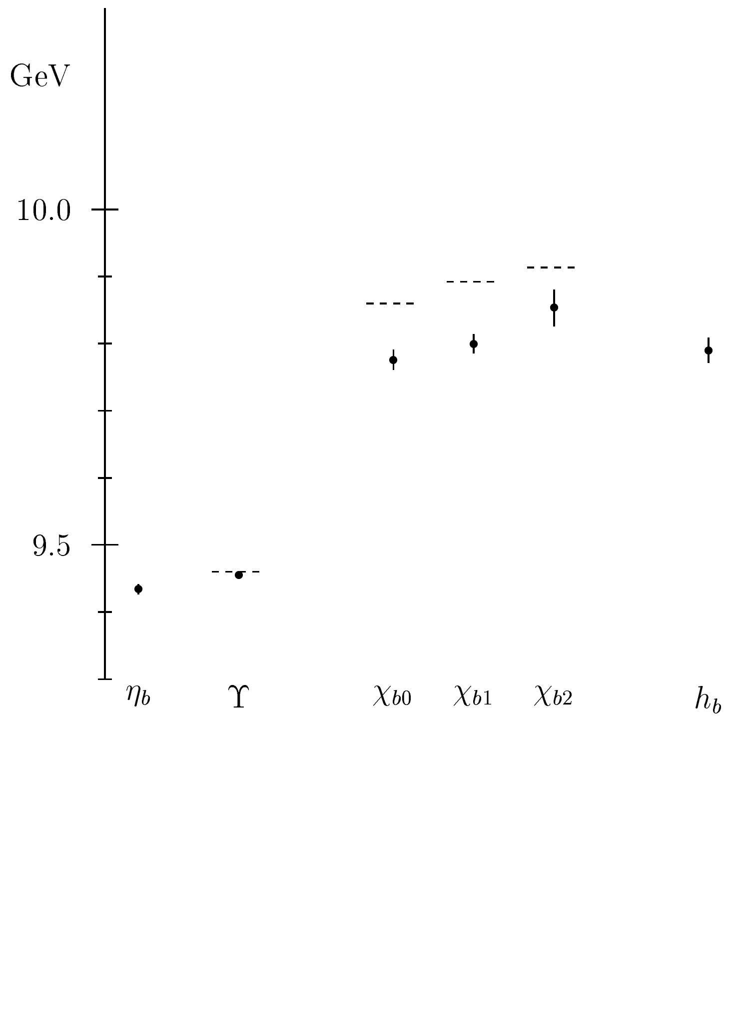

Chapter 4

Scaling Behaviour

In this chapter I present the results of a slightly less extensive calculation performed using the tadpole improved clover action at $\beta = 6.2$ in the form of a scaling analysis for those quantities common to both calculations.

4.1 $\beta = 6.2$ Simulation Details

The simulation was performed using 220 sample gauge configurations from a quenched distribution at $\beta = 6.2$ on a $24^3 \times 48$ lattice using UKQCD time on the Cray T3D at the EPCC in Edinburgh University. Three light quark masses,

$$\kappa_{\text{light}} \in \{0.13640, 0.13710, 0.13745\},$$

and five heavy quark masses,

$$\kappa_{\text{heavy}} \in \{0.12000, 0.12300, 0.12600, 0.12900, 0.13200\},$$

were used, all having the tadpole improved clover action with $C_{SW} = 1.44239$, corresponding to $U_0 = 0.88506$.

Due to constraints of disk space, fewer propagator sources were used than in the previous calculation, so that only the fuzzed source - local sink and the fuzzed source - fuzzed sink meson correlators were available for heavy-light analysis. The fuzzing radius used was found to be non-optimal for the heavy-heavy states, presumably due to the shrinking of the meson size as mass increases, and so the calculation for the heavy-heavy states required the generation of additional propagators, with local sources, on 150 configurations. The data were fitted using a similar procedure to that described in the previous chapter, and tedious details are omitted.

4.2 Lattice Spacing from Quarkonium S-P splitting

As in the previous chapter, one way to determine the lattice spacing is to use the quarkonium S-P splitting, giving a lattice spacing that is quark mass dependent, as shown in Figure 4.1. The inverse lattice spacings obtained for the J/ψ and Υ systems were 2.67(12) and 2.84(16) GeV respectively . The inverse lattice spacings obtained from the string tension and M_ρ are 2.73(5) and 2.61(8) GeV respectively.

Figure 4.1: Inverse lattice spacing from quarkonium S-P splitting at $\beta = 6.2$

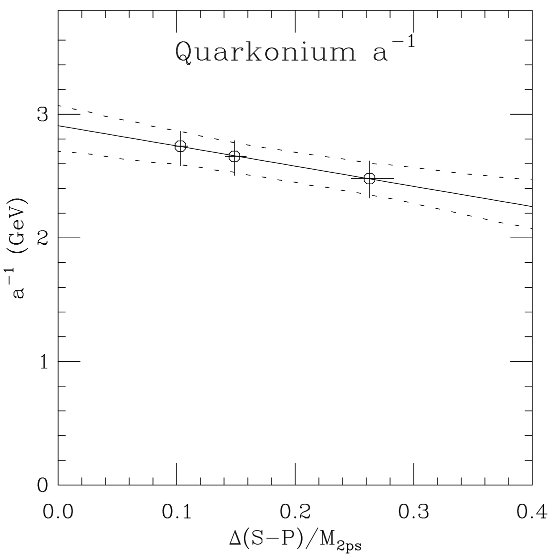

4.3 Heavy-Light Meson Analysis

Following a similar analysis to the previous chapter, we overlay plots showing the heavy quark extrapolations of the mass splittings from the $\beta = 6.2$ calculation (fancy diamonds), and the $\beta = 6.0$ calculation (open circles), using the string tension to scale the axes.

Figure 4.2: D meson hyperfine splitting

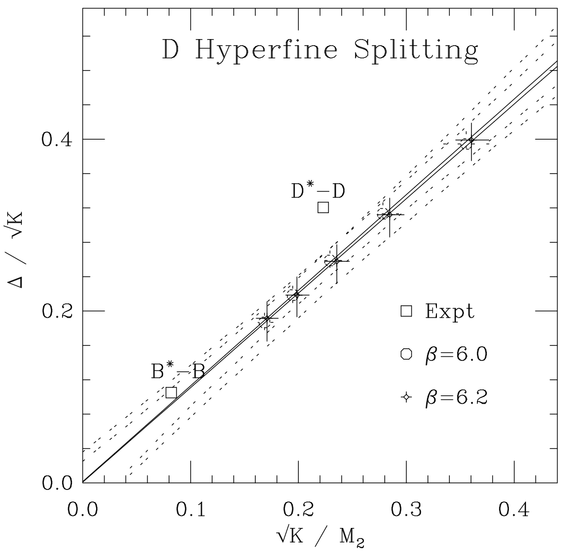

Figure 4.2 and Figure 4.3 present the heavy quark extrapolations of the hyperfine splittings. The results from the two lattices are consistent within statistics, suggesting that the continuum quenched heavy-light hyperfine splittings for the D system are lower than experiment.

The spin averaged S-wave splitting between strange and chiral quarks are presented in Figure 4.4, and are consistent with experiment on both lattices for the D system, but appear to be higher than experiment on the $\beta = 6.2$ lattice once extrapolated to B. However, this is less than a 1 σ effect, and so smaller statistical errors are required to interpret this as an inconsistency.

The smearing was poor for the p-states, so that a signal can only be obtained for the S-P splitting, and this can only be done with large statistical errors compared with the magnitude of the splitting. Within this level of error both

Figure 4.3: D_s meson hyperfine splitting

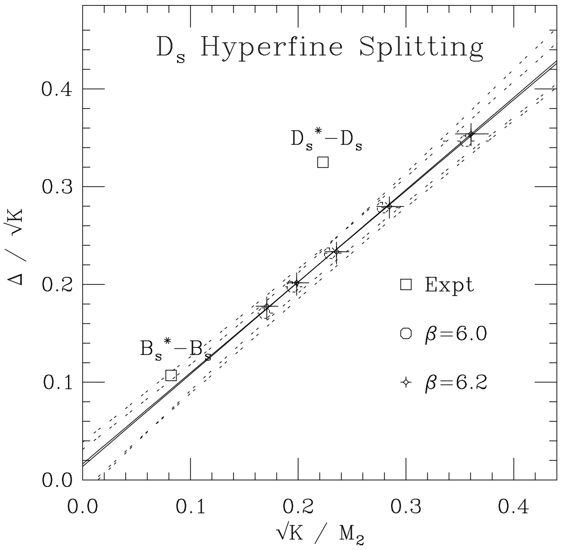

Figure 4.4: $\bar{D}_s - \bar{D}$ spin averaged splitting

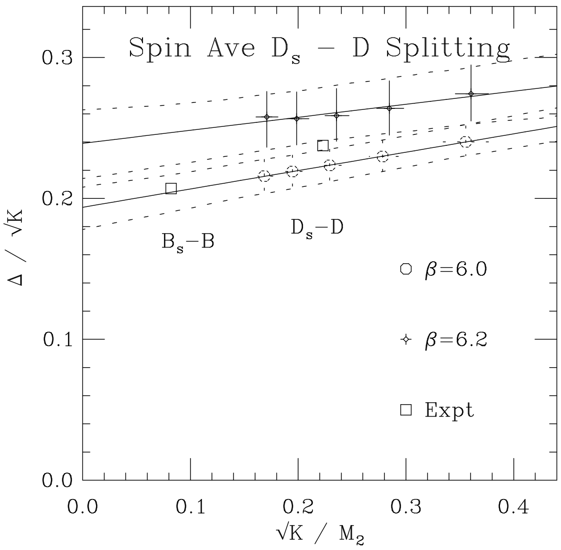

Figure 4.5: D S-P splitting

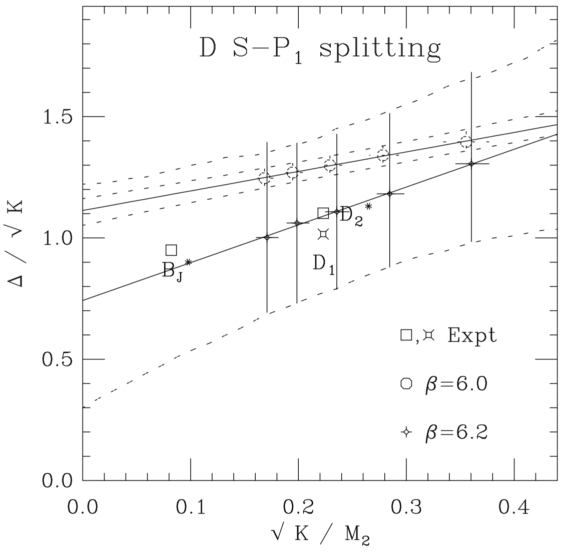

Figure 4.6: D_s S-P splitting

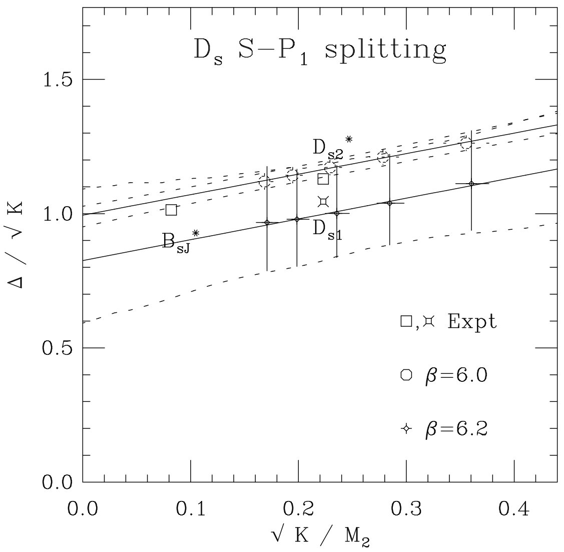

scaling and consistency with experiment are not remarkable results, nevertheless it is worth presenting these plots in Figure 4.5 and Figure 4.6 since there are no competing relativistic calculations of heavy-light p-states, and the NRQCD calculations referred to in Chapter 3 are on single lattices preventing continuum scaling analysis.

The numerical results for the heavy-light spectrum obtained at $\beta = 6.2$ are presented in Table 4.1. Since the string tension and quarkonium S-P splitting data are calculated using different configurations from this heavy-light calculation, the results incorporate an estimate of the error due to these scales, rather than being bootstrapped with the quantity used to set the scale.

Table 4.1: Heavy-light spectrum at $\beta = 6.2$

Splitting (MeV)	$\sqrt{K}$	M_ρ	$Q\bar{Q}$ S-P Splitting	Experiment
$D^* - D$	109(10)	99(10)	104(12)	142
$D_s^* - D_s$	99(7)	91(7)	95(8)	144
$\bar{D}_s\bar{D}$	114(8)	109(8)	112(9)	105
$D_1\bar{D}$	480(140)	450(140)	465(140)	459
$D_{s1}\bar{D}_s$	440(80)	415(70)	430(80)	460
$B^* - B$	40(14)	37(14)	43(14)	46
$B_s^* - B_s$	41(9)	38(9)	44(10)	47
$\bar{B}_s\bar{B}$	108(9)	103(9)	113(11)	91
$B_1\bar{B}$	390(180)	370(170)	400(180)	419
$B_{s1}\bar{B}_s$	390(100)	370(90)	410(100)	446

4.4 Heavy-Heavy Meson Analysis

The quarkonium hyperfine splitting scales with the string tension within statistical error between the two calculations, Figure 4.7, and is very much lower than experiment, demonstrating that, as anticipated, the quenched hyperfine splitting is smaller than experiment.

The quarkonium S-P splitting, again scaled using the string tension, is plotted in Figure 4.8. The error on this splitting is rather large in the $\beta = 6.2$ calculation due to the use of local correlation functions, which only form a plateau at relatively large times. The splitting in the $\beta = 6.2$ calculation is in agreement with experiment, while the $\beta = 6.0$ calculation is not. The two calculations are only in marginal agreement with each other, suggestive of discretisation effects.

Preliminary results from the Fermilab research group [57, 58], simulated using a fixed (i.e. β independent) tadpole improved clover coefficient of $C_{SW} = 1.4$, are also suggestive of a change, again with marginal statistics, Figure 4.9.

Figure 4.7: Quarkonium hyperfine splitting

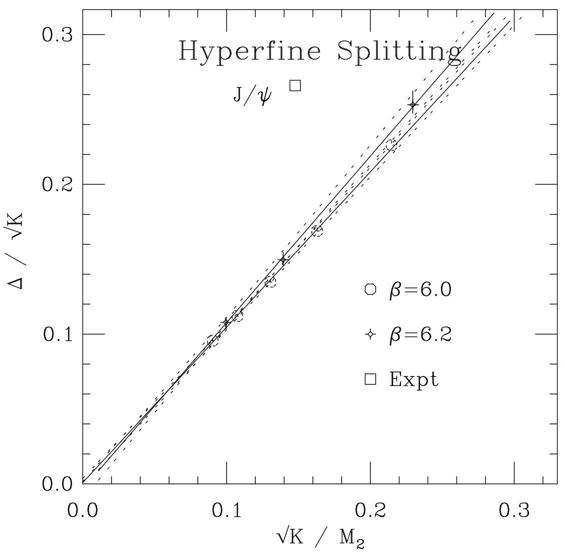

The numerical quarkonium results obtained from the $\beta = 6.2$ calculation are presented in Table 4.2.

4.5 Scaling Behaviour

With only two calculations, an extrapolation to the continuum using a linear model is not possible, and so we plot the lattice spacing dependence without performing a fit.

Figure 4.8: Quarkonium S-P splitting

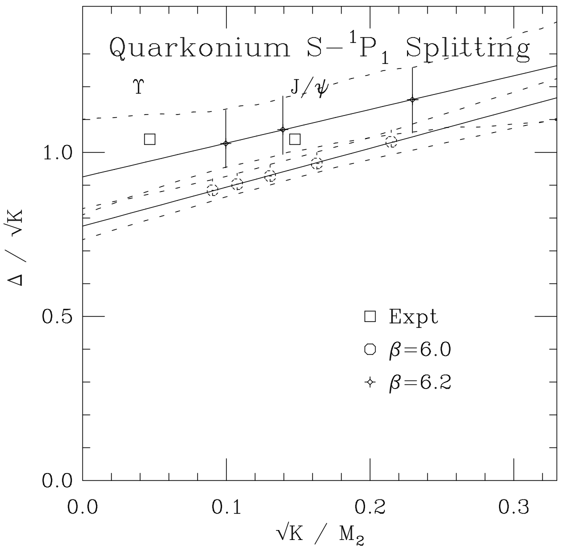

Figure 4.9: Preliminary Fermilab tadpole improved quarkonium S-P splitting

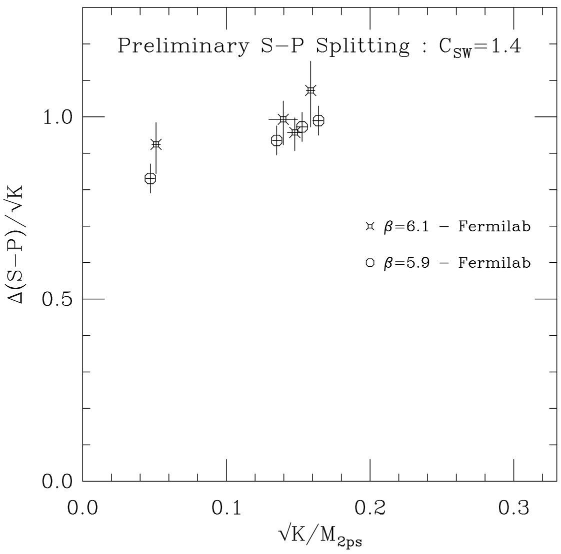

Table 4.2: $\beta = 6.2$ heavy-heavy mass splittings

Splitting (MeV)	$\sqrt{K}$	M_ρ	$Q\bar{Q}$ S-P Splitting	Experiment
$J/\psi - \eta_c$	72(3)	66(3)	69(5)	117
$^1P_1 - \bar{S}$	474(35)	450(35)	-	458
$\Upsilon - \eta_b$	22(3)	20(3)	24(5)	40
$^1P_1 - \bar{S}$	430(50)	410(50)	-	460

4.5.1 Hyperfine Splittings

The scaling behaviour of the J/ψ hyperfine splitting is shown in Figure 4.10, and can be seen to be near scaling with both the string tension and M_ρ scales, in clear disagreement with experiment, showing that the quenched approximation is incorrect. The charmonium hyperfine results are consistent with those of the El-Khadra et al [27].

Similarly the results extrapolated to Υ, Figure 4.10 are in clear disagreement with the potential model estimate of around 40 MeV.

The results normalised to the quarkonium S-P splitting do not scale, at around the 1 σ level. The calculation of the $S - P$ splitting at $\beta = 6.2$ is subject to large statistical errors, so that further work is required to clarify whether this is a discretisation or a purely statistical effect.

Future improved calculations should produce a result for the hyperfine splitting which scales using the quarkonium S-P splitting to set the lattice spacing. This will probably not agree with those using the low momentum observables since NRQCD calculations, which are not subject to large discretisation effects for heavy quarks, produce a result [50] for the S-P splitting in units of M_ρ which scales and is 30% lower than experiment, so that this would induce an inconsistency between the quarkonium hyperfine splitting scaled with each of these quantities. Any mass dependence of the quenched continuum S-P splitting will, of course, mean that the level of discrepancy between the lattice spacing definitions will differ in the J/ψ and Υ systems.

For comparison we can estimate the value NRQCD calculations of the hyperfine splitting would yield using M_ρ to set the scale by assuming $\Delta_{\text{hyperfine}} \propto \frac{1}{M_Q}$; feeding the change in scale into both the selected quark mass and the splitting then yields a 40-50% reduction in the hyperfine splitting. The NRQCD quenched continuum result appears to be around 35 MeV [50] using the S-P splitting to set the scale, with a 30% uncertainty due to u_0 ambiguities and higher order relativistic corrections. This gives an estimate for the central value of around 17-21 MeV if M_ρ were used to set the scale.

Figure 4.10: Scaling behaviour of J/ψ and Υ hyperfine splitting

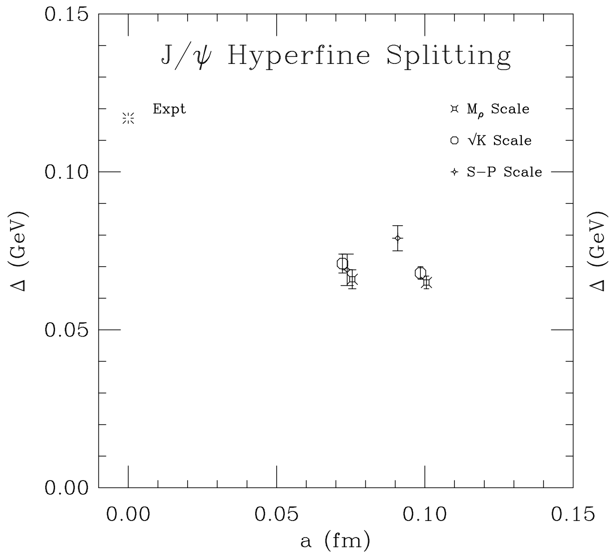

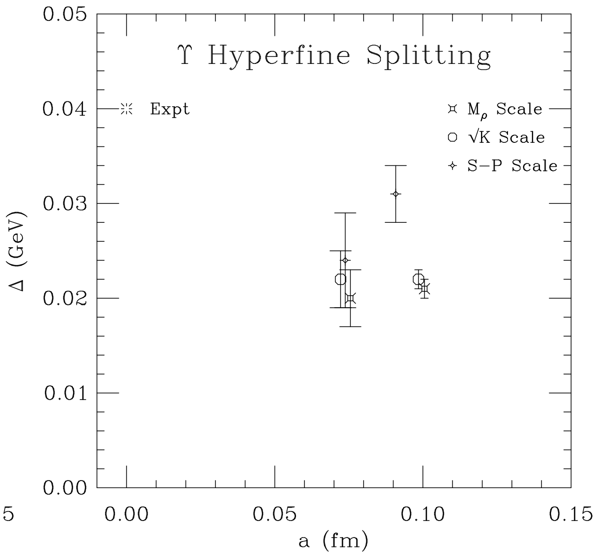

The results for the D and D_s hyperfine splittings are scaling well, significantly below experiment, c.f. Figure 4.11. Extrapolating the heavy-light hyperfine splittings to the B and B_s systems, however, introduces a much greater percentage statistical error, so that the results are both consistent with experiment and with a large quenching effect, as shown in Figure 4.12, so that no conclusion can be drawn.

These results can be compared with preliminary extrapolations generously made

Figure 4.11: Scaling behaviour of D and D_s hyperfine splittings

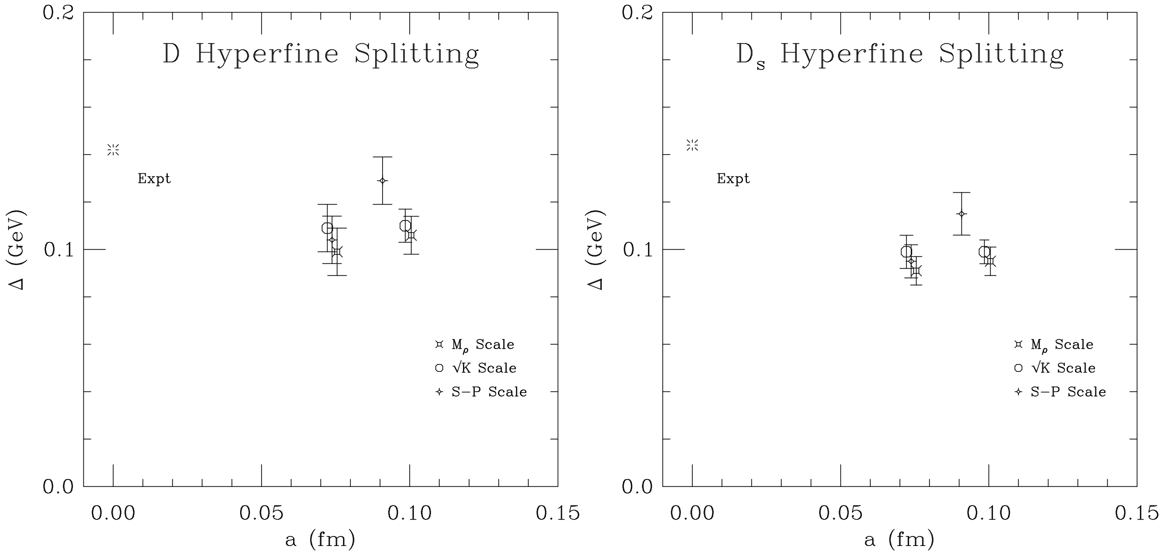

Figure 4.12: Scaling behaviour of B and B_s hyperfine splittings

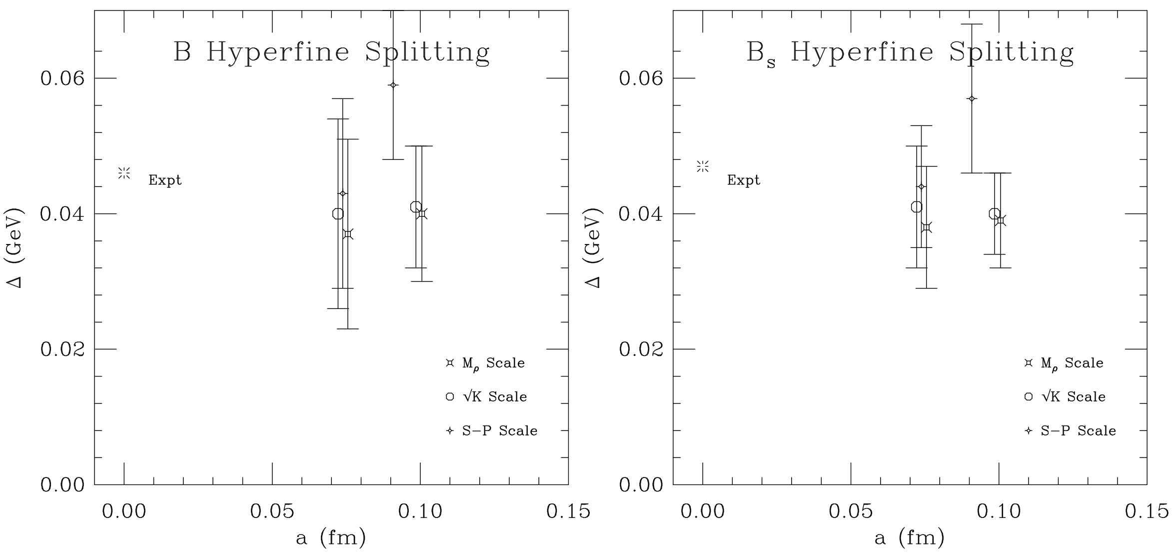

available by the Fermilab research group [57, 58] in Figure 4.13 and Figure 4.14. These calculations were performed at $\beta = 5.5, 5.7, 5.9$ and 6.1 using the tadpole improved clover action and the scale was set using the quarkonium S-P splitting. The fits did not include the points from coarsest lattice, $\beta = 5.5$, and the analysis at $\beta = 6.1$ which is not considered complete.

Figure 4.13: Fermilab preliminary D_s hyperfine splitting

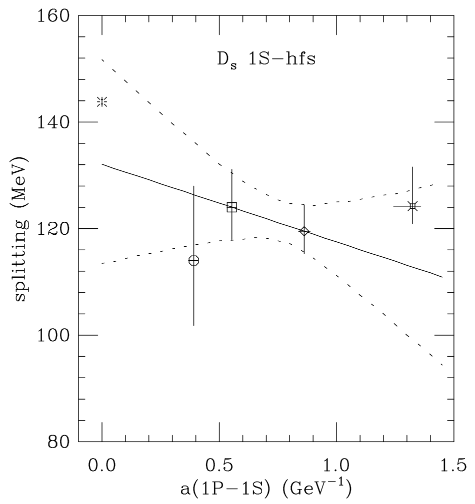

4.5.2 Spin Averaged Q_s - Q_l Splittings

Figure 4.15 shows the scaling behaviour of the spin averaged $\bar{D}_s - \bar{D}$ and $\bar{B}_s - \bar{B}$ splittings respectively, having fixed κ_{strange} from the kaon mass. These are consistent with experiment at the 1 σ level, however it is difficult to conclude anything about the lattice spacing dependence.

4.5.3 S-P Splittings

The scaling behaviour of the Quarkonium S-P splittings with light hadron observables are shown in Figure 4.16 for the $c\bar{c}$ and $b\bar{b}$ systems. The central values of these plots scale poorly, causing the odd looking continuum behaviour of data

Figure 4.14: Fermilab preliminary B_s hyperfine splitting

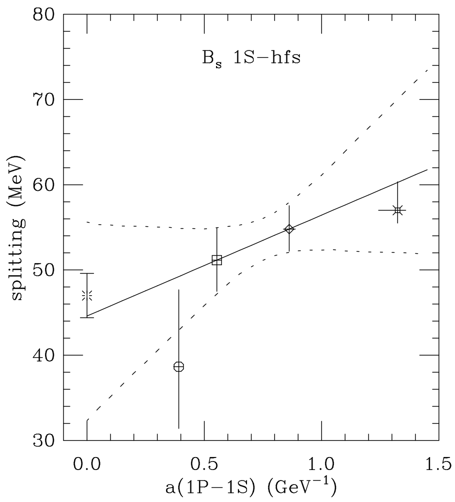

Figure 4.15: Scaling behaviour of $\bar{D}_s - \bar{D}$ and $\bar{B}_s - \bar{B}$ spin averaged splittings

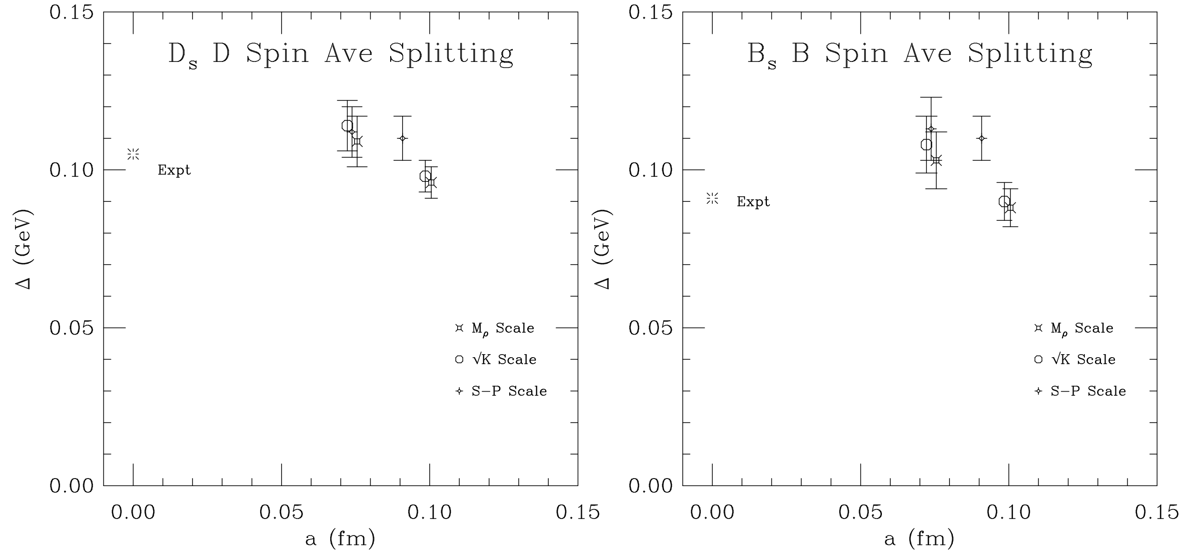

scaled with the S-P splitting in the previous graphs. The statistical error on the points is large, however, and without an improved analysis at $\beta = 6.2$, or perhaps even higher, the question of whether the source of this effect is statistical, discretisation, or quenching cannot be addressed.

Figure 4.16: Scaling behaviour of J/ψ and Υ S-P splittings

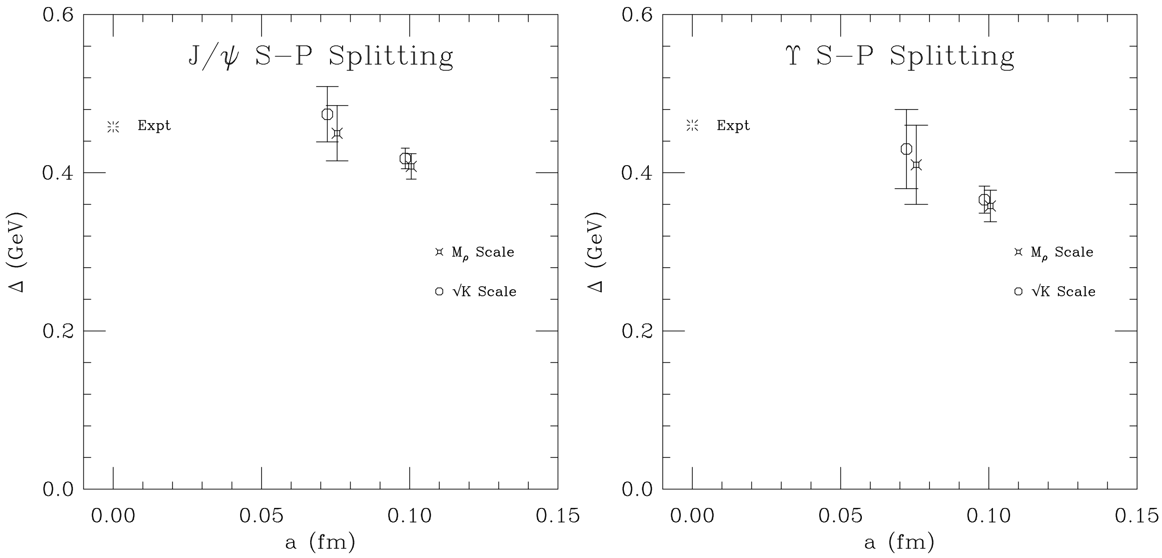

The quenched NRQCD splitting [50] scales well with M_ρ, but is about 30% lower than experiment, significantly lower than the values obtained in the two calculations in this thesis.

The heavy-light S-P splittings, Figures 4.17, and 4.18, are broadly consistent with experiment, apart from the chirally extrapolated points in the $\beta = 6.0$ calculation, which were not considered particularly trustworthy, as discussed in Section 3.8.

Figure 4.17: Scaling behaviour of $D_1 - \bar{D}$ and $D_{s1} - \bar{D}_s$ S-P splittings

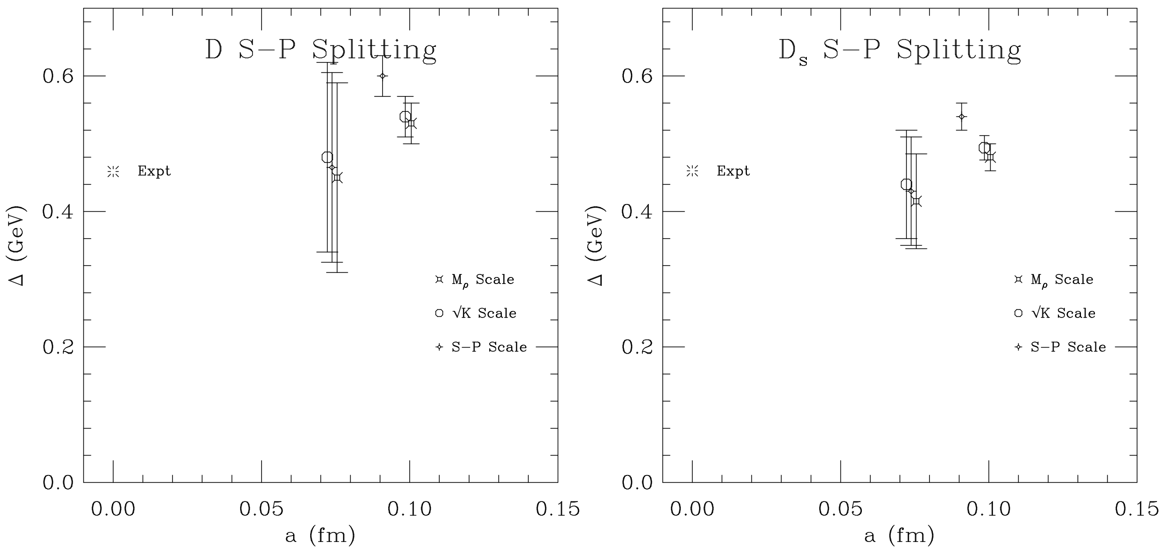

Figure 4.18: Scaling behaviour of $B_1 - \bar{B}$ and $B_{s1} - \bar{B}_s$ S-P splittings

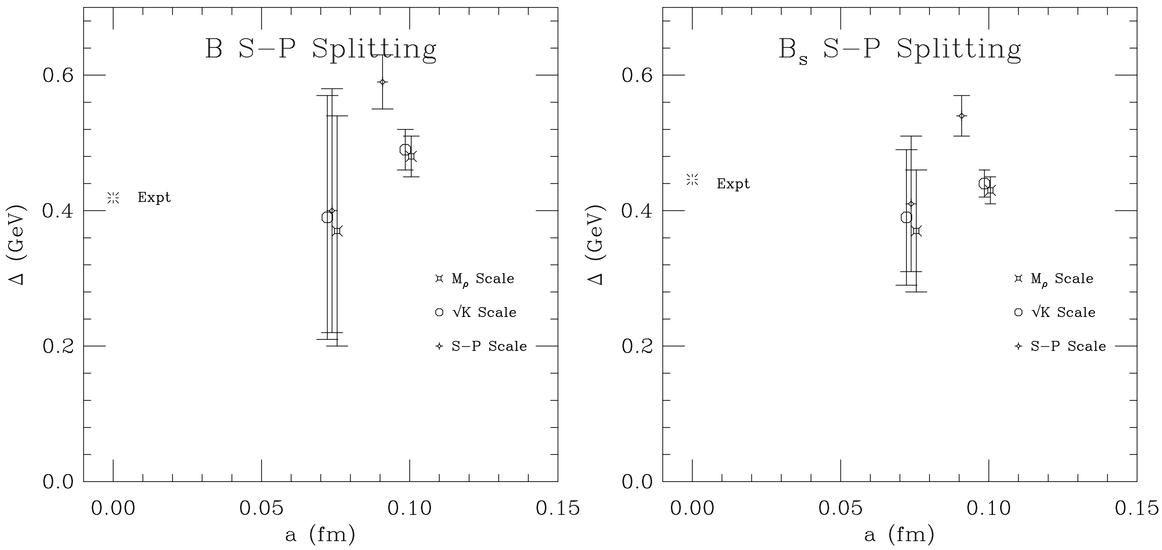

4.6 Conclusions

The quenched hyperfine splittings in both heavy-light and quarkonium systems are approximately scaling with both the string tension and with M_ρ, and are in clear disagreement with experiment in all but the B system, where the statistical error after extrapolation is too great to draw conclusions. If we assume scaling behaviour of the data, and take a weighted average of the values obtained with the string tension scale we produce the results in Table 4.3.

We have presented the first relativistic lattice results for the heavy-light S-P splittings, and find that the calculations of the S-P splittings in both heavy-light systems and quarkonia are within one or two sigma of experiment, apart from the calculation of the Υ S-P splitting at $\beta = 6.0$. Improved statistical errors for a high β quenched quarkonium calculation are required in order to resolve whether this is a quenching or discretisation effect, and would be of great interest since this splitting is commonly used to set the scale, and has been shown to have the incorrect quark mass dependence in the quenched approximation by NRQCD calculations.

In today's context of exploratory dynamical quark simulations, the quarkonium hyperfine splitting is extremely interesting as an observable that has been demonstrated to be incorrect in the quenched approximation, and would be an ideal candidate for a hadronic observable that should demonstrate a sea quark mass dependence.

Table 4.3: Estimates for continuum quenched hyperfine splittings

Splitting	Calculation (MeV)	Experiment (MeV)
$D^* - D$	110 (6)	142
$D_s^* - D_s$	99 (4)	144
$B^* - B$	41 (8)	46
$B_s^* - B_s$	40 (5)	47
$J/\psi - \eta_c$	69 (2)	117
$\Upsilon - \eta_b$	22 (1)	-

Chapter 5

Novel Gauge-Invariant Smearing Technique

5.1 Motivation

In this section we motivate a novel smearing technique with intuition based upon a colour singlet potential model. Following the analysis of Appendix C, we suppose there exists non-relativistic wavefunctions, $\psi_n(\vec{x})$, for the physical states in the QCD colour singlet potential. With a smearing function

$$S_n(\vec{x},0) \equiv S_n(\vec{x}) \sum_{i,j,k} \delta^3(\vec{x} - i\hat{x} - j\hat{y} - k\hat{z}) \tag{5.1}$$

we obtain the overlap of the smearing function with the physical wave functions as

$$C_{nm} = \int_{\mathbb{R}^3} \psi_m^*(\vec{x}) S_n(\vec{x},0) d^3x = \sum_{i,j,k} \psi_m^*(i\hat{x} + j\hat{y} + k\hat{z}) S_n(i\hat{x} + j\hat{y} + k\hat{z}). \tag{5.2}$$

If we choose a non-space-filling smearing function of the form

$$S_n(\vec{x},0) \equiv \sum_{r=0}^{N} r^2 \phi_n(r) \sum_{\hat{\mu}=\hat{x},\hat{y},\hat{z}} \Big(\delta^3(\vec{x} - r\hat{\mu}) + \delta^3(\vec{x} + r\hat{\mu}) \Big) \tag{5.3}$$

where ϕ_n is some arbitrary modulating function that is chosen to approximate the true solution ψ_n, and the factor r^2 compensates for the non-space-filling nature of the smearing, then the overlap is

$$C_{nm} = \int_{\mathbb{R}^3} \psi_m^*(\vec{x}) S_n(\vec{x},0) dV \tag{5.4}$$

$$= \sum_{r=0}^{N} r^2 \phi_n(r) \psi_m^*(r) \tag{5.5}$$

$$\overset{a\to 0}{\to} \int_{r=0}^{\infty} r^2 \psi_m^* \phi_n dr \tag{5.6}$$

$$\simeq \delta_{nm}. \tag{5.7}$$

Thus if we choose the ϕ_m correctly (i.e. to be ψ_n) then we establish the orthogonality relation required without the need for space filling. The new smearing technique proposed is a generalisation of the above form to incorporate colour:

$$\psi(x) \to \sum_{r=0}^{N} (r+\tfrac{1}{2})^2 \phi_n(r) \sum_{i=x,y,z} \left\{ \left[\prod_{n=1}^{r} U_i(x+(n-1)\hat{i}) \right] \psi(x+r\hat{i}) + \left[\prod_{n=1}^{r} U_i^\dagger(x-n\hat{i}) \right] \psi(x-r\hat{i}) \right\} \tag{5.8}$$

where the links are fuzzed links, c.f. Section 1.13.2. This procedure is very similar in cost to fuzzing with a radius N, since all the terms can be formed as part of the process of fuzzing to the largest radius. The technique therefore eliminates the two main problems with implementing gauge-invariant multi-state smearing, namely that gauge invariance requires expensive iterative space filling techniques, and that it restricts the functional form. Here we have a low-cost gauge invariant technique with an arbitrary functional form, allowing the insertion of both ground and radially excited wavefunctions.

We now consider the case when the physical solutions are approximately hydrogenic wavefunctions.

5.2 Optimising the Smearing

Suppose the physical wave functions are well described by the hydrogenic wavefunctions, ψ_n , with some Bohr radius, r_1. We wish to approximate these solutions with a trial wavefunction, which we choose to be the hydrogenic solutions ϕ_m with Bohr radius r_2. Consider the overlap of the trial excited state with the physical groundstate,

$$C_{10} = \int r^2 \psi_0 \phi_1 dr \tag{5.9}$$

$$\begin{aligned}
&\propto \int r^2(1-\frac{r}{2r_2})e^{-\frac{r}{2r_2}}e^{-\frac{r}{r_1}}dr && (5.10)\\
&= \int r^2 e^{-\frac{r}{c}}dr - \int \frac{r^3}{2r_2}e^{-\frac{r}{c}} && (5.11)\\
&= c^3\left[\Gamma(3) - \frac{c}{2r_2}\Gamma(4)\right] && (5.12)\\
&\simeq 2c^3\frac{\delta}{r_2} && (5.13)
\end{aligned}$$

where $c = \frac{2r_1r_2}{r_1+2r_2}$, $\delta = r_2 - r_1$, and the last step is made for small δ. Thus the overlap of the excited state smearing with the physical state is proportional to the error in the Bohr radius. The overlap is positive for smearing radii that are too large, and negative for radii that are too small, and, recalling Section 1.13, the effective mass of the smeared - local correlation function will have a vertical asymptote for radii that are too small, and a smooth form for radii that are too large. This dramatic change of behaviour may be used to tune the Bohr radius on very small statistical samples.

Arguments involving the limiting cases of very large and very small smearing radii may be used to convince onself that for reasonable physical (but not necessarily hydrogenic) ground states, the same transition must occur between the two limits, making it possible to orthogonalise the radially excited smearing with respect to the physical groundstate by tuning the Bohr radius parameter. This gives a very simple way to define and measure the smearing radius in a simulation.

Since the physical wavefunctions (only well defined in non-relativistic systems) are not hydrogenic in form, one choice for the radius will not, in general, simultaneously minimise the overlaps C_{10} and C_{01}. The better the ansatz for the smearing functions, the closer together we expect the optimal radii for the groundstate and excited state correlators to lie. Where the ansatz is better we also expect there to be less contamination from the higher excited states, since the physical wavefunctions are all mutually orthogonal.

In order to demonstrate the applicability of this smearing technique, a feasibility study was carried out on a small sample, with a large number of smearing radii, in the light-light, heavy-light and heavy-heavy sectors.

5.3 Feasibility Study

In this section we use the notation R_{nl} to denote smearing with the corresponding hydrogenic wavefunction with some Bohr radius. Fourteen quenched configurations of a $24^3 \times 48$ lattice at $\beta = 6.2$ were used with non-perturbatively $O(a)$ improved quarks (i.e. $C_{sw} = 1.61377$). Kappa values 0.13460 and 0.12300 were used, corresponding to quarks near the strange and charm masses respectively. The lighter quark propagators had local sources, and both local and R_{10} sources were generated for the heavy propagator with Bohr radii of 2.4, 2.5, 2.6, 2.75, 2.8, 2.9, 3.0, 3.1, 3.25, 4.0, and 5.5 in lattice units. This allowed the smearing combinations in Table 5.1 to be generated for each Bohr radius. The correlation functions were analysed using uncorrelated fits, because the small statistical sample caused the correlation matrix to be too noisy for reliable inversion in correlated fits.

Of primary interest is the two exponential row fit to the R_{10} and R_{20} smearing functions. A representative subset of the fitted effective masses at each Bohr radius for the heavy-heavy, heavy-light and light-light sectors are given in Figures 5.1 through 5.6.

The effective mass for the radially excited smearing demonstrates the expected transition in behaviour, and appears to be forming a plateau for $r_0 = 2.6(3.0, 3.1)$ in the heavy-heavy (heavy-light, light-light) sector. While the formation of an excited state plateau is clearly strongly dependent on the selection of r_0 to within about 0.1 (this is possible to do using only one configuration by looking for a pole in the effective mass plot), we do not wish that the fitted values be dependent on the smearing. To investigate this we study the stability of the fitted masses with the input parameters to the fitting procedure, namely the Bohr radius, and the timeslice range of the fit.

Table 5.1: Smearing combinations

κ_1	Source	Sink	κ_2	Source	Sink
2300	L	L	2300	L	L
2300	L	F	2300	L	L
2300	R_{10}	L	2300	L	L
2300	R_{10}	L	2300	R_{10}	L
2300	R_{10}	R_{10}	2300	L	L
2300	L	R_{20}	2300	L	L
2300	R_{10}	R_{20}	2300	R_{10}	L
2300	L	L	3460	L	L
2300	L	F	3460	L	L
2300	R_{10}	L	3460	L	L
2300	R_{10}	R_{10}	3460	L	L
2300	L	R_{10}	3460	L	L
2300	L	R_{20}	3460	L	L
3460	L	L	3460	L	L
3460	L	F	3460	L	L
3460	L	R_{20}	3460	L	L
3460	L	R_{10}	3460	L	L
3460	L	R_{10}	3460	L	R_{10}

Figure 5.1: Heavy heavy pseudoscalar fits, $r_0 = 2.4, 2.5, 2.6$: R_{20} (circles) and R_{10} (fancy squares) smearings

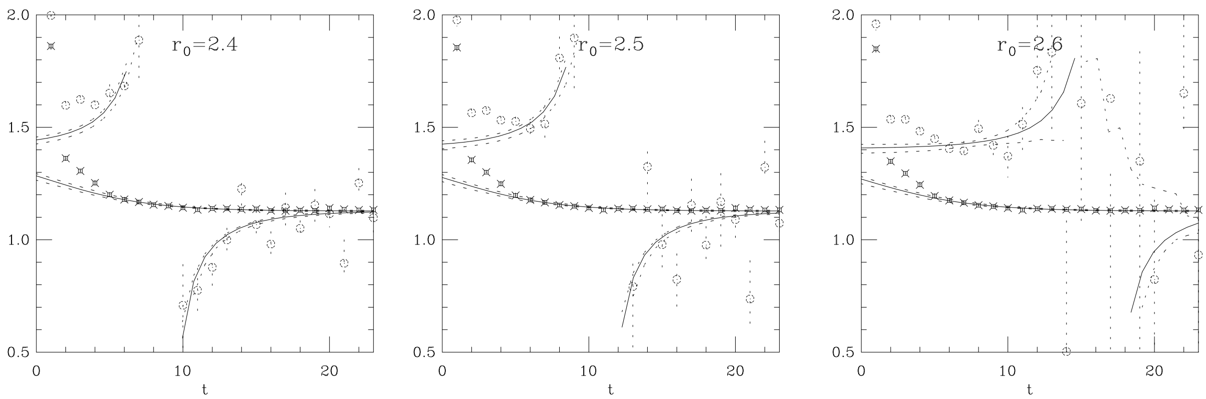

Figure 5.2: Heavy heavy pseudoscalar fits $r_0 = 2.75, 3.0, 5.5$

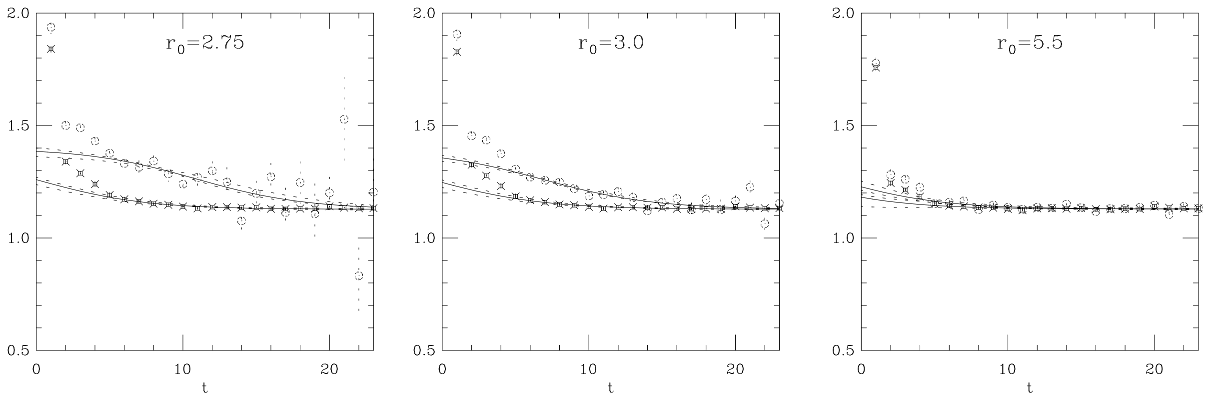

Figure 5.3: Heavy light pseudoscalar fits, $r_0 = 2.6, 2.8, 2.9$

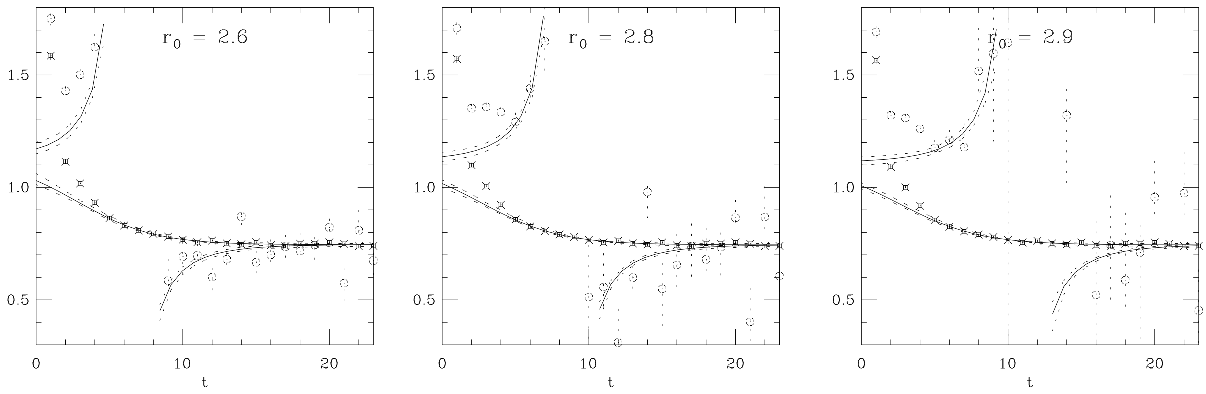

Figure 5.4: Heavy light pseudoscalar fits $r_0 = 3.0, 3.1, 4.0$

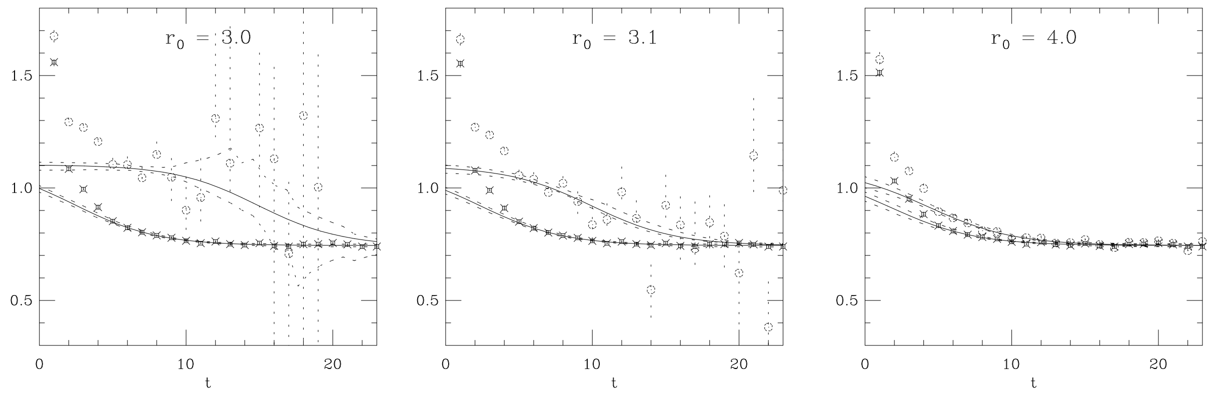

Figure 5.5: Light light pseudoscalar fits, $r_0 = 2.8, 2.9, 3.0$

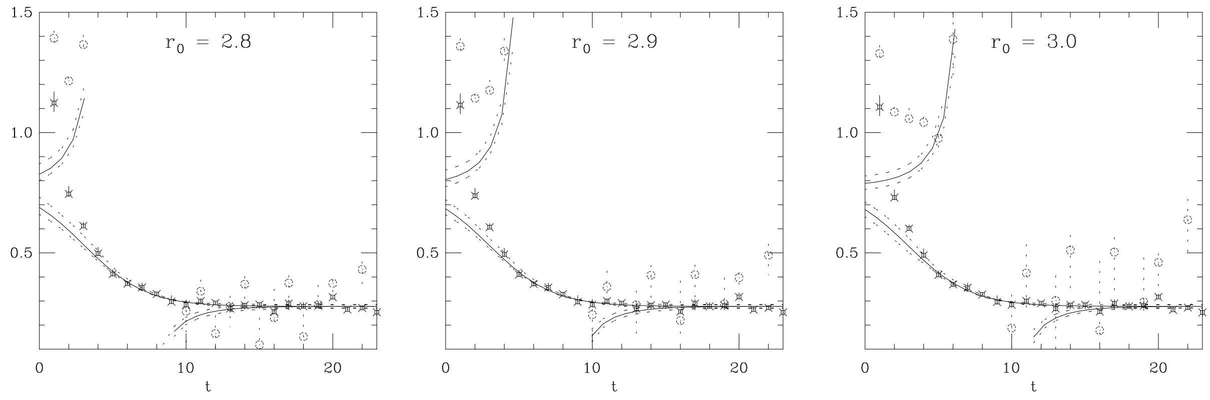

Figure 5.6: Light light pseudoscalar fits $r_0 = 3.1, 3.25, 4.0$

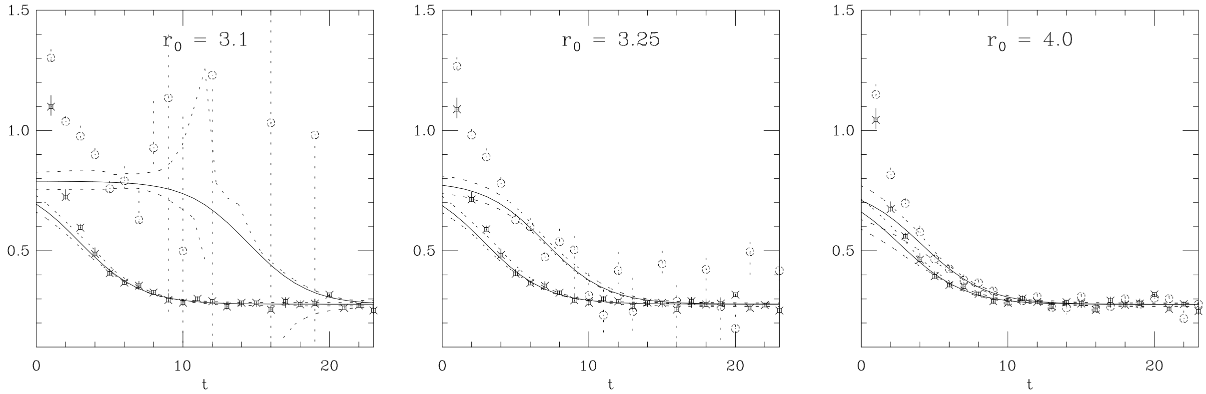

5.3.1 Stability Analysis of Fitted Masses

The fitted values for the two masses are given in Table 5.2 to Table 5.5, and are found to be remarkably stable in the fit range typically agreeing within statistical error for all values of $t_{min} \geq 3$.

Table 5.2: Heavy heavy double exponential fit stability; $r_0 = 2.6$, $T_{max} = 20$

tmin	χ^2/dof	χ^2	Pseudo	Pseudo$'$
2	0.66	21.	1.123(3)	1.45(2)
3	0.25	7.5	1.125(4)	1.42(1)
4	0.13	3.7	1.127(4)	1.41(2)
5	0.13	3.3	1.128(4)	1.40(3)
6	0.13	3.2	1.129(4)	1.40(3)
7	0.14	3.1	1.130(5)	1.40(4)

The level of statistical error on the excited state mass is also particularly pleasing; compare Table 5.5 with Table 3.7. The error on the excited light-light state is typically between 5 and 10 times larger than that on the ground state, while in the fuzzed calculations of Chapter 3 the ratio is between 50 and 100, and the fit is not stable. The direct comparison of the errors is not particularly meaningful since

Table 5.3: Heavy heavy triple exponential fit stability; $r_0 = 2.6$, $T_{max} = 20$

tmin	χ^2/dof	χ^2	Pseudo (2300,2300)	Pseudo$'$	Pseudo$''$
2	0.081	3.6	1.128(4)	1.39(3)	2.13(4)
3	0.083	3.5	1.129(5)	1.39(3)	2.10(10)
4	0.086	3.3	1.130(6)	1.39(4)	1.9(2)
5	0.089	3.2	1.130(5)	1.40(7)	1.9(2)
6	0.095	3.1	1.131(6)	1.39(8)	1.8(2)

Table 5.4: Heavy light double exponential fit stability; $r_0 = 3.0$, $T_{max} = 20$

tmin	χ^2/dof	χ^2	Pseudo	Pseudo$'$
2	0.44	14.	0.746(5)	1.18(2)
3	0.15	4.5	0.745(6)	1.13(2)
4	0.074	2.1	0.744(6)	1.10(2)
5	0.076	2.0	0.744(7)	1.09(3)
6	0.078	1.9	0.744(7)	1.08(4)
7	0.083	1.8	0.744(7)	1.07(6)

Table 5.5: Light light double exponential fit stability; $r_0 = 3.1$, $T_{max} = 18$

tmin	χ^2/dof	χ^2	Pseudo	Pseudo$'$
2	0.18	5.0	0.280(7)	0.86(4)
3	0.085	2.2	0.279(7)	0.81(3)
4	0.079	1.9	0.278(7)	0.79(4)
5	0.082	1.8	0.278(7)	0.81(6)

the fits here are on a different lattice with a different number of configurations and uses an uncorrelated fit, while only sink smearing was employed for the R_{20} correlator in all systems and for both the R_{10} and R_{20} channel in the light-light mesons.

Table 5.6: Heavy heavy double exponential fit stability with Bohr radius

Bohr	tmin	χ^2/dof	χ^2	Pseudo	Pseudo ′
2.60	4	0.13	3.7	1.127(4)	1.41(2)
2.75	4	0.083	2.3	1.128(4)	1.40(2)
2.80	4	0.066	1.9	1.128(4)	1.40(2)
2.90	4	0.045	1.2	1.128(4)	1.39(2)
3.00	4	0.033	0.92	1.128(4)	1.39(2)
3.10	4	0.026	0.74	1.128(4)	1.39(1)
3.25	4	0.021	0.59	1.128(4)	1.39(1)
4.00	4	0.016	0.44	1.128(3)	1.39(1)
5.50	4	0.016	0.44	1.129(3)	1.40(6)

Table 5.7: Heavy light double exponential fit stability with Bohr radius

Bohr	tmin	χ^2/dof	χ^2	Pseudo	Pseudo ′
2.60	4	0.059	1.6	0.745(6)	1.13(3)
2.75	4	0.10	2.8	0.745(6)	1.12(2)
2.80	4	0.12	3.2	0.745(6)	1.12(2)
2.90	4	0.12	3.3	0.744(6)	1.11(2)
3.00	4	0.074	2.1	0.744(6)	1.10(2)
3.10	4	0.045	1.2	0.744(6)	1.10(2)
3.25	4	0.026	0.72	0.744(6)	1.09(2)
4.00	4	0.013	0.35	0.744(6)	1.09(3)
5.50	4	0.014	0.38	0.745(6)	1.10(5)

In order to study the stability of the fits with respect to the chosen Bohr radius, I tabulate the fitted mass values corresponding to $t_{min} = 4$ for all the simulated Bohr radii in Table 5.6, Table 5.7, and Table 5.8. They are stable within the statistical error over almost the entire range of radii simulated, however it is

Table 5.8: Light light double exponential fit stability with Bohr radius

Bohr	tmin	χ^2/dof	χ^2	Pseudo	Pseudo ′
2.60	4	0.0053	0.13	0.278(7)	0.79(4)
2.75	4	0.010	0.24	0.278(7)	0.78(4)
2.80	4	0.013	0.32	0.278(7)	0.78(4)
2.90	4	0.029	0.70	0.278(7)	0.78(4)
3.00	4	0.077	1.9	0.278(7)	0.78(3)
3.10	4	0.079	1.9	0.278(7)	0.79(4)
3.25	4	0.023	0.55	0.278(7)	0.79(4)
4.00	4	0.0013	0.031	0.277(6)	0.77(7)
5.50	4	0.00072	0.017	0.277(6)	0.8(1)

worth fine tuning the radius since it is possible to do this cheaply and gives the satisfying effect of obtaining a plateau for the excited state.

5.4 Selecting the Bohr Radius

From inspection of the effective mass plots presented, we can see that the optimal values of the Bohr radius parameter (at least for the R_{20} correlator) were about 2.6 for the heavy-heavy state, 3.0 for the heavy-light and 3.1 for the light-light. Using the discussion in Section 5.2 we plot the fitted amplitudes of the local-smeared correlation functions versus Bohr radius, looking for the zero of the overlap of the R_{20} correlator with the groundstate.

Figure 5.7, Figure 5.8 and Figure 5.9 present the dependence of the four fitted amplitudes on the Bohr radius used. The linear fits are a good approximation, producing the following optimal values for the smearing radii given in Table 5.9

While the effective mass plots presented were on fourteen configurations, it is clear that following the pole on the plot gave very accurate optimisation of the Bohr radius, as demonstrated by later fits to the amplitudes. It was anticipated in Section 5.2 that the radius for minimal contamination of the groundstate with respect to the excited state would differ from the radii already presented, due to the non-hydrogenic form of the solutions of the QCD potential. This not ap-

Figure 5.7: Fitted amplitudes for quarkonia correlation functions

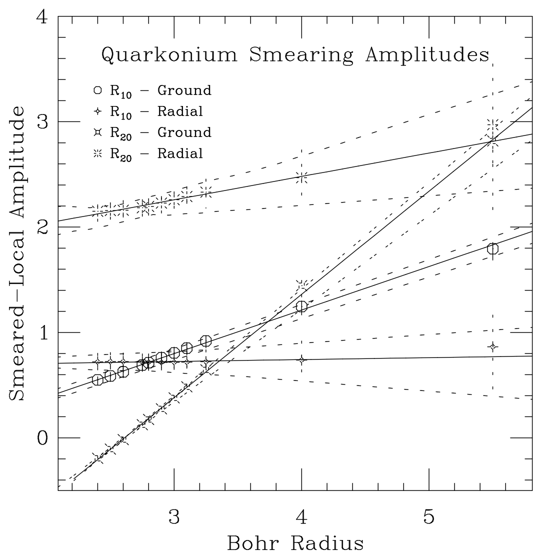

Figure 5.8: Fitted amplitudes for heavy-light correlation functions

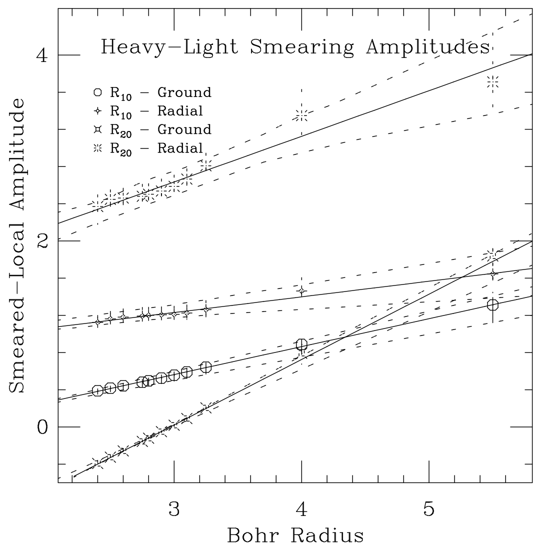

Figure 5.9: Fitted amplitudes for light-light correlation functions

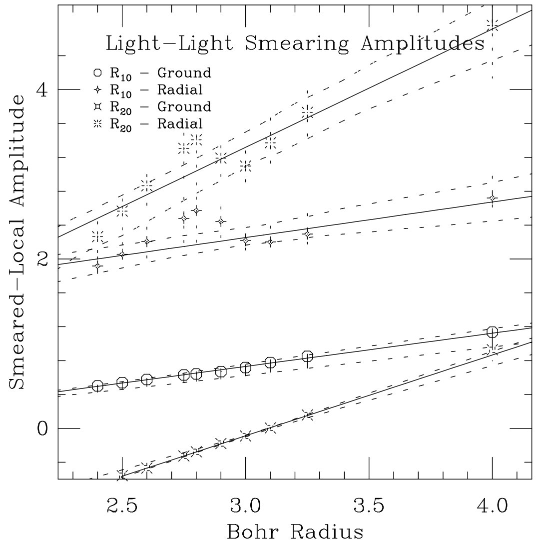

Table 5.9: Optimal Bohr radii

System	Fitted Value	Choice
2300-2300	2.62(2)	2.6
2300-3460	2.98(2)	3.0
3460-3460	3.09(1)	3.1

parent from the data presented above, where there is no minimum of the R_{10} - excited state amplitude. We must bear in mind however that the contamination of the R_{10} correlator is measured at early times, whereas the contamination of the R_{20} correlator is found from its asymptotic time dependence, leaving the determination of the optimal Bohr radius from the R_{10} correlator much more subject to contamination from higher excited states. For this reason, it is dangerous to look only at the local-smeared amplitude, since cancelling contributions from the higher states can cause a seemingly flat effective masses. Instead we study the smeared-smeared correlators, which have positive definite contaminating contributions, and minimise the amplitude for the contamination of the R_{10} - R_{10} correlator. These correlation functions were only generated for the heavy-heavy combination, and Figure 5.10 presents a sample fit to the pseudoscalar data.

Figure 5.10: R_{10} - R_{10} smeared quarkonium, $r_0 = 2.4, 3.0$

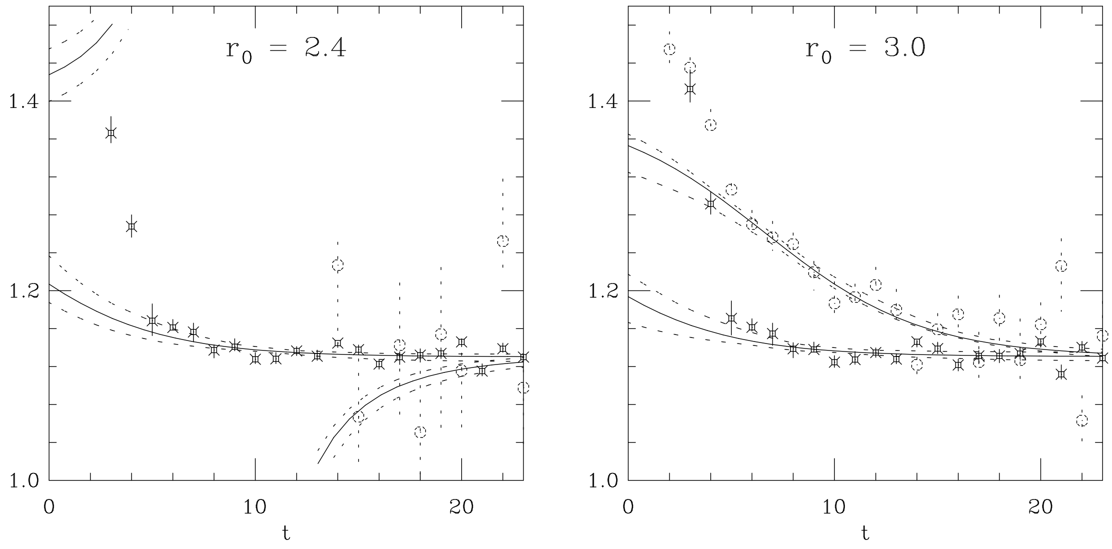

Here the contamination below timeslice 5 is apparent, as well as a weaker drift to the plateau beyond this point. It is this ultimate drift we must study. Figure 5.11 plots the fitted contaminating amplitude for this correlator versus radius; we ex-

Figure 5.11: R_{10} - R_{10} smeared quarkonium contaminating amplitude

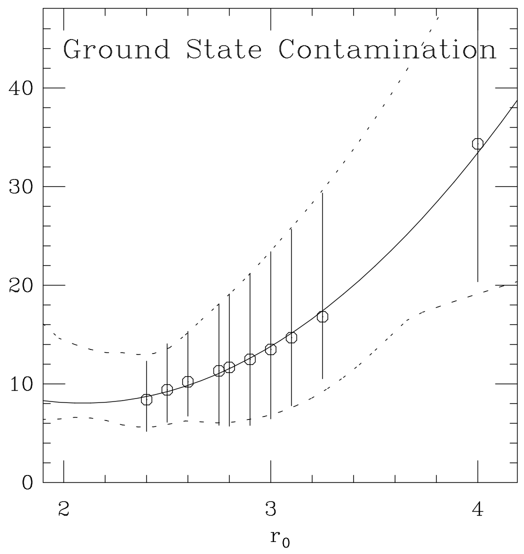

pect from Section 5.2 a quadratic dependence on the smeared-smeared correlator. We obtain a minimising radius of $r_0 = 2.1(4)$ with a quadratic fit.

5.5 Use of Doubly Smeared Correlation Functions

In this section I demonstrate that the signal obtained from doubly smeared correlators produces is useful. The double exponential fit to the double R_{10} and single R_{20} smeared correlation functions are presented in Figure 5.12 and Figure 5.13 for the heavy-heavy and light-light systems respectively.

Clearly this smearing combination, while not tailored for any particular state consitutes a valid signal that can be included in multi-channel multi-exponential fits, which is always of use, especially for the p-states.

Figure 5.12: Doubly smeared (fancy squares) heavy-heavy fit

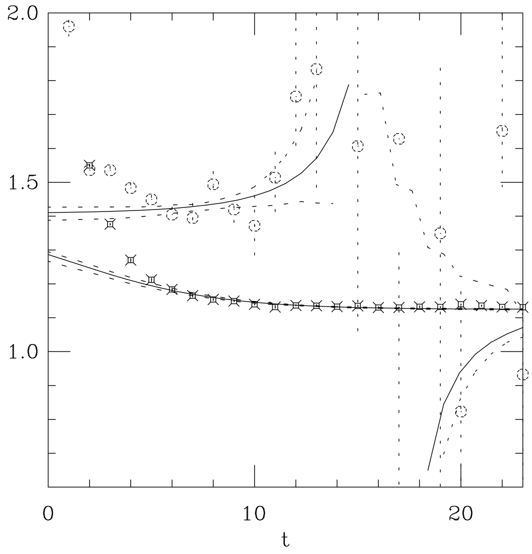

Figure 5.13: Doubly smeared (fancy squares) light-light fit

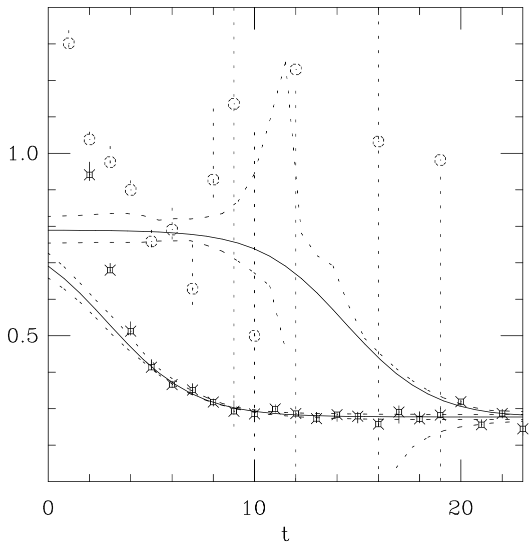

5.6 Comparison With Fuzzing

In order to fairly compare the level of statistical error with traditional techniques, I present double exponential fits to the R_{10} sink and the fuzzed sink, both with the optimal radius in Figure 5.14, Figure 5.15 and Figure 5.16 for the heavy-heavy, heavy-light and light-light systems respectively, on the same set of local source propagators.

Figure 5.14: Heavy-heavy fuzzed (r=6) and R_{10} comparison

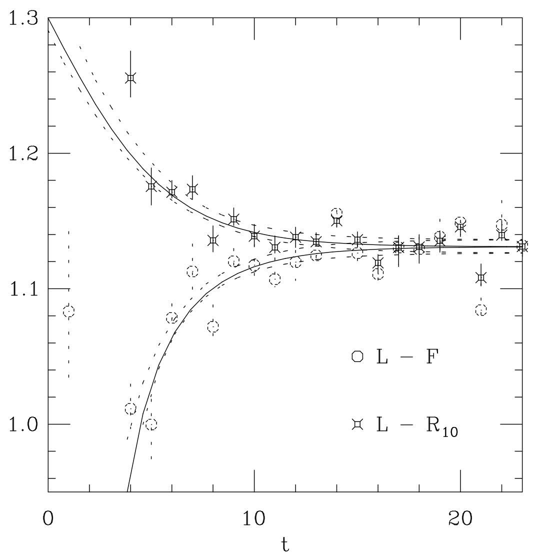

It can be seen that the statistical error from the R_{10} correlator is much reduced with respect to the fuzzed data. Admittedly the fuzzed data does appear to plateau earlier, with a caveat however; the noise on the fuzzed data is such that there is quite possibly a "double approach" to the plateau, due to contributions from more than one excited state, as seen in the large statistics fuzzed data at $\beta = 6.2$ in Figure 5.17, so that with higher statistics the plateau may well not survive. This was a surprise when performing high statistics calculations after the original fuzzing paper [25]. It has also been found that the fuzzed-

Figure 5.15: Heavy-light fuzzed (r=6) and R_{10} comparison

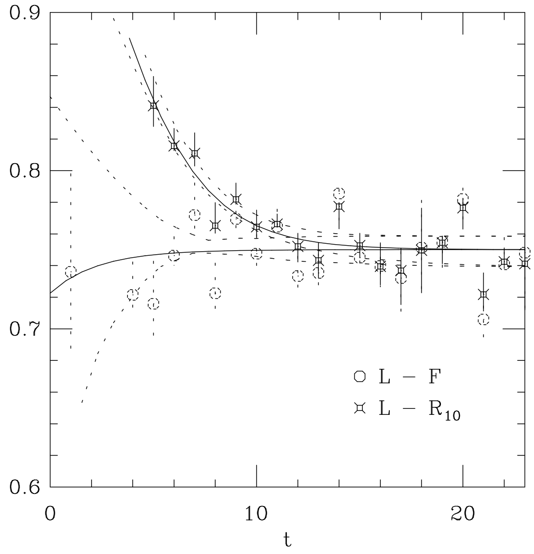

Figure 5.16: Light-light fuzzed (r=8) and R_{10} comparison

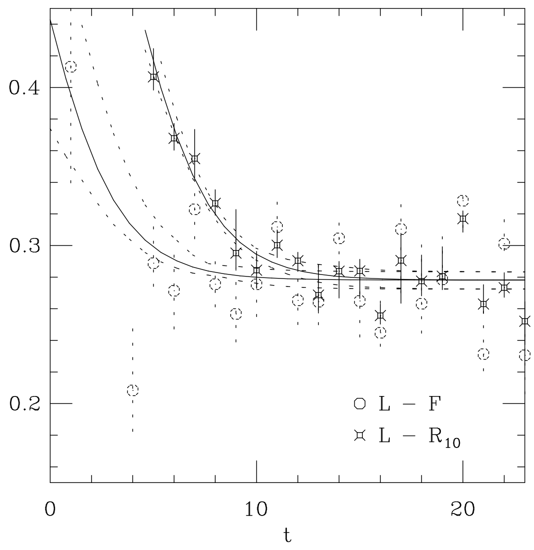

fuzzed combination tends to plateau after the fuzzed-local, indicating opposing contributions from excited states, and meaning that the plateau at early times is a misleading balance between contaminations of opposite sign (at least until after the fuzzed-fuzzed correlator has plateaued), c.f. Figure 5.17.

Figure 5.17: Approaches to fuzzed plateaux with high statistics

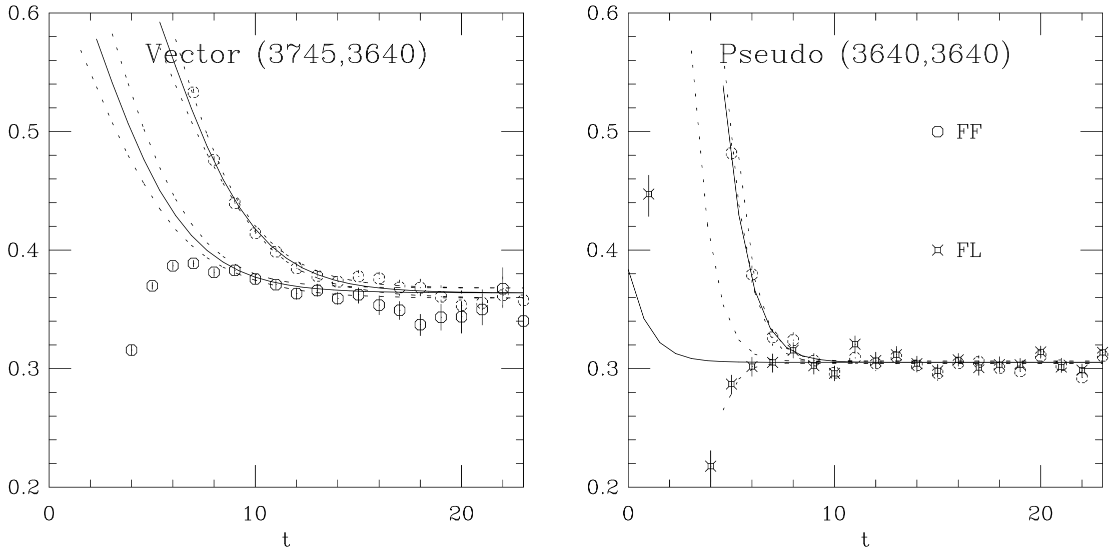

5.7 Conclusions

This smearing method provides, for the first time, a gauge invariant technique for inserting arbitrary radial wavefunctions in a smeared operator. So far results have only been presented using hydrogenic wavefunctions, though in principle any form could be used. Excellent stability of fits to both the ground and radially excited states was demonstrated, and the level of statistical error was significantly smaller than traditional techiques on the same ensemble. Tuning the radius of the wavefunctions allowed a clear plateau for the radially excited state to be isolated. An understanding of the dependence of the fitted amplitudes on the radius of the smearing was obtained, which can be used to determine more accurately the optimal radius.

The feasibility study did not include sufficient quark masses to extrapolate to the physical spectrum, however a rudimentary comparison of the splittings with experiment is made in Table 5.10, and can be seen to be plausible, though not exact. The main source of error in the light-light system is expected to be finite volume effects, since the Bohr radius required suggests the extent of the wave-function is significantly bigger than the lattice used. Secondly, quenching effects are to be expected since the mesons may reach the string breaking part of the potential.

Table 5.10: Comparison of 2S-1S splittings with experiment using string tension scale

System	Lattice (MeV)	Experimental (MeV)
Light Pseudoscalar	1370(50)	1170(100) (π)
Light Vector	1250(100)	700(25) (ρ)
Heavy-Light Pseudoscalar	970(60)	-
Heavy-Heavy Pseudoscalar	710(60)	590 (J/ψ)

Since the technique allows a free choice for the wavefunction it would be interesting to try to find a better basis than the hydrogenic wavefunctions. Harmonic oscillator wavefunctions have been tried and found to be inferior to hydrogenic. Other possible options are numerically solving the Cornell potential and inserting the solution as the smearing function, or alternatively measuring the wavefunction within a lattice calculation and re-inserting this. It would be interesting to compute the R_{20} smeared correlators on a large volume for light quarks since we expect finite volume effects on the current volume.

Appendix A

Experimental Heavy Meson Spectra

A.1 Experimental Quarkonium Spectrum

The observed $c\bar{c}$ and $b\bar{b}$ spectra are as follows

	Radial State (GeV) $\longrightarrow$		
State	1	2	3
η_c	2.980	3.594	
J/ψ	3.097	3.686	3.770
h_c	3.526	?	
χ_{c0}	3.415	?	
χ_{c1}	3.510	?	
χ_{c2}	3.556	?	

	Radial State (GeV) $\longrightarrow$		
State	1	2	3
η_b	?		
Υ	9.460	10.233	10.355
h_b	?		
χ_{b0}	9.860	10.232	
χ_{b1}	9.892	10.255	
χ_{b2}	9.913	10.269	

A.2 Experimental Heavy-Light Spectrum

Here I give the observed spectra of heavy-light mesons and include the K system because the complete set of unexcited (radially) P-states has been observed, displaying the general angular momentum structure for non-degenerate mesons.

	State (GeV) $\longrightarrow$	
State	1	2
K	0.495	
K^*	0.892	1.410
K_0^*	1.430	
$K_1(\frac{1}{2})$	1.400	
$K_1(\frac{3}{2})$	1.270	
K_2^*	1.430	

State	GeV
D	1.865
D^*	2.007
$D_1(\frac{3}{2})$	2.420
D_2^*	2.460
D_s	1.968
D_s^*	2.112
$D_{s1}(\frac{3}{2})$	2.536
D_{s2}^*	2.573

State	GeV
B	5.279
B^*	5.325
$B^{**}(\frac{3}{2})$	5.732
B_s	5.369
B_s^*	5.416
$B_s^{**}(\frac{3}{2})$	5.850

Appendix B

Helmholtz Green Function

In the 3d Born approximation we are interested in the Green function $G(y)$ of the Helmholtz operator,

$$\{\nabla^2 + k^2\}G(y) = \delta(y) \tag{B.14}$$

associated with the Schroedinger eqaution. This equation is easily solved in Fourier space, with solution

$$G(p) = \frac{1}{k^2 - p^2}. \tag{B.15}$$

In order to obtain the coordinate space representation of the Green function we need to consider the inverse Fourier transform of B.15

B.1 Fourier Transform of $\frac{1}{k^2-p^2}$

We solve the Fourier integral using Cauchy's residue theorem. Consider

$$G(r) = \frac{1}{(2\pi)^3}\int d^3p \frac{e^{ip\cdot r}}{k^2 - p^2} \tag{B.16}$$

writing $d^3p = p^2 d(\cos\theta)d\phi$ and performing the ϕ integral we have

$$\begin{aligned} G(r) &= \frac{1}{(2\pi)^2}\int_0^\infty dp \int_{-1}^{1} d(\cos\theta)\frac{p^2 e^{ipr\cos\theta}}{k^2 - p^2} && \text{(B.17)} \\ &= \frac{1}{(2\pi)^2}\int_0^\infty dp \frac{p^2}{k^2 - p^2}\frac{e^{ipr} - e^{-ipr}}{ipr} && \text{(B.18)} \end{aligned}$$

$$= \frac{1}{(2\pi)^2} \int_{-\infty}^{\infty} dp \frac{pe^{ipr}}{k^2 - p^2} \frac{1}{ir} \tag{B.19}$$

Using the usual trick, the denominator $k^2 - p^2$ has poles at $p = |k| + i\epsilon$ and $p = -|k| - i\epsilon$ so that only the pole is in the above the real line. Closing around the upper half plane, the residue is $-\frac{1}{2\cdot(2\pi)^2}\frac{e^{ikr}}{ir}$ and so the integral is

$$G(r) = -\frac{e^{ikr}}{4\pi r} \tag{B.20}$$

Appendix C

Quarkonium Wavefunction Solutions

C.1 Radial Wavefunction Solutions

Given the non-relativistic potential ansatz, and the Breit-Fermi Hamiltonian,

$$\mathcal{H} = 2m + \frac{p^2}{2\mu} + V_{NR}(r) + \mathcal{H}_{L.S} + \mathcal{H}_{S.S} + \mathcal{H}_T, \tag{C.21}$$

$$V_{NR}(r) = V_V(r) + V_S(R), \tag{C.22}$$

$$\mathcal{H}_{L.S} = \frac{1}{2m^2 r} L.S \left[3\frac{\partial V_V(r)}{\partial r} - \frac{\partial V_S(r)}{\partial r} \right], \tag{C.23}$$

$$\mathcal{H}_{S.S} = \frac{2}{3m^2} S_1.S_2 \nabla^2 V_V(r), \tag{C.24}$$

$$\mathcal{H}_T = \frac{1}{12m^2} \mathcal{S}_{12} \left[\frac{1}{r}\frac{\partial}{\partial r} V_V(r) - \frac{\partial^2}{\partial r^2} V_V(r) \right], \tag{C.25}$$

we treat the wavefunction as factorised into spin and spatial parts, and solve the spin independent Schroedinger equation:

$$-\nabla^2 \psi(r) = M \left[E - V_V(r) - V_S(r) \right] \psi(r) \tag{C.26}$$

obtaining an orthogonal set of radial wavefunctions for each $L = 0, 1, 2...$

$$\psi_{nlm}(r, \theta, \phi) = R_{nl}(r) P_{lm}(\theta\phi) \tag{C.27}$$

where P_{lm} are the spherical harmonics. The orthogonality relation between the radial wavefunctions R_{nl} is then

$$\int dV \psi^*_{mko}\psi_{nlp} = \delta_{kl}\delta_{op}\int_{r=0}^{\infty} R^*_{ml}(r)R_{nl}(r)r^2 dr \tag{C.28}$$

$$\Rightarrow \int_{r=0}^{\infty} R^*_{ml}(r)R_{nl}(r)r^2 dr = \delta_{mn} \tag{C.29}$$

Writing

$$y_{nl}(r) = rR_{nl}(r) \tag{C.30}$$

the Schroedinger equation becomes

$$y''_{nl}(r) = \left[M\{E - V_V(R) - V_S(R)\} + \frac{L(L+1)}{r^2}\right] y_{nl}(r). \tag{C.31}$$

Note that the normalisation of y is

$$\int_0^{\infty} |y(r)|^2 dr = 1 \tag{C.32}$$

and that for S-states,

$$\psi_{00}(r) = \frac{1}{\sqrt{4\pi}}\frac{y_{00}(r)}{r} \tag{C.33}$$

The task of solving the model for a given potential reduces to a one dimensionl second order differential equation, which may be solved either analytically or numerically depending on the potential.

Apart from the obvious application - calculation of the spin-dependent perturbations to obtain the energy eigenvalues - the wavefunctions obtained in potential models may be used in a number of interesting ways. Firstly I consider their use as an improved smearing basis in lattice calculations. Secondly I derive a useful result for the wavefunction at the origin, which may be applied to both the hyperfine splitting and the electroweak decay constant of quarkonium. Finally I consider the use of the solutions with the Virial theorem as a consistency check that the system is indeed non-relativistic.

C.2 Smearing In a Non-Relativistic Model

We now consider smearing in the context of a non-relativistic model with spatial wavefunction solutions ψ_n

Suppose we construct a non-local meson operator

$$\mathcal{O}_n(x) = \int d^3y \bar{\psi}(y) S(y,x) \psi(x) \tag{C.34}$$

where the smearing function $S(y,x) = S(y-x)$ is thought of as a spatial wavefunction defined on lattice sites

$$S(y,0) \equiv S(y) \sum_{i,j,k} \delta^3(y - i\hat{x} - j\hat{y} - k\hat{z}) \tag{C.35}$$

Note we have dropped the colour indices since in our wavefunction approximation the gauge degrees of freedom are represented by a colour singlet potential.

The operator $\mathcal{O}$ will have an overlap with each physical state $|\psi_m\rangle$ of the relevant J^{PC}

$$C_{nm} = \int_{\mathbb{R}^3} \psi_m^*(x) S(x) dV = \sum_{i,j,k} \psi_m^*(i\hat{x} + j\hat{y} + k\hat{z}) S(i\hat{x} + j\hat{y} + k\hat{z}) \tag{C.36}$$

Now if $S_n(x)$ is chosen to well approximate the state $\psi_n(x)$ and the lattice is sufficiently fine that the sum C.36 is close to the integral

$$C_{nm} = \int \psi_m^* S_n(x) dV \simeq \psi_m^*(x) \psi_n(x) dV = \delta_{nm} \tag{C.37}$$

Thus with a well chosen set smearing functions S_n we can write

$$C_{nm} = \delta_{nm} + \eta_{nm} \tag{C.38}$$

where η_{nm} is a small contamination to the signal, giving a set of correlation functions corresponding to each of the physical radial exctitations.

If we modify the smearing functions, such that for each n the contamination

$$\eta_{nm} \simeq 0 \quad \forall m < n \tag{C.39}$$

Then the lowest state overlapping with the nth radially excited operator is in fact the nth state, and the effective mass will not decay to the ground state of the J^{PC}, giving access to plateaux for excited states.

The spin-dependent Hamiltonian can be solved as a perturbation about the solutions obtained for the spin independent wave equation, allowing the structure of the quarkonium spectrum to be studied.

C.3 Wavefunction at the Origin

The wavefunction at the origin is of interest because it is a factor in both the electroweak decays and the hyperfine structure of quarkonium. A useful result for the wavefunction at the origin can be derived as follows. Consider the integral

$$-\int d^3r \frac{y''y'}{4\pi r^2} = -\tfrac{1}{2}\int_0^\infty dr (y'^2)' = -\tfrac{1}{2}\left[y'^2\right]_0^\infty = -2\pi\left[(\psi + r\psi')^2\right]_0^\infty = 2\pi|\psi(0)|^2 \tag{C.40}$$

Inserting the Schroedinger equation for y'' gives

$$-M\int d^3r \left[E - V(r)\right]\frac{yy'}{4\pi r^2} = \tfrac{1}{2}M\int_0^\infty dr\left[E - V(r)\right](y^2)' = \tfrac{1}{2}M\int_0^\infty drV'(r)y^2 = \tfrac{1}{2}M\langle V'\rangle \tag{C.41}$$

We have neglected the boundary term at $r = 0$, since finiteness of $\psi(0)$ implies that for small r , $y(r) \overset{r\to 0}{\propto} r^n$ for some $n \geq 1$. The tree level potential implies $V(r) \overset{r\to 0}{\propto} \frac{1}{r}$ and hence $\lim_{r\to 0}(E - V(r))y^2 = 0$.

Thus we have

$$|\psi(0)|^2 = \frac{M}{4\pi}\langle V'(r)\rangle \tag{C.42}$$

For the Cornell potential this yields

$$|\psi(0)|^2 = \frac{M}{4\pi}\langle\frac{4}{3}\frac{\alpha_s}{r^2} + K\rangle \tag{C.43}$$

C.4 Virial Theorem in Phenomenological Potential

The quarkonium wavefunctions obtained from the non-relativistic model can be used in the Virial theorem as a consistency check that the systems in question are indeed non-relativistic:

For a spherical potential,

$$Mv^2\langle T\rangle = \tfrac{1}{2}\langle rV'(r)\rangle \tag{C.44}$$

giving estimates that [59] for charmonium $\frac{v^2}{c^2} \simeq 0.4$ and bottomonium $\frac{v^2}{c^2} = 0.1$ which suggests that qualitative behaviour suggested for charm is useful and that quantitative values for beauty may be of use.

Appendix D

$\beta = 6.0$ Fitted Lattice Masses

This appendix contains tables of best fits to the lattice data in the $\beta = 6.0$ heavy-light two point function calculation.

Table D.11: Light-light Pseudoscalars

State	χ^2/dof	Q	M_{GS}	M_{EX}
Pseudo (3856,3856)	1.1	0.38	0.228(2)	1.1(3)
Pseudo (3856,3810)	1.0	0.45	0.263(1)	0.9(1)
Pseudo (3856,3700)	1.1	0.35	0.332(1)	0.94(7)
Pseudo (3810,3810)	1.0	0.41	0.293(1)	0.91(7)
Pseudo (3810,3700)	1.0	0.43	0.357(1)	0.94(5)
Pseudo (3700,3700)	1.1	0.31	0.4135(10)	0.99(3)

Table D.12: Light-light Vectors

State	χ^2/dof	Q	M_{GS}	M_{EX}
Vector (3856,3856)	1.3	0.12	0.426(9)	0.95
Vector (3856,3810)	1.4	0.094	0.446(7)	1.1(1)
Vector (3856,3700)	1.4	0.10	0.486(5)	1.11(9)
Vector (3810,3810)	1.5	0.037	0.463(5)	1.1(1)
Vector (3810,3700)	1.5	0.050	0.502(3)	1.11(7)
Vector (3700,3700)	1.6	0.035	0.539(2)	1.12(5)

Table D.13: Heavy-light Pseudoscalars

State	χ^2/dof	Q	M_{GS}	M_{EX}
Pseudo (3000,3700)	0.93	0.55	0.6933(9)	1.24(5)
Pseudo (3000,3810)	1.1	0.37	0.653(1)	1.19(7)
Pseudo (3000,3856)	1.4	0.082	0.637(2)	1.17(8)
Pseudo (2600,3700)	0.99	0.47	0.8231(9)	1.37(5)
Pseudo (2600,3810)	1.1	0.30	0.786(1)	1.33(6)
Pseudo (2600,3856)	1.5	0.073	0.771(2)	1.32(8)
Pseudo (2200,3700)	1.0	0.42	0.9413(10)	1.48(5)
Pseudo (2200,3810)	1.2	0.24	0.906(2)	1.46(6)
Pseudo (2200,3856)	1.4	0.090	0.892(2)	1.45(7)
Pseudo (1800,3700)	1.1	0.37	1.051(1)	1.58(5)
Pseudo (1800,3810)	1.2	0.20	1.017(2)	1.57(6)
Pseudo (1800,3856)	1.4	0.11	1.003(2)	1.56(7)
Pseudo (1400,3700)	1.1	0.31	1.155(1)	1.68(5)
Pseudo (1400,3810)	1.3	0.16	1.122(2)	1.67(6)
Pseudo (1400,3856)	1.3	0.13	1.109(3)	1.67(7)

Table D.14: Heavy-light Vectors

State	χ^2/dof	Q	M_{GS}	M_{EX}
Vector (3000,3700)	1.1	0.30	0.766(1)	1.43(6)
Vector (3000,3810)	0.88	0.62	0.732(2)	1.5(1)
Vector (3000,3856)	0.58	0.94	0.720(3)	1.5(1)
Vector (2600,3700)	1.0	0.41	0.882(1)	1.50(5)
Vector (2600,3810)	0.71	0.84	0.849(2)	1.53(9)
Vector (2600,3856)	0.50	0.97	0.837(3)	1.6(1)
Vector (2200,3700)	1.0	0.43	0.990(1)	1.58(5)
Vector (2200,3810)	0.69	0.86	0.959(2)	1.60(8)
Vector (2200,3856)	0.51	0.97	0.946(3)	1.6(1)
Vector (1800,3700)	1.0	0.43	1.093(1)	1.67(4)
Vector (1800,3810)	0.73	0.82	1.062(2)	1.68(7)
Vector (1800,3856)	0.56	0.95	1.050(3)	1.71(10)
Vector (1400,3700)	1.0	0.42	1.192(1)	1.75(4)
Vector (1400,3810)	0.77	0.76	1.161(2)	1.76(7)
Vector (1400,3856)	0.60	0.93	1.149(3)	1.78(9)

Table D.15: Heavy-light 0^+

State	χ^2/dof	Q	M_{GS}	M_{EX}
A0 (3000,3700)	1.5	0.13	0.974(8)	1.66(9)
A0 (3000,3810)	1.6	0.093	0.97(1)	1.7(1)
A0 (3000,3856)	1.2	0.26	0.99(1)	1.8(2)
A0 (2600,3700)	1.4	0.15	1.088(8)	1.73(8)
A0 (2600,3810)	1.5	0.12	1.079(10)	1.8(1)
A0 (2600,3856)	1.1	0.36	1.10(1)	1.9(1)
A0 (2200,3700)	1.4	0.17	1.195(7)	1.80(7)
A0 (2200,3810)	1.4	0.16	1.186(9)	1.83(9)
A0 (2200,3856)	0.99	0.46	1.21(1)	1.9(1)
A0 (1800,3700)	1.3	0.19	1.297(7)	1.88(6)
A0 (1800,3810)	1.3	0.20	1.288(9)	1.90(8)
A0 (1800,3856)	0.90	0.55	1.31(1)	2.0(1)
A0 (1400,3700)	1.3	0.21	1.396(7)	1.96(6)
A0 (1400,3810)	1.2	0.25	1.386(9)	1.97(8)
A0 (1400,3856)	0.84	0.61	1.40(1)	2.1(1)

Table D.16: Heavy-light 1^{++}

State	χ^2/dof	Q	M_{GS}	M_{EX}
A1 (3000,3700)	1.2	0.24	1.014(8)	1.62(5)
A1 (3000,3810)	1.8	0.050	1.000(10)	1.60(6)
A1 (3000,3856)	1.6	0.081	1.02(1)	1.62(9)
A1 (2600,3700)	1.3	0.20	1.125(7)	1.72(5)
A1 (2600,3810)	1.9	0.034	1.111(9)	1.70(6)
A1 (2600,3856)	1.7	0.067	1.13(1)	1.72(7)
A1 (2200,3700)	1.4	0.17	1.229(7)	1.81(4)
A1 (2200,3810)	1.9	0.028	1.216(9)	1.79(5)
A1 (2200,3856)	1.7	0.055	1.23(1)	1.82(7)
A1 (1800,3700)	1.4	0.16	1.328(7)	1.89(4)
A1 (1800,3810)	1.9	0.031	1.316(9)	1.88(5)
A1 (1800,3856)	1.7	0.060	1.33(1)	1.91(7)
A1 (1400,3700)	1.4	0.16	1.424(7)	1.98(4)
A1 (1400,3810)	1.8	0.043	1.412(9)	1.97(5)
A1 (1400,3856)	1.6	0.083	1.43(1)	1.99(7)

Table D.17: Heavy-light 1^{+-}

State	χ^2/dof	Q	M_{GS}	M_{EX}
B1 (3000,3700)	1.2	0.26	1.013(9)	1.59(6)
B1 (3000,3810)	1.6	0.089	1.00(1)	1.63(9)
B1 (3000,3856)	1.8	0.045	1.02(1)	1.7(1)
B1 (2600,3700)	1.4	0.15	1.123(9)	1.68(6)
B1 (2600,3810)	1.8	0.047	1.11(1)	1.71(8)
B1 (2600,3856)	1.8	0.037	1.13(1)	1.8(1)
B1 (2200,3700)	1.6	0.089	1.226(8)	1.77(6)
B1 (2200,3810)	1.9	0.030	1.21(1)	1.79(8)
B1 (2200,3856)	1.8	0.040	1.23(1)	1.8(1)
B1 (1800,3700)	1.7	0.060	1.325(8)	1.85(5)
B1 (1800,3810)	1.9	0.025	1.313(10)	1.87(7)
B1 (1800,3856)	1.7	0.054	1.33(1)	1.90(9)
B1 (1400,3700)	1.8	0.050	1.420(8)	1.94(5)
B1 (1400,3810)	1.9	0.028	1.41(1)	1.94(7)
B1 (1400,3856)	1.6	0.083	1.42(1)	1.97(9)

Table D.18: Heavy-light $M_2(PS)$

State	χ^2/dof	M_2
Pseudo (3000,3700)	1.05	0.73(2)
Pseudo (3000,3810)	0.34	0.68(3)
Pseudo (3000,3856)	0.25	0.65(3)
Pseudo (2600,3700)	1.0	0.90(2)
Pseudo (2600,3810)	0.21	0.85(2)
Pseudo (2600,3856)	0.22	0.82(3)
Pseudo (2200,3700)	0.85	1.07(2)
Pseudo (2200,3810)	0.15	1.02(3)
Pseudo (2200,3856)	0.24	0.98(3)
Pseudo (1800,3700)	0.70	1.24(2)
Pseudo (1800,3810)	0.14	1.19(3)
Pseudo (1800,3856)	0.27	1.15(4)
Pseudo (1400,3700)	0.65	1.41(2)
Pseudo (1400,3810)	0.15	1.37(3)
Pseudo (1400,3856)	0.34	1.33(4)

Table D.19: Heavy-heavy Pseudoscalar

State	χ^2/dof	Q	M_{GS}	M_{EX}
Pseudo (3000,3000)	0.83	0.68	0.9283(7)	1.41(3)
Pseudo (2600,2600)	0.88	0.61	1.1619(6)	1.60(2)
Pseudo (2200,2200)	0.99	0.47	1.3755(6)	1.79(2)
Pseudo (1800,1800)	1.2	0.25	1.5751(6)	1.97(1)
Pseudo (1400,1400)	1.4	0.093	1.7644(6)	2.14(1)

Table D.20: Heavy-heavy Vector

State	χ^2/dof	Q	M_{GS}	M_{EX}
Vector (3000,3000)	1.0	0.44	0.9780(9)	1.49(2)
Vector (2600,2600)	0.95	0.52	1.1990(8)	1.66(2)
Vector (2200,2200)	1.0	0.44	1.4052(7)	1.83(1)
Vector (1800,1800)	1.2	0.26	1.5998(7)	2.00(1)
Vector (1400,1400)	1.4	0.12	1.7854(7)	2.17(1)

Table D.21: Heavy-heavy 0^{++}

State	χ^2/dof	Q	M_{GS}	M_{EX}
A0 (3000,3000)	1.1	0.37	1.161(7)	1.76(10)
A0 (2600,2600)	0.92	0.56	1.376(7)	1.89(7)
A0 (2200,2200)	0.91	0.57	1.578(6)	2.04(5)
A0 (1800,1800)	1.0	0.45	1.770(6)	2.19(4)
A0 (1400,1400)	1.2	0.28	1.955(7)	2.34(4)

Table D.22: Heavy-heavy 1^{++}

State	χ^2/dof	Q	M_{GS}	M_{EX}
A1 (3000,3000)	0.62	0.90	1.193(7)	1.76(7)
A1 (2600,2600)	0.56	0.94	1.404(7)	1.91(6)
A1 (2200,2200)	0.65	0.87	1.602(6)	2.07(5)
A1 (1800,1800)	0.79	0.73	1.791(7)	2.22(4)
A1 (1400,1400)	0.91	0.58	1.972(7)	2.37(4)

Table D.23: Heavy-heavy 1^{+-}

State	χ^2/dof	Q	M_{GS}	M_{EX}
B1 (3000,3000)	0.56	0.94	1.193(8)	1.67(6)
B1 (2600,2600)	0.42	0.99	1.402(7)	1.86(5)
B1 (2200,2200)	0.51	0.96	1.602(7)	2.04(5)
B1 (1800,1800)	0.70	0.83	1.792(7)	2.21(4)
B1 (1400,1400)	0.86	0.64	1.975(7)	2.37(4)

Table D.24: Heavy-heavy $M_2(PS)$

State	χ^2/dof	M_2
Pseudo (3000,3000)	1.0	1.024(11)
Pseudo (2600,2600)	0.14	1.350(11)
Pseudo (2200,2200)	0.14	1.686(12)
Pseudo (1800,1800)	0.6	2.05(1)
Pseudo (1400,1400)	0.9	2.43(1)
Pseudo (2600,1400)	0.12	1.87(1)
Pseudo (2600,1800)	0.06	1.69(1)
Pseudo (2600,2200)	0.025	1.51(1)

References

[1] F. Mandl and G. Shaw. Quantum Field Theory. John Wiley and Sons, 1993.

[2] D. Bailin and A. Love. Introduction to Gauge Field Theory. Institute of Physics Publishing, Techno House, Redcliffe Way, Bristol, 1993.

[3] G. Sterman. An Introduction to Quantum Field Theory. Cambridge University Press, Trumpington Street, Cambridge, 1993.

[4] I. Montvay and G. Münster. Quantum Fields on a Lattice. Cambridge University Press, Cambridge, 1994.

[5] I. Stewart and D. Tall. Complex Analysis. Cambridge University Press, Cambridge, 1983.

[6] K. G. Wilson. *Phys. Rev. D*, **10**, 2445, (1974).

[7] N. Metropolis et al. *J. Chem. Phys.*, **21**, 1087, (1953).

[8] M. Luscher. *Nucl. Phys. B*, **254**, 52, (1985).

[9] B. Sheikholeslami and R. Wohlert. *Nucl. Phys. B*, **259**, 572, (1985).

[10] K. Symmanzik. *Nucl. Phys. B*, **226**, 187,205, (1983).

[11] G. Heatlie et al. *Nucl. Phys. B*, **352**, 266, (1991).

[12] H. B. Nielsen and M. Ninomiya. *Nucl. Phys. B*, **185**, 20, (1981).

[13] P. Lepage and P. Mackenzie. *Phys. Rev. D*, **48**, 2250, (1993).

[14] M. Luscher et al. *Nucl. Phys. B*, **478**, 365, (1996).

[15] M. Luscher et al. *HEP-LAT*, **9609035**, (1996).

[16] M. Luscher et al. *Nucl. Phys. B (Proc. Suppl.)*, **53**, 905, (1997).

[17] B Efron. The jacknife, the bootstrap and other resampling plans. *Society for Industrial and Applied Mathematics*, (1982).

[18] P. Van Baal and A. Kronfeld. *Nucl. Phys. B (Proc. Suppl.)*, **9**, 227, (1989).

[19] D. Weingarten. Lattice algorithms and predictions for the qcd spectrum. Lecture course at Computing Particle Properties School, March 1997. 36 Internationale Universitatwochen fur Kern und Teilchenphysik, Schladming, Austria.

[20] M. Wingate et al. *Phys. Rev. D*, **52**, 307, (1995).

[21] C. Michael et al. *Phys. Rev. D*, **54**, 6997, (1996).

[22] J. F. Cornwell. Group Theory in Physics, Vols. 1,2. Academic Press, London, 1984.

[23] C. Allton et al. *Phys. Rev. D*, **47**, 5128, (1993).

[24] S. Gusken et al. *Nucl. Phys. B (Proc. Suppl.)*, **17**, 361, (1990).

[25] P. Lacock et al. *Phys. Rev. D*, **51**, 6403, (1995).

[26] C. Davies et al. *Phys. Lett. B*, **382**, 131, (1996).

[27] A El-Khadra et. al. *Phys. Rev. D*, **55**, 3933, (1997).

[28] S. Aoki et al. *Nucl. Phys. B (Proc. Suppl.)*, **53**, 355, (1997).

[29] W. Lucha. Effective potential models for hadrons. Lecture course, August-September 1995. Development in Nuclear Theory and Particle Physics summer school, Dubna.

[30] L. Landau and E. Lifschitz. Quantum Mechanics (Non-relativistic theory). Pergamon, Headington Hill Hall, Oxford, 3rd Edition 1977.

[31] W. Lucha et al. *Phys. Rep.*, **200**, 127, (1991).

[32] W. Buchmuller. Fine and hyperfine structure of quarkonia. *Phys. Lett. B*, **112**, 479, (1982).

[33] A. El-Kahadra. *Nucl. Phys. B (Proc. Suppl.)*, **30**, 449, (1992).

[34] A. El-Kahadra et al. *Phys. Rev. Lett.*, **69**, 729, (1992).

[35] T. Mannel et al. *Nucl. Phys. B*, **368**, 274, (1991).

[36] E. Eichten C. Hill and C. Quigg. Orbitally excited heavy-light mesons revisited. *FERMILAB-CONF*, **118-T**, (May 94).

[37] E. Eichten C. Hill and C. Quigg. Spectra of heavy-light mesons. *FERMILAB-CONF*, **117-T**, (94).

[38] E. Eichten C. Hill and C. Quigg. *Phys. Rev. Lett.*, **71**, 4116, (1993).

[39] J. Rosner. P-wave mesons with one heavy quark. *Comm. Nucl. Part. Phys.*, **16**, 109, (1986).

[40] C. Quigg E. Eichten, C. Hill. Properties of orbitally excited heavy light mesons. *Phys. Rev. Lett.*, **71**, 4116, (1993).

[41] Aleph Collaboration. Production of excited beauty states in z decays. *Z. Phys. C*, **69**, 393, (1996).

[42] Aleph Collaboration. Produuction of orbitally excited charm mesons in semileptonic b decays. *Z. Phys C*, **73**, 601, (1997).

[43] S. Godfrey and N. Isgur. Mesons in a relativised quark model with chromodynamcs. *Phys. Rev. D*, **32**, 189, (1985).

[44] S. Godfrey and R. Kokoski. Properties of p-wave mesons with one heavy quark. *Phys. Rev. D*, **43**, 1679, (1991).

[45] A. Kaidalov and A Nogteva. *Sov. J. Nucl. Phys.*, **47**, 321, (1988).

[46] A. Edmonds. Angular Momentum in Quantum Mechanics. Princeton University Press, Princeton, New Jersey, 1974.

[47] S. M. Pickles. PhD thesis, University of Edinburgh, In preparation.

[48] W. H. Press, S. A. Teukolsky, W. T. Vetterling, and B. P. Flannery. Numerical Recipes in C. Cambridge University Press, Cambridge, 1992.

[49] S. Collins et al. *Nucl. Phys. B (Proc. Suppl.)*, **47**, 455, (1996).

[50] C. Davies. *hep-lat*, **9705039**, (1997).

[51] C. Davies et al. Precision upsilon spectroscopy from nonrelativistic lattice qcd. *Phys. Rev.*, **D50**, 6963, (1994).

[52] A. Alikhan et. al. The heavy - light spectrum from lattice nrqcd. *Phys. Rev. D*, **53**, 6433, (1996).

[53] S. Collins et. al. B spectroscopy from nrqcd with dynamical fermions. *Phys. Rev. D*, **54**, 5777, (1996).

[54] S. Collins. PhD thesis, University of Edinburgh, 1993.

[55] C. Allton. The hyperfine splitting in charmonium: Lattice computations using the wilson and clover fermion actions. *Phys. Lett.*, **B292**, 408, (1992).

[56] T. Bhattacharya et al. *Phys.Rev.D*, **53**, 6486–6508, (1996).

[57] Sinead Ryan. private communication, 1997. preliminary Fermilab results.

[58] Jim Simone. private communication, 1997. preliminary Fermilab results.

[59] C. Davies. The heavy hadron spectrum. Lecture course at Computing Particle Properties School, March 1997. 36 Internationale Universitatwochen fur Kern und Teilchenphysik, Schladming, Austria.